



January 2018

Plate Vibration Dispalcement Curve Measurement Using PVDF

Aniket Nandkumar Pinjan

Follow this and additional works at: <https://commons.und.edu/theses>

Recommended Citation

Pinjan, Aniket Nandkumar, "Plate Vibration Dispalcement Curve Measurement Using PVDF" (2018). *Theses and Dissertations*. 2311.
<https://commons.und.edu/theses/2311>

This Thesis is brought to you for free and open access by the Theses, Dissertations, and Senior Projects at UND Scholarly Commons. It has been accepted for inclusion in Theses and Dissertations by an authorized administrator of UND Scholarly Commons. For more information, please contact zeinebyousif@library.und.edu.

PLATE VIBRATION DISPLACEMENT CURVE MEASUREMENT USING PVDF

by

Aniket Nandkumar Pinjan
Bachelor of Engineering, Savitribai Phule Pune University, India, 2014

A Thesis

Submitted to the Graduate Faculty

of the

University of North Dakota

In partial fulfillment of the requirements

for the degree of

Master of Science

Grand Forks, North Dakota

AUGUST

2018

Copyright 2018 Aniket Pinjan


This thesis, submitted by Aniket N. Pinjan in partial fulfillment of the requirement for the Degree of Master of Science from the University of North Dakota, has been read by the Faculty Advisory Committee under whom the work has been done and hereby approved.



Dr. Marcellin Zahui



Dr. Surojit Gupta



Dr. Cai Xia Yang

This thesis is being submitted by the appointed advisory committee as having met all requirement School of the Graduate Studies at the University of North Dakota and is hereby approved.

Dr. Grant McGimpsey
Dean od School of Graduate Studies

Date

PERMISSION

Title Plate Vibration Displacement Curve Measurement Using PVDF
Department Mechanical Engineering
Degree Master of Science

In presenting this thesis in partial fulfillment of the requirements for a graduate degree from the University of North Dakota, I agree that the library of this University shall make it freely available for inspection. I further agree that permission for extensive copying for scholarly purposes may be granted by the professor who supervised my thesis work or, in his absence, by the chairperson of the department or the dean of the Graduate School. It is understood that any copying or publication or other use of this thesis or part thereof for financial gain shall not be allowed without my written permission. It is also understood that due recognition shall be given to me and to the University of North Dakota in any scholarly use which may be made of any material in my thesis.

Signature AN Pinjan

Date 07/09/2018

TABLE OF CONTENTS

LIST OF TABLES	xii
LIST OF VARIABLES.....	xiii
ACKNOWLEDGMENT.....	xix
ABSTRACT	xx
1. INTRODUCTION.....	1
1.1 Research Objective.....	1
1.2 Vibration Measurement.....	2
1.2.1 Importance of vibration measurement	2
1.2.2 Types of vibration and measurements	5
1.2.3 Types of sensors.....	7
1.2.4 Vibration Exciters	13
1.2.5 Signal Analysis.....	15
1.2.6 Modal Analysis	17
1.3 Origin of piezoelectricity and applications	21
1.3.1 Sensors	22
1.3.2 Actuators.....	23

1.3.3	Field of application.....	23
1.3.4	PVDF Properties	24
1.4	Thesis Layout	25
2	PIEZOELECTRIC SHELL VIBRATION THEORY	27
2.1	Fundamentals	27
2.2	Distributed Sensing of Elastic Shells	42
2.2.1	Generic Shape	42
2.2.2	Spatial Thickness Shaping	44
2.2.3	Spatial Surface Shaping.....	46
2.3	Cylindrical Shell.....	47
2.4	Plate Substrate	50
2.5	Beam Substrate.....	53
3	SENSOR DEVELOPMENT	37
3.1	Sensor Design.....	37
3.1.1	Beam Displacement Sensor Design	37
3.1.2	Plate Displacement Sensor Equation	60
3.2	Numerical Simulation	63
3.2.1	Beam Sensor	63
3.2.2	Plate Sensor	69

3.2.3	Multiphysics Simulation.....	73
4	EXPERIMENTAL DISPLACEMENT MEASUREMENT	78
4.1	Beam Experimental Displacement Measurement	78
4.1.1	Sensor shaping and fabrication	81
4.1.2	Experimental Measurement Procedure for beam.....	83
4.1.3	Experimental Results for the beam.	86
4.2	Plate Experimental Displacement Measurement.	89
4.2.1	Experimental Results for the plate.	92
5	CONCLUSION AND RECOMMENDATIONS.....	95
5.1	Conclusion.....	95
5.2	Recommendation for Future Work	97
6	APPENDICES.....	99
7	REFERENCES.....	107

LIST OF FIGURES

Figure 1.1: Basic vibration measurement scheme.....	4
Figure 1.2: Strain gauge.....	8
Figure 1.3 PCB Accelerometer.....	9
Figure 1.4: Linear variable differential transformer (LVDT).....	11
Figure 1.5: Noncontact Displacement sensors.....	12
Figure 1.6: Sper Scientific Direct Vibrometer model 840060.....	12
Figure 1.7: Reed K4030 Digital Stroboscope.....	13
Figure 1.8: Labworks ET-126 Electrodynamic shaker.....	14
Figure 1.9: Time domain and frequency domain graph.....	16
Figure 1.10: E4440A PSA Spectrum Analyzer, 3 Hz to 26.5 GHz.....	17
Figure 2.1: Representation of piezoelectric sensor bonded to a shell structure.....	28
Figure 2.2: Spatial Thickness Shaping.....	45
Figure 2.3: Spatial Surface Shaping.....	47
Figure 2.4: Cylindrical Shell with a Shaped Sensor Adhered.....	48
Figure 2.5: A Rectangular Plate Bonded with a Piezoelectric Sensor.....	52
Figure 3.1: Beam with PVDF film and deflection curve.....	59
Figure 3.2: Beam (S-S) first and second mode response (Continuous= Actual; Dot=Sensor).....	65

Figure 3.3: Beam (S-S) third and fourth mode response (Continuous= Actual; Dot=Sensor)	65
Figure 3.4: Beam (C-C) first and second mode response (Continuous= Actual; Dot=Sensor)	66
Figure 3.5: Beam (C-C) third and fourth mode response (Continuous= Actual; Dot=Sensor)	66
Figure 3.6: Beam (C-F) first and second mode response (Continuous= Actual; Dot=Sensor)	66
Figure 3.7: Beam (C-F) first and second mode response (Continuous= Actual; Dot=Sensor)	67
Figure 3.8: Layout of the PVDF sensor across plate for measuring plate deflection curve at resonance.....	70
Figure 3.9: Plate (S-S) first and second mode response (Continuous= Actual; Dot=Sensor)	72
Figure 3.10: Plate (S-S) third and fourth mode response (Continuous= Actual; Dot=Sensor)	72
Figure 3.11: Plate (C-C) first and second mode response(Continuous= Actual; Dot=Sensor)	72
Figure 3.12: Plate (C-C) third and fourth mode response (Continuous= Actual;Dot=Sensor)	73
Figure 3.13: Geometry of beam in ANSYS.....	75
Figure 3.14: S-S Beam first mode of vibration at frequency 56.672 Hz	77
Figure 3.15: S-S Beam second mode of vibration at frequency 230.77 Hz.....	77

Figure 3.16: S-S Beam third mode of vibration at frequency 519.53 Hz	77
Figure 3.17: C-C Beam first mode of vibration at frequency 129.44 Hz	78
Figure 3.18: C-C Beam second mode of vibration at frequency 358.88 Hz.....	78
Figure 3.19: C-C Beam third of vibration at frequency 706.64 Hz	78
Figure 3.20: C-F Beam first mode of vibration at frequency 20.771 Hz.....	79
Figure 3.21: C-F Beam second mode of vibration at frequency 130.04 Hz	79
Figure 3.22: C-F Beam third mode of vibration at frequency 364.41 Hz.....	79
Figure 4.1: Setup for Clamped-Clamped boundary condition of the beam.....	78
Figure 4.2: Setup for Simply Supported boundary condition of the beam.	79
Figure 4.3: Setup for Clamped-Free boundary condition of the beam.	80
Figure 4.4: Sensor template.	82
Figure 4.5: Sensor fabrication details.	82
Figure 4.6: Beam Experimental Setup using an accelerometer	84
Figure 4.7: Beam divided into 14 sections for accelerometer measurements.....	86
Figure 4.8: Beam (S-S) first and second mode response (Continuous= Actual; Dot=Sensor)	87
Figure 4.9: Beam (S-S) third mode r esponse(Continuous= Actual; Dot=Sensor).....	87
Figure 4.10: Beam (C-C) first and second mode response (Continuous= Actual; Dot=Sensor)	88
Figure 4.11: Beam (C-C) third mode response (Continuous= Actual; Dot=Sensor)	88
Figure 4.12: Beam (C-F) first and second mode response (Continuous= Actual; Dot=Sensor)	89

Figure 4.13: Beam (C-F) third mode response (Continuous= Actual; Dot=Sensor)	89
Figure 4.14: Plate with the grid mapping.....	90
Figure 4.15: Plate Experimental Setup using an accelerometer.	91
Figure 4.16: Plate (S-S) first and second mode response (Continuous= Actual; Dot=Sensor).....	93
Figure 4.17: Plate (S-S) third mode response (Continuous= Actual; Dot=Sensor)	93
Figure 4.18: Plate (C-C) first and second mode response (Continuous= Actual; Dot=Sensor).....	93
Figure 4.19: Plate (C-F) third mode response (Continuous= Actual; Dot=Sensor).....	94

LIST OF TABLES

Table 3.1: Simulation data for beam.....	65
Table 3.2: Boundary Condition and characteristics of the vibrating beam.....	68
Table 3.3: Natural Frequencies of Beam with boundary conditions.....	69
Table 3.4: Simulation data for plate.....	70
Table 3.5: Theoretical and finite element beam natural frequencies.....	81
Table 3.6: Percentage error for analytical and simulation calculation.....	81
Table 4.1: Properties of the test specimen.....	80

LIST OF VARIABLES

$\alpha_1, \alpha_2, \alpha_3$		curvilinear coordinate system
β_1, β_2		angles related to displacement
β_{33}		impermeability coefficient of the piezoelectric sensor
δ		variation
ε_{ij}		strain of the i^{th} surface and the j^{th} direction
ε_{ij}°		membrane strain of the i^{th} surface and the j^{th} direction
$[\epsilon]$		dielectric constant matrix
θ		theta direction in cylindrical coordinates
κ_{ij}		bending strain of the i^{th} surface and the j^{th} direction
ξ_j		fraction of critical damping for mode j
ρ		mass density
σ_{ij}		mechanical stress of the i^{th} surface and the j^{th} direction
σ		surface charge density
ν		Poisson's ratio
ϕ		electric potential
ϕ_3^S		total signal output in the three direction
$\{\phi\}_i$		eigenvector representing the mode shape of the i^{th} natural frequency
ω		natural frequency

ω_i	-----	i^{th} natural circular frequency
A_1 and A_2	-----	Lamé parameters
B	-----	<i>the</i> thickness of cylindrical shell
$[c]$	-----	elastic constant matrix
$[C]$	-----	structural damping matrix
D	-----	electric displacement
$\{D_j\}$	-----	electric displacement vector
E	-----	modulus of elasticity
E_j	-----	the electric field strength in the α_j direction
E_i^e	-----	electric field induced by an electric displacement
$[e]$	-----	piezoelectric constant matrix
e_{31}	-----	PVDF sensor strain/charge coefficients in the one direction
e_{32}	-----	PVDF sensor strain/charge coefficients in the two directions
F	-----	force
$\{F\}$	-----	force vector
$F(x, y)$	-----	shape function of the sensor
F_x	-----	first derivative of the shape function of the sensor with respect to x
F_{xx}	-----	second derivative of the shape function of the sensor with respect to x
F_y	-----	first derivative of the shape function of the sensor with respect to y
F_{yy}	-----	second derivative of the shape function of the sensor with respect to y
(f)	-----	natural frequency
H	-----	enthalpy

h^S ----- the thickness of the sensor
 h_{ij} ----- strain charge coefficient of the piezoelectric sensor
 i, j ----- stress tensors: surface and direction, respectively
 \hat{K} ----- kinetic energy
 $[K]$ ----- structural stiffness matrix
 L_x ----- dimension of the plate in the x -direction
 L_y ----- dimension of the plate in the y -direction
 $[M]$ ----- mass matrix
 P, P' ----- initial and end points, respectively
 Q ----- surface charge per unit area
 q ----- charge output of PVDF film
 R ----- *the* radius of cylindrical shell
 R_1 and R_2 ----- radii of curvatures in the 1 and two directions
 r_1, r_2 - distance measured from the neutral surface to the top and bottom of the sensor layer
 S ----- surface over the volume
 S_{ij} ----- mechanical strain of the i^{th} surface and the j^{th} direction
 S^e ----- *the* effective surface electrode area
 $\text{sgn}(\cdot)$ ----- signum function
 $\text{sgn}[U_3(\alpha_1, \alpha_2)]$ ----- polarity function
 t ----- surface traction
 t_0, t_1 ----- initial and end time, respectively
 $\{T_{ij}\}$ ----- stress vector

$U_1, U_2,$ and U_3	-----	generic deflections
$U_x, U_y,$ and U_z	-----	displacements in the x, y, and z directions
\hat{U}	-----	potential energy
$\{u\}$	-----	nodal displacement vector
V	-----	piezoelectric volume
$W_s(\alpha_1, \alpha_2)$	-----	weighting shape function
$W_t(\alpha_1, \alpha_2)$	-----	spatial function
w_x	-----	--first partial derivative of the plate surface displacement field $w(x,y)$ with respect to x
w_y	-----	--first partial derivative of the plate surface displacement field $w(x,y)$ with respect to y
w_{xx}	-----	2^{nd} partial derivative of the plate surface displacement field $w(x,y)$ with respect to x
w_{yy}	-----	2^{nd} partial derivative of the plate surface displacement field $w(x,y)$ with respect to y
Z	-----	length of the cylindrical shell
h_p	-----	plate thickness
h_s	-----	sensor thickness
q_x	-----	charge along due to bending the x -axis
q_y	-----	charge along due to bending the y -axis
q^T	-----	Top sensor's total charge due to bending in x and y axis
q_x^T	-----	Top sensor's total charge due to bending along the x -axis
q_y^T	-----	Top sensor's total charge due to bending along the y -axis
k_{31}	-----	random variable assigned to plate properties
k_{32}	-----	random variable assigned to plate properties
z_x	-----	Slope of the sensor patch at a particular location along x -axis
z_y	-----	Slope of the sensor patch at a particular location in along y -axis

l_x^S	-----	length of the sensor along x -axis
l_y^S	-----	length of the sensor in the along y -axis
q^B	-----	Bottom sensor's total charge due to bending
q_x^B	-----	Bottom sensor's total charge due to bending along the x -axis
q_y^B	-----	Bottom sensor's total charge due to bending along the y –axis
h	-----	height of the plate and sensor together
x_1, x_2	-----	initial and end point of the sensor patch along x -axis
y_1, y_2	-----	initial and end point of the sensor patch along y -axis
i	-----	sensor patch considered for numerical calculation
Φ_i	-----	charge produced at the location i due to bending
b	-----	width of the beam
h_i^f	-----	PVDF film thickness of patch i
S_i^f	-----	PVDF surface area at location i
h_{31i}	-----	PVDF strain/charge coefficient at location i along x -axis
x_{i-1}, x_i	-----	initial and end points locations to calculate the slope of patch
$r_{x_i}^f$	-----	distance from the neutral axis to top surface of the film at location i
$\frac{\partial^2 z_i}{\partial x^2}$	-----	double derivative of the slope at location i along x -axis
$\frac{\partial z_i}{\partial x}$	-----	derivative of the slope at location i along x -axis
a_i	-----	slope of the sensor patch at the location i
x	-----	center point on the patch i
Δx	-----	distance between the center and extreme points of patch
$z(x)$	-----	deflection along the x -axis
m	-----	maximum number of modes

k	-----	number of modes
W_k	-----	modal participation factor for k^{th} mode
Ψ_k	-----	mode shape for k^{th} mode
n	-----	number of sections on the sensor
l_p	-----	length of the plate
$\{\Psi_k\}^T$	-----	transpose vector for mode shape
$\{f\}$	-----	force vector exciting the beam/plate
ω_k	-----	natural frequency for the k^{th} mode
ω	-----	excitation frequency
η_k	-----	structural damping factor for beam/plate
l	-----	length of the beam
$(\beta_n l)$	-----	boundary condition constants for the beam
E	-----	Young's modulus for aluminum
ρ	-----	density of aluminum
A	-----	area of the cross-section for the beam
ω_n	-----	natural frequency of the beam
f_n	-----	natural frequency in radians

ACKNOWLEDGMENT

This work would not have been possible without the support from my research advisory committee members Dr. Zahui, Dr. Gupta and Dr. Cia Xia Yang. With direction provided by Dr. Zahui, I learned a great deal about FEA and thankful to the rest of committee members for their confidence, tolerance, and support during last two years. I would also like to thank the Mechanical Engineering Department at the University of North Dakota for providing the space and means to complete this research. Finally, I would like to thank my family members and friends for their support during this project. Their understanding and support have been very motivating.

*To my mom Vijaya and dad Nandkumar,
& loving memory of my Grandfather Namdeo*

ABSTRACT

Beam and plate dynamics are often measured using accelerometers and in some cases laser-based systems. Natural frequencies, mode shapes, and deflections are then derived from these measurements. The work presented here describes a method to directly measure the deflection curve of a vibrating beam and plate using piezoelectric films. The sensor consists of constant shape segment of PolyVinylidene Fluoride (PVDF) films bonded to the surface of the structure. We show in here that each segment of the sensor measures the deflection slope at its particular location. The overall lateral displacement curve of the structure (beam/plate) is calculated from these slopes using central difference formulas. In this work, the equations of the sensor are presented along with the results of the numerical verifications. Numerical simulations are executed through MATLAB, whereas Multiphysics simulation is accomplished through ANSYS, and the results of these simulations are compared to the experimental results. The results indicate that the proposed sensors can be used to efficiently and respectively measure the lateral vibration displacements curves of beams and plates with various boundary conditions.

CHAPTER I

INTRODUCTION

1.1 Research Objective

The focus of this research aims towards the design of PolyVinylidene Fluoride (PVDF) sensor to measure the deflection curve of the vibrating beam and a vibrating plate. The displacement measurements of these vibrating structures are often conducted through accelerometers and sometimes laser-based system. Natural frequencies, modes shapes, and deflections are obtained through these measurements. The sensor used in this research is made of multiple constant shape PVDF film, bonded to the vibrating surface. The individual charge of each PVDF section is proportional to the slope of the beam or plate's section. Using the slopes of the structures at different segments and implementing central difference method, the beam or plate surface deflection curve can be calculated. The equation of the sensor is derived, followed with numerical calculations through MATLAB and Multiphysics simulation using ANSYS. The experimental results along with numerical calculations confirm that the designed sensors can effectively measure the deflection curve of prismatic beams and plates with various boundary conditions. The accuracy of the sensor highly depends upon the number of sensor patches and the range of frequency over which the measurements are intended.

1.2 Vibration Measurement

In this section, we see the various aspects of vibration measurement and applications. The basic scheme for vibration measurement is outlined here. Devices like transducers are described which transform physical variables into equivalent electrical signals. Frequency response function and the instruments used for vibration measurement along with electrodynamic shakers or exciters used to excite a machine or system to study its dynamic characteristics are outlined too. Signal analysis process, to represent the signal received from the vibrating system in a convenient form, is discussed. The modal analysis determines the natural frequencies, mode shapes, and damping ratio through vibration testing. Thus, in the process of vibrating testing of the structure, the necessary equipment, digital signal processing, analysis of random signals received from the structure, determining mode shapes are all described in this section.

1.2.1 Importance of vibration measurement

Vibration is a mechanical phenomenon which results in oscillations of the structure from its equilibrium point. The word vibration is derived from the Latin word 'vibrationem,' i.e., shaking, brandishing. The process of hearing involves eardrum vibration, and we see because light waves undergo vibration too. Breathing is associated with lung vibration, and so is the fact that humans speaking is associated with the tongue vibration. Vibration can be desirable in cases such as tuning fork, guitar strings producing melody tune, loudspeaker producing loud sounds or a mobile phone vibration. In many cases, vibration is undesirable, cause for energy wastage and creating undesirable effects in vehicle engines, electric motors, bridge, etc. Wheels of some locomotives rise from the ground at high speeds due to imbalance and vibration arises from the imbalances in the

rotating parts of the mechanical system, friction between the mating objects, effects of other working parts in a larger assembly or the environmental conditions affecting the operation of a structure. In a situation such as structures designed to support heavy machinery, like turbines and motors, steam and gas engines, and reciprocating pumps are subjected to vibrations. Engineers have found the task of vibration mitigation in turbine difficult due to disk and blade vibration, and hence it is crucial to address the failure in machinery like hydraulic turbines [1]. Vibration is also held responsible for rapid wear of machine parts such as bearings and gears [2]. Furthermore, vibration causes chatter in the cutting process resulting in reduced surface finish [3]. In the State of Illinois, the case of highway light poles; characterized with slender structures and low values of structural damping leading to large-amplitude vibration causing the structure to collapse [4] [5] and thus recommending vibration reduction through proposed dampers. The resonance phenomenon occurs when the natural frequency of a structure coincides with the external excitation frequency, leading to high amplitude vibrations, excessive deflection, and structural failure. The standard example of resonance effect is the bridge collapsing due to human-induced external events and natural causes [6]. Vibration measurement is necessary, as with industrialization and modernization need for more sophisticated gadgets has hassled the markets. These equipment's characterized by factors such as high efficiency and being light-weight, tend to face resonance situations more frequent, hampering their performances. Knowing the natural frequency not only helps to suppress resonance but also assists to deduce the speed of other machines parts to avoid resonance. It might be challenging to develop a mathematical model of the system in practical situations and predict its vibration characteristics. In such cases, we make use of experimental models to

measure the vibration response of the system through a known input, thus helping in identifying the system regarding its mass, stiffness, and damping. The computational process adopted to measure natural frequencies have different values when compared to the practical situation because of the assumptions made during analysis [7]. Machines are put under certain environment to experience specific vibration, and their sustainability decides whether they can survive the practical situations. These events and circumstances make vibration measurement an important issue. Basic vibration measurement scheme is outlined in Figure 1.1.



Figure 1.1: Basic vibration measurement scheme

Vibration measurement is done in following way: transducers are employed to convert the vibration of the structure to an electrical signal. These electrical signals in the form of voltage are too small for direct recording, and hence a signal conversion instrument is used to amplify the signal to required values. The output signals can be recorded through a computer or stored in a display unit for visual inspection. The data recorded in the form of signals undergo analysis to determine the vibration characteristics of the structure. During vibration testing, it is important to consider certain factors such as the frequency ranges and amplitudes with the substantiality of the structure involved along with operational conditions imposed on the machine, and the type of data processing as the output can be in the form of graphical representations or digital recording for further analysis.

Vibration measurement is sometimes used as an indirect measurement of some other value, as the final measurement goal determines the approach to obtaining the vibration response. Often, condition monitoring process is used to predict or monitor wear, fatigue, and failure which in turn assist in machine maintenance. Condition monitoring also called inertial vibration [8]. E.g., monitoring machinery motors (especially the bearings) in critical applications.

1.2.2 Types of vibration and measurements

Free Vibration happens when a system, after an initial disturbance, is left to vibrate on its own, the ensuing vibration is known as free vibration, and no external force acts on the system. An example of free vibration is the oscillation of a simple pendulum. Forced Vibration occurs when a system is subjected to an external force, i.e., an impact or often a repeating type of force, the resulting vibration is known as forced vibration. A condition known as resonance takes place when the frequency of the external force coincides with one of the natural frequencies of the system, and the system undergoes large oscillations. Failures of such structures as bridges, buildings, turbines blades and airplane wings have been associated with the occurrence of resonance phenomenon.

When no energy is lost or dissipated during oscillation in the form of friction or other resistance, the vibration is known as undamped vibration. However, it is called damped vibration in case of energy loss. In many physical systems, the amount of damping is so small that it can be considered as negligible and disregarded for most engineering purposes. However, during analysis of vibrating systems, the consideration of damping becomes extremely important.

Vibration is known as linear vibration when all the basic components of a vibratory system, i.e. the spring, the mass, and the damper behave linearly. If any of the basic components behave nonlinearly, the vibration is termed as nonlinear vibration. The differential equations governing the behavior of such linear and nonlinear vibratory systems are also linear and nonlinear, respectively. Linear vibration holds the principle of superposition and the mathematical techniques of analysis are well developed. For nonlinear vibration, the superposition principle is not valid, and thus, the techniques of analysis are less known. With increasing amplitude of oscillation, all vibratory systems tend to behave nonlinearly. Hence knowledge of nonlinear vibration is desirable while dealing with practical vibratory systems.

If at any given time the value or magnitude of the excitation (force or motion) acting on a vibratory system is known, the excitation is known as deterministic. Therefore, the resulting vibration is known as deterministic vibration. Wind velocity, road roughness, and ground motion during earthquakes are categorized under random vibration. When excitation is random, the resulting vibration is also called as random vibration. In the system with the random vibratory response; the excitation can be described only regarding statistical quantities.

Different measurement technologies have merits and demerits depending on the ultimate vibration response goals. Continuous vibration measurements are used for condition monitoring of machines. It directly measures the dynamic characteristics of the object of interest under real operating conditions, also facilitating in real-time maintenance and preventing failure. An impulse vibration measurement involves striking the object, often with a “hammer” that measures impact force and then measuring the resulting

vibration of the object. This type of test reveals resonances and help predict its behavior in real operating conditions. It often leads to design considerations to either avoid or accentuate resonant frequencies depending on the application. There is non-contact type displacement sensors that measure displacement without being in contact with the vibrating structure. The types of sensor used for vibration measurement are discussed in the following part of this section. With instantaneous vibration focusing on obtaining the limited vibration response of particular instance on the structure whereas total vibration measurement involves measuring the total vibration response of the structure.

1.2.3 Types of sensors

During vibration the structure vibrating undergoes physical change about its resting position and measuring this change is termed as vibration measurement. The transducer is a device that transforms values of physical variables into the equivalent electrical signal. Figure 1.2 shows the strain gauge functioning under tension and compression. A strain gauge is one of the transducers; construction of a strain gauge includes a fine wire of copper-nickel alloy, sandwiched between two sheets of thin paper. When bonded to a vibrating structure the strain gauge experiences the same motion as that of vibrating structure is attached to and thus the change in strain experienced by the gauge results in a change in resistance, producing the electrical signals equivalent to the strain experienced. The strain at any point on the structure is proportional to the structural deflection thus can be calibrated to read strain directly. To measure the change in resistance of the wire, the strain gauge is accompanied by Wheatstone bridge, potentiometer or voltage divider. Transducers facing problems such as nonlinearity or slow response find less application in vibration measuring field.

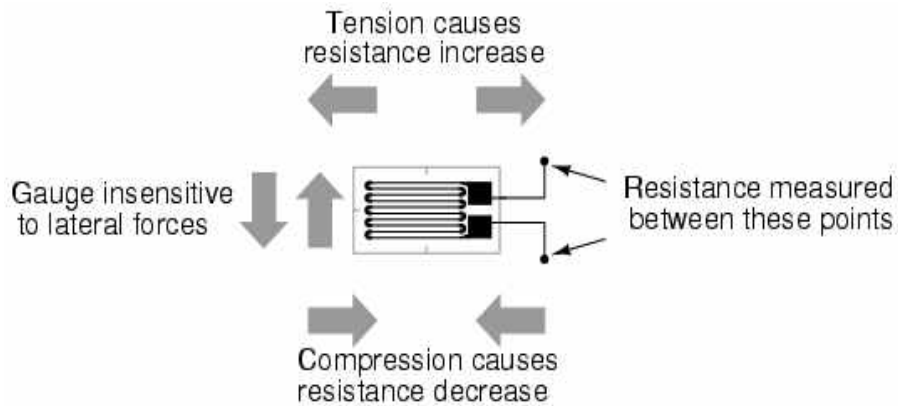


Figure 1.2: Strain gauge

For accurate surface strain and temperature measurements for propulsion systems, techniques have advanced through the development of thin strain gauges and thermocouples sensors few micrometers thick ($5 - 8 \mu m$), sputter deposited directly on test structure without any structural alteration and minimal gas flow disturbances in an environment such as furnace testing and harsh engine conditions. [9]. There are certain materials like quartz, tourmaline, lithium sulfate and Rochelle **salt** that directly generate an electrical signal when subjected to deformation or mechanical stress and the charge disappears when the material is back to its original shape. These materials are termed as a piezoelectric material, and the transducer with such material is termed as a piezoelectric transducer. Researchers have studied the behavior of piezoelectric elements as strain sensors. Strain developed in the testing structure is measured regarding electric charge generated by the piezoelectric element as a direct effect of piezoelectricity. A typical example of a piezoelectric transducer is an accelerometer, enclosed with a small spring-loaded mass against a piezoelectric crystal used to measure the acceleration of vibrating

body. Different accelerometers from PCB Piezotronics are shown in Figure 1.3. When the base to which the accelerometer is attached vibrates, the mass experiences the changes in



Figure 1.3: PCB Accelerometer

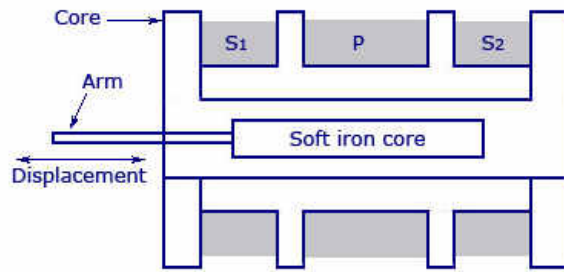
acceleration, hence the output voltage generated by the crystal will be proportional to the acceleration of the vibrating structure. The main advantages of the piezoelectric accelerometer include compactness, ruggedness, high sensitivity, and high-frequency range. An accelerometer is a point sensor requiring multiple readings to measure total deformation of a structure undergoes. Accelerometers are used to measure the acceleration of the vibrating surface and the frequency response generated is used to determine the dynamic characteristics such as natural frequency, mode shapes and damping ratio. [10]. It is to be noted that accelerometers are point sensor and thus multiple accelerometers are needed to be embedded on the vibrating surface to derive the frequency response determining the dynamic characteristics. The accelerometer also finds application in basic activity recognition [11] such as walking, running and similar activities.

Linear variable differential transformer (LVDT) consisting of a primary coil in the center with two secondary coils at each end, connected in opposite phase to the center coil, and magnetic core free to move in an axial direction. With core positioned in the center, the two Secondary coils are equal with 180° out of phase, thus making the LVDT output voltage as zero. Figure 1.4 (a) shows the schematic diagram of LVDT and Figure 1.4 (b) represents a displacement LVDT from OmegaTM. With the core movement in either direction resulting in a change of magnetic coupling i.e, increased magnetic coupling on the side where the core moves and decreased coupling on the opposite side. The output of LVDT depends on the directional magnetic core movement. The output voltage from LVDT varies linearly with displacement and hence the name LVDT (this apply until the core is not moved far away from the center coil). The LVDT offers its displacement range from 0.0002 to 40 cm. It includes advantage such as insensitivity to temperature, but the magnetic core restricts its use at higher frequencies.

Non-contact displacement sensors are mounted with a small gap between the sensor (probe) and the vibrating surface. Non-contact displacement sensors are categorized as: eddy current, capacitive and optical sensors, where the choice of the sensor depends upon the environmental conditions in which the sensor is placed [12] and these sensors are shown in Figure 1.5. The sensors not being mounted on the object, hence do not interfere with the object's mass or its resonant characteristics. The output is not affected by the frequency of the vibration; therefore, more accurate measurements are recorded across the frequency spectrum.

A transducer, when used in conjunction with another device to measure vibration, is known as a vibration pickup. Seismic instrument formulated with the mass-spring-

damper system is commonly used as vibration pickups; measuring displacement of the mass concerning the base it is mounted on. A vibrometer or seismometer is a device used to measure the displacement of the vibrating structure as shown in Figure 1.6.



(a) Basic construction of LVDT



(b) Omega™ Displacement LVDT sensor

Figure 1.4: Linear variable differential transformer (LVDT)



(a) AkuSense Eddy current sensor



(b) Capacitive sensor



(c) Sycamore Optical sensor

Figure 1.5: Noncontact Displacement sensors



Figure 1.6: Sper Scientific Direct Vibrometer model 840060

Mechanical type frequency measuring instruments are based on the principle of resonance. Single-Reed Instrument or Fullarton Tachometer is built with a variable length cantilever strip and mass attached at one end and clamped at the other end with a screw mechanism to change the free length. Then the reed is marked based on natural frequency along its length in such a way that when the excitation frequency matches the natural frequency, a direct reading is obtained. A Multireed-Instrument or Frahm Tachometer is

constructed on the same principle as the single reed, except with the fact that multireed has a multiple number of cantilever strip useful to measure a wide range of frequencies.

The stroboscope is a device that produces light pulse intermittently, and the frequency of the light pulse can be altered and read. Figure 1.7 represents a stroboscope. When a specific point on a rotating (Vibrating) structure is viewed with the help of the stroboscope, it will appear to be stationary only when the frequency of the pulsating light is equal to the speed of the rotating (vibrating) structure. Lowest frequency captured through this instrument is up to 15 Hz.



Figure 1.7: Reed K4030 Digital Stroboscope.

1.2.4 Vibration Exciters

The exciter may be impact hammer or an electromagnetic shaker. The response can be measured easily with the help of electrodynamic shaker as it can provide large input forces. The mass loading effect in case of the electrodynamic shaker should be taken care off. The vibration exciters or shakers are used in applications such as determination of the

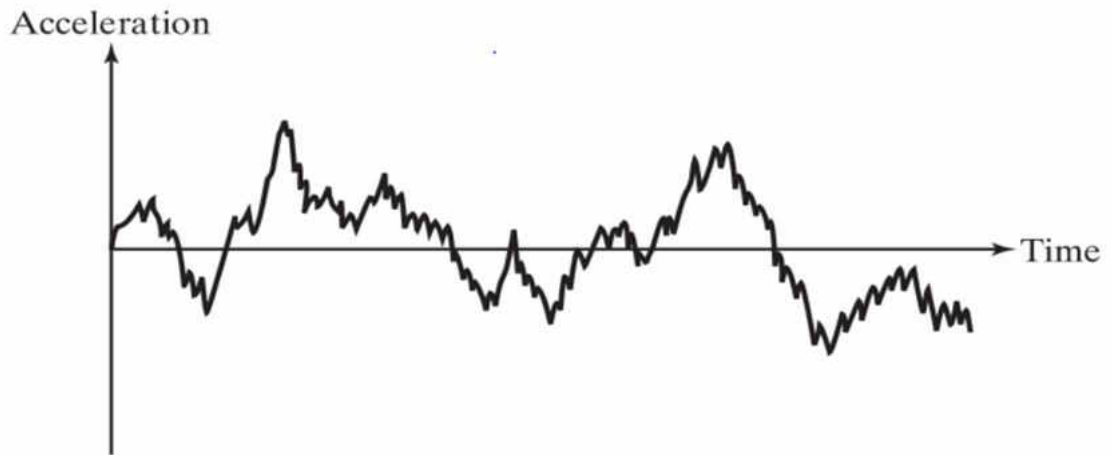
dynamic characteristics of machines and structures, and fatigue testing of materials. There are various types of vibration exciters like the mechanical, electrodynamic or hydraulic type. In small shakers, the magnetic field is produced by a permanent magnet while electromagnet is used in larger ones like the one in Figure 1.8. Another traditional method of exciting the structure is the impact hammer with an inbuilt force transducer in its head. The mass of the hammerhead and impact velocity contributes to the force generated to excite the structure.



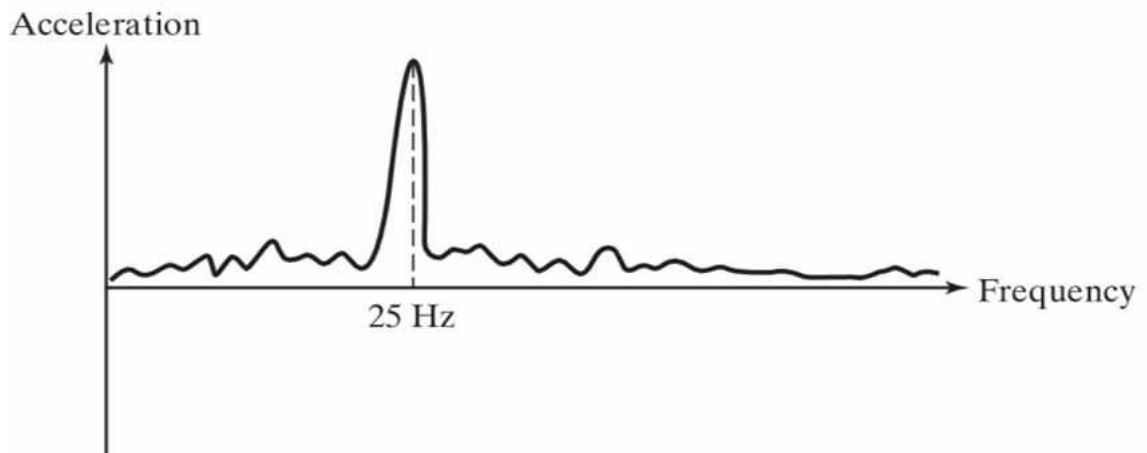
Figure 1.8: Labworks ET-126 Electrodynamic shaker.

1.2.5 Signal Analysis

Signal conditioners, in the form of charge or voltage amplifiers, are used to match and amplify the signals before analysis. After conditioning, the response signal is sent to an analyzer for processing. In signal analysis, we determine the response of a system under a known excitation force and represent the response in a convenient form. The time response of a system will not provide insight to the response. Frequency response will show one or more discrete frequencies where energy is concentrated. The acceleration-time history of a machine frame subjected to excessive vibration gives a graph (as shown in Figure 1.9 (a)) that cannot be used to identify the cause of vibration. If the acceleration-time history is transformed to the frequency domain (as shown in Figure 1.9 (b)), it shows energy concentration at location where the peaks represent the natural frequencies of the vibrating structure. Real-time analyzers find their application in machinery health monitoring, as a change in the vibration spectrum can be observed at the same time when an actual change occurs in the machine. Real-time analysis procedures can be differentiated into two types: the digital filtering method and the fast Fourier transform (FFT) method. Fast Fourier Transform (FFT) analyzer is used where the analyzer receives the analog voltage signals from the conditioning process for computations.



(a) Shows the acceleration-time graph of machine frame subjected to excessive vibration.



(b) Frequency-domain with peak representing natural frequency of vibrating structure

Figure 1.9: Time domain and frequency domain graph.

FFT is performed by an analog-to-digital (A/D) converter (which is part of a digital analyzer). It computes the discrete frequency spectra of individual signals and cross-spectra between the input and the output signals thus determining the natural frequencies, damping ratios, and mode shapes in either numerical or graphical form. Digital analyzers have become quite popular for real-time signal analysis where the signal is continuously analyzed over all the frequency bands. The frequency bandwidth of these analyzers

depends on the manufacturers and range from few kHz to 100 kHz. Figure 1.10 shows a digital analyzer from Keysight Technologies.

When the machine starts developing faults, the shape of the frequency spectrum changes. Hence the nature and location of the fault can be detected by comparing the frequency spectrum of the machine in damaged condition concerning the frequency spectrum of the machine in good condition.

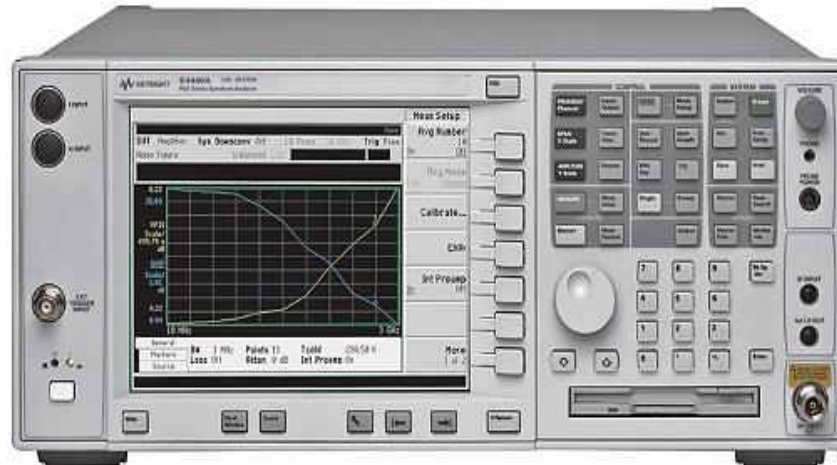


Figure 1.10: E4440A PSA Spectrum Analyzer, 3 Hz to 26.5 GHz

1.2.6 Modal Analysis

Experimental modal analysis, also known as modal testing, deals with determining the natural frequencies, mode shapes, and damping ratios through vibration testing. In vibrating structure, when the forcing frequency equals the natural frequency of the structure (almost no damping), a sharp peak response exhibited (known resonance) and the output of this process is termed as FRF (Frequency Response Function). Measuring this FRF over a period of time is termed as Modal Analysis. As the forcing frequency crosses the natural

frequency of the structure the response phase changes by 180° with the phase at 90° resonance.

Modal analysis process requires an exciter to apply input force to the structure and a sensor converting the physical motion of the structure to an electrical signal. An amplifier controlling the input signal to set the structure into vibration and a digital analyzer to display the frequency response [13].

In an Undamped-Multidegree-of-Freedom System, the equations of motion of a system in physical coordinates are represented by

$$[m]\{\ddot{\vec{x}}\} + [k]\{\vec{x}\} = \{\vec{f}\} \quad (1.1)$$

Where m refers to the mass matrix of the system, $\ddot{\vec{x}}$ stands for acceleration of mass, k refers to stiffness constant, \vec{x} refers to displacement of mass and \vec{f} refers to the force acting on the mass. Therefore, for free harmonic vibration, Eq. (1.1) becomes

$$[[k] - \omega_i^2[m]]\{\vec{y}_i\} = 0 \quad (1.2)$$

Where ω_i stands for the i^{th} modal frequency and \vec{y}_i is the corresponding mode shape. The orthogonality relations for the mode shapes can be represented as

$$[Y]^T[m][Y] = \text{diag}[M] = [\wedge M_{i\setminus}] \quad (1.3)$$

$$[Y]^T[k][Y] = \text{diag}[K] = [\wedge K_{i\setminus}] \quad (1.4)$$

Where $[Y]$ & $[Y]^T$ refers to modal matrix & transpose modal matrix respectively, containing the modes $\vec{y}_1, \vec{y}_2, \vec{y}_3, \dots \dots y_N$ as columns (N refers to the number of measured natural frequencies), M_i and K_i are the elements of diagonal matrix $[M]$ and $[K]$

respectively for the i^{th} mode. M_i and K_i also known as the modal mass and modal stiffness of the i^{th} mode.

$$\omega_i^2 = \frac{K_i}{M_i} \quad (1.5)$$

When harmonic force applied, $\{\vec{f}(t)\} = \vec{F}e^{i\omega t}$, with $\tilde{t} = \sqrt{-1}$, Eq. (1.4) can be written as

$$\vec{x}(t) = \vec{X}e^{i\omega t} = \left[[k] - \omega_i^2 [m] \right]^{-1} \vec{F}e^{i\omega t} \equiv [\alpha(\omega)] \vec{F}e^{i\omega t} \quad (1.6)$$

Where \vec{x} is complex amplitude independent of time and \vec{X} & $e^{i\omega t}$ are the magnitude and phase respectively. $\alpha(\omega)$ refers to receptance matrix or the frequency-response function of the system. Now using the orthogonality relations as expressed in Eq. (1.3) and Eq. (1.4) we can express $\alpha(\omega)$ as

$$[\alpha(\omega)] = [Y][[K] - \omega^2[M]]^{-1}[Y]^T \quad (1.7)$$

The harmonic response of one coordinate, X_p is denoted by an individual element of the matrix lying in row p and column q, caused by a harmonic force applied at another coordinate, F_q (with no other forces), can be expressed as

$$\begin{aligned} \alpha_{pq}(\omega) &= [\alpha(\omega)]_{pq} = \frac{X_p}{F_q} \Big|_{\text{with } F_j=0; j=1,2,\dots,N; j \neq q} \\ &= \sum_{i=1}^N \frac{(\vec{y}_i)_p (\vec{y}_i)_q}{K_i - \omega^2 M_i} \end{aligned} \quad (1.8)$$

where $(\vec{y}_i)_p$ denotes the j th component of mode \vec{y}_i and ω refers to natural frequency of system. If the modal matrix $[Y]$ is further normalized as

$$[\Phi] \equiv [\phi_1 \phi_2 \dots \phi_N] = [Y][M]^{-0.5} \quad (1.9)$$

Where Φ is the normalized mode matrix and $\phi_1, \phi_2 \dots \phi_N$ are the normalized mode shapes. With the normalized mode shapes, Eq. (1.8) becomes

$$\alpha_{pq}(\omega) = \sum_{i=1}^N \frac{(\vec{\phi}_i)_p (\vec{\phi}_i)_q}{\omega_i^2 - \omega^2} \quad (1.10)$$

Where $\alpha_{pq}(\omega)$ represents the receptance matrix with individual element of matrix lying in the row p & column q and $(\vec{\phi}_i)_p$ denotes the pth component of mode $\vec{\phi}_i$. The equations of motion of a damped multidegree-of-freedom system in physical coordinates can be expressed as

$$[m]\{\ddot{\vec{x}}\} + [c]\{\dot{\vec{x}}\} + [k]\{\vec{x}\} = \{\vec{f}\} \quad (1.11)$$

Where $[c]$ represents the damping matrix with $\dot{\vec{x}}$ as the velocity. We assume proportional damping for simplicity, therefore, that the damping matrix $[c]$ can be written as

$$[c] = a[k] + b[m] \quad (1.12)$$

Where a and b are constants. Then the undamped mode shapes of the system diagonalize not only the mass and stiffness matrices shown in Eq. (1.3) and Eq. (1.4), but also the damping matrix as shown in Eq. (1.13)

$$[Y]^T [c] [Y] = \text{diag}[c] = [\hat{C}_i] \quad (1.13)$$

C_i represents the element of diagonal matrix $[c]$ and $[\hat{C}_i]$ represents the modal constant matrix of i^{th} mode. Here the mode shapes of the damped system will be the same as those of the undamped system except the natural frequencies will change and in general become complex. In Eq. (1.11) the forcing vector is assumed to be harmonic. Therefore, the frequency-response function or receptance can be expressed as

$$\alpha_{pq}(\omega) = [\alpha(\omega)]_{pq} = \sum_{i=1}^N \frac{(\vec{y}_i)_p (\vec{y}_i)_q}{K_i - \omega^2 M_i + i\omega C_i} \quad (1.14)$$

On including the mass-normalized mode shapes from Eq. (1.8), the frequency response or receptance becomes

$$\alpha_{pq}(\omega) = [\alpha(\omega)]_{pq} = \sum_{i=1}^N \frac{(\vec{\phi}_i)_p (\vec{\phi}_i)_q}{\omega_i^2 - \omega^2 + 2i\zeta_i \omega_i \omega} \quad (1.15)$$

ζ_i , refers to the i^{th} mode damping ratio,

1.3 Origin of piezoelectricity and applications

The word ‘piezo’ is derived from the Greek word for pressure, hence the word piezoelectricity means electricity resulting from pressure, it’s the ability of a material to generate a voltage in response to stress and develop strain in response to the applied electric field. Piezoelectricity and ferroelectricity properties were found in PVDF material [14]. The piezoelectric effect was discovered by, Jacques and Pierre Curie in 1880. Their experiment consisted of crystals of tourmaline, quartz, topaz, cane sugar and Rochelle salt subjected to mechanical stress. In 1920, the first application of this technology was implemented in quartz transmitter and receiver for underwater sound (first sonar) by Frenchman, Langevin. By 1960’s, a weak piezoelectric effect was exhibited by whalebone and tendon which indulged the researchers to search for other materials possessing such property. By 1969, a high level of piezo activity was detected amongst the polyvinylidene fluoride (PVDF). Also, nylon and PVC exhibit the effect, but none claim to be as highly piezoelectric as PVDF and its copolymers. PVDF structures are made of long chains of repeating monomer $(-Ch_2 - CF_2 -)$. The inherent dipole moment exists within each monomer unit as the hydrogen atoms have positive charge whereas fluorine atoms have

negative charge with respect to carbon atoms. PVDF also being pyroelectric produces an electric charge in response to temperature change too. Strongly absorbs infrared energy in range 7-20 μ m wavelength which is the same wavelength spectrum representing human body heat. With this we see applications of PVDF material as sensor, exhibiting direct piezoelectric effect in the next section.

1.3.1 Sensors

PVDF films are useful to detect early damage in wind turbine blades [15] where several film sensors were installed on the component skin and the behavior of these sensors were examined under opening and closing loads. As pressure sensor, accompanied by a wide working temperature range, preferably from -40 to $+125$ °C, long working life: more than 10 years and 100 million pressure cycles along a pressure range from 10kPa till 2 MPa with about 10% accuracy and about 1ms response time [16]. PVDF as a pressure sensor senses the input, output and near the valve pressure, which notifies whether the valve functions as expected, thus an effective way to monitor the valve functioning. Development of novel wearable cardiorespiratory signal sensor device for monitoring sleep conditions [17] like sleep apnea. PVDF thin film with one layer is used as 3D force sensor [18] measuring the stress in three principle directions. PVDF film used as a sensor in detecting respiratory disorder like bronchial asthma by analyzing the recorded breathing pattern through imping exhale air on the PVDF sensor to sense the breath patterns [19]. Other wearable gadgets include; pulse detection in the form of finger clip and/or wrapped around the wrist, and in measuring the physical response of muscle. Piezoelectricity of PVDF material can also be exhibited as actuators in the form of indirect piezoelectric effect, and thus we see applications of PVDF as actuators in the following section.

1.3.2 Actuators

PVDF material also functions as an actuator. In a loudspeaker, the voltages are converted to mechanical movement of the piezoelectric film. A similar concept is applicable to the headphones. Other general application includes; printers where the cartilage has a circuit at bottom consisting of a piezoelectric material which deforms as the electrical signal is converted to mechanical energy, hence causing the nozzle to deflect. Lighter utilizes the mechanical energy generated by the fingers pressing the trigger, as this causes the piezoelectric material beneath to deflect which in return generates electrical signal resulting in a flame. Watch having a quartz crystal which mechanically oscillates deforming at a constant frequency and transducing mechanical energy to an electrical signal. Samsung keyboard has piezoelectric device beneath the keys. Pressing the keys causes deformation of the piezo material producing electric charge. In case of cellphone battery runs out, you can vigorously press the keys on the keypad generating some electric charge capable of charging the battery to make a call (though not applicable to the touch screen phones available these days). The next section highlights the field of application for PVDF material.

1.3.3 Field of application

Variety of application can be seen in the field of active noise and vibration, Material characterization [20], Medical fields [21] like Pacemaker activity motion sensor-acceleration, etc. In the field of monitoring structural health and design fatigue, where sensors with a response time of about several nanoseconds along with frequency range from 0.001Hz to 2GHz are used [22]. Extending its application to manufacturing industries for monitoring of dynamic cutting torque in single-point cutting processes [23]. PVDF as

an actuator, behaves as a vibrating membrane used for fatigue test of thin film [24] and control vibration of a cylindrical shell [25]. PVDF film is much superior to the foil type strain gage in term of signal conditioning requirement, especially in applications with low strain levels and high noise levels. Vibration measurement is useful in monitoring the deflection curve of the structure to derive the design fatigue life and call for the need of maintenance, of the structure, i.e., structural health and fatigue design monitoring of traffic sign structural support vibrations [26]. Use of PVDF material in various fields is possible due to its properties, and hence these properties are presented in the following section.

1.3.4 PVDF Properties

With high pyroelectric and piezoelectric coefficients, PVDF has excellent mechanical properties, high chemical resistance and good thermal stability facilitating easy processing of PVDF films [27]. PVDF film possesses exceptionally high mechanical performance and belonging to the family of ultra-light structural materials hence find a place in the manufacturing of aircraft parts [28]. Polymer-based composite materials belong to the family of ultra-light structural materials are used massively not only in military and civil aircraft, but in other fields like civil and automotive engineering as well [29]. It could also be used to encompass a large area of the vibrating surface as it is potentially inexpensive and could also generate voltages 10–25 times higher than that of piezoceramics at the same input pressure [30]. Apart from being lightweight and flexible, the PVDF film extends its properties as a transducer by possessing high elastic compliance with a dynamic range of 10^{-8} to 10^6 *psi* [22]. Low acoustic impedance followed by higher mechanical strength and impact resistance of $10^9 - 10^{10}$ *Pascal modulus*. High dielectric strength is helping to withstand strong fields, whereas most piezo ceramics would

depolarize. Highly stable, resisting most chemical, oxidants, moisture, ultraviolet and nuclear radiation. And most importantly easily fabricated and applicable to a variety of test specimens. Being non-reactive, can be glued by commercial adhesives. PVDF has Young's modulus approximately $1/12^{th}$ that of aluminum, least likely affecting the dynamics as the aluminum beam stiffness is much greater than that of the PVDF film. Using piezo ceramics in absence of the thin film sensors would add a degree of complexity to the system for measuring the surface parameters such as stress, strain and temperature. They also eliminate the need for machining surfaces for sensor installation like the wire or foil sensors. With negligible mass and minimal gas flow disturbance over specimen surface these sensors have minimal impact on stress, strain, thermal and vibration pattern within the operational limits. PVDF is unaffected by water but the electrodes are vulnerable to such conditions leading to low Z bridging, the shortening of the electrode circuit. Human body is good antenna for picking up 50/60 Hz hence sensor shielding is required. The material is flexible to accommodate the required shape but not stretchable. High amount of force necessary to stretch the film even by 2%. The properties exhibited by the piezoelectric film: Design Flexibility, dynamic range, dimensional properties and ease to fabricate and apply to structure make it favorable to be used as a sensor in this work. After studying aspects of PVDF as sensors and actuators, and the field of applications we move to the thesis layout, outlining the processes to be carried out to successfully establish PVDF film as a sensor to measure deflection curve of vibrating beams and plates.

1.4 Thesis Layout

The processes involved in the research are as follows: starting with the equation of a PVDF film attached on arbitrary structures, sensor equation for the plate and beam with

general boundary conditions are derived under sensor design section in Chapter II. The sensor along with plate equations and beam equations are discretized for numerical simulations through MATLAB in numerical simulation section 3.1 and 3.2, followed by ANSYS further assisting in performing Multiphysics simulations as illustrated in sensor simulation section 3.3.3, under Chapter III. Finally, in Chapter IV, experimental procedure demonstrates the experimental setup and application of various boundary conditions to the beam. Whereas, the plate is constrained to clamped-clamped boundary condition only. In the final chapter i.e. Chapter V, the results conclude the PVDF film as effective and affordable means of measuring deflection curve of the vibrating plate and beam.

CHAPTER II

PIEZOELECTRIC SHELL VIBRATION THEORY

This chapter further discusses the general piezoelectric shell vibration theory, followed by the development of general output charge equation for the PVDF film. The generic output charge equation is then applied to the different structures to derive the respective output charge equations.

2.1 Fundamentals

In the following section, derivations of generic piezoelectric shell theories are reviewed based on linear piezoelectricity and Hamilton's principle presented by Tzou [31]. Figure 2.1 depicts a generic piezoelectric shell continuum defined in a tri-orthogonal curvilinear coordinate system where α_1 and α_2 define the shell neutral surface and α_3 the normal direction. The shell sensor has a constant thickness h^s which is very thin as compared to the shell structure and its radii of curvatures, R_1 and R_2 , such that the strains in the film are assumed constant and equal to the outer surface strains of the shell. U_1 , U_2 , and U_3 represent the generic deflections: in three principal directions, respectively: α_1, α_2 , and α_3 , are assumed to be small. The piezoelectric sensor is perfectly coupled with the shell continuum, not change its dynamic characteristics.

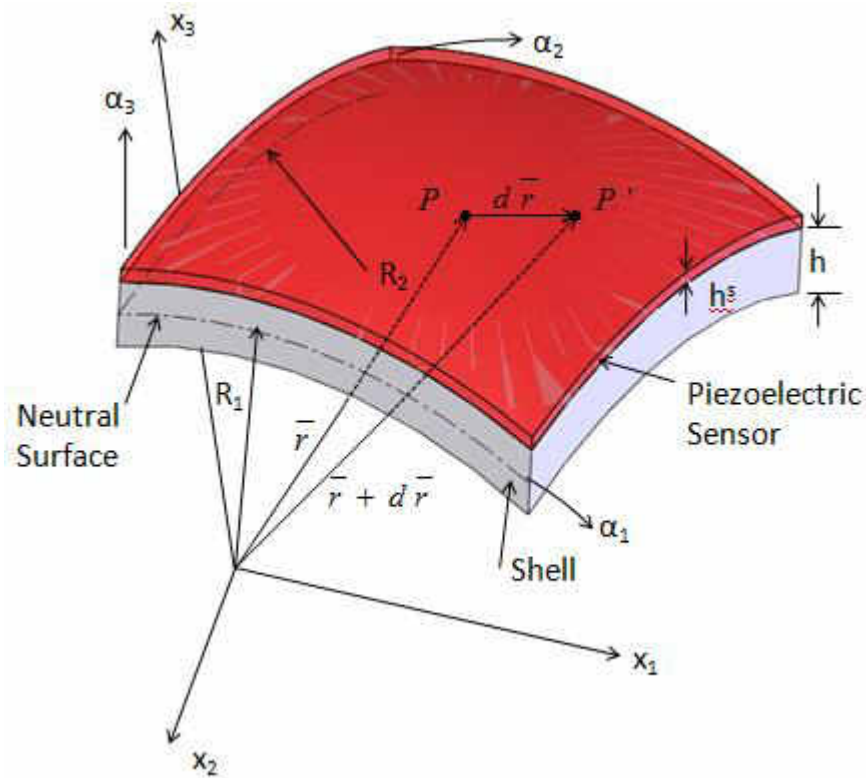


Figure 2.1: Representation of piezoelectric sensor bonded to a shell structure.

Here are some fundamental physical laws defined, including Hamilton's principle which is the fundamental basis of all theoretical derivations performed. Hamilton's principle is written as:

$$\delta \int_{t_0}^{t_1} dt [\hat{K} - \hat{U}] = 0 \quad (2.1)$$

Where \hat{K} represents the kinetic energy; \hat{U} represents the total potential energy (inclusive of mechanical energy, electric energy, and work was done by externally applied forces and charge); δ represents the variation concerning the variable that follows, in this case kinetic energy and total potential energy. In case of a piezoelectric continuum subjected to a

prescribed surface traction t and a surface charge per unit area Q , Hamilton's principle states:

$$\delta \int_{t_0}^{t_1} dt \int_V \left[\frac{1}{2} \rho \dot{U}_j \dot{U}_j \right] dV - \left\{ \int_{t_0}^{t_1} dt \int_V [H(S_{ij}, E_j)] dV - \int_{t_0}^{t_1} dt \int_S (t_j \delta U_j - Q_j \delta \phi) dS \right\} = 0 \quad (2.2)$$

where the electric enthalpy is defined by $H(S_{ij}, E_j)$; mass density by ρ ; deflection U_j in the α_j direction; mechanical strain S_{ij} , of the i^{th} surface and the j^{th} direction; electric field strength as E_j in the α_j direction; surface charge by Q_j ; electric potential by ϕ ; piezoelectric volume considered as V ; S is the surface over the volume. The relation between electric field E_j and potential ϕ in the curvilinear coordinate system are defined as:

$$E_1 = \frac{1}{A_1 \left(1 + \frac{\alpha_3}{R_1} \right)} \frac{\partial \phi}{\partial \alpha_1} \quad (2.3)$$

$$E_2 = \frac{1}{A_2 \left(1 + \frac{\alpha_3}{R_2} \right)} \frac{\partial \phi}{\partial \alpha_2} \quad (2.4)$$

$$E_3 = -\frac{\partial \phi}{\partial \alpha_3} \quad (2.5)$$

Where the Lamé parameters are from the fundamental equation are represented as A_1 and A_2 :

$$(ds)^2 = A_1^2 (d\alpha_1)^2 + A_2^2 (d\alpha_2)^2 \quad (2.6)$$

A_1 and A_2 may also be considered as the fundamental form parameters and, R_1 and R_2 are the radii of curvatures of α_1 and α_2 axes, respectively. The Lamé parameters are named after the French mathematician, Gabriel Lamé, known for his work in curvilinear coordinates. The infinitesimal distance between points P and P' can be defined on the neutral surface, from Figure 2.1. The differential change $d\bar{r}$ of the vector \bar{r} moving from P to P' is $d\bar{r} = \frac{d\bar{r}}{\partial\alpha_1} d\alpha_1 + \frac{d\bar{r}}{\partial\alpha_2} d\alpha_2$. The magnitude ds of $d\bar{r}$ is obtained by

$(ds)^2 = d\bar{r} \cdot d\bar{r}$. The following can be defined which produces Eq. 2.6:

$$\frac{\partial\bar{r}}{\partial\alpha_1} \cdot \frac{\partial\bar{r}}{\partial\alpha_1} = \left| \frac{\partial\bar{r}}{\partial\alpha_1} \right|^2 = A_1^2 \quad \text{and} \quad \frac{\partial\bar{r}}{\partial\alpha_2} \cdot \frac{\partial\bar{r}}{\partial\alpha_2} = \left| \frac{\partial\bar{r}}{\partial\alpha_2} \right|^2 = A_2^2. \quad (2.6.1)$$

In general, linear piezoelectric relations of a piezoelectric continuum can be described as:

$$\begin{aligned} \{T_{ij}\} &= [c] \{S_{ij}\} - [e]^t \{E_j\} \\ \{D_j\} &= [e] \{S_{ij}\} + [\epsilon] \{E_j\} \end{aligned} \quad (2.7)$$

where $\{T_{ij}\}$ represents the stress vector induced by mechanical and electrical effects [31].

$[c]$ represents the elastic constant matrix; $[e]$ represents the piezoelectric constant matrix;

$\{S_{ij}\}$ represents the mechanical strain of the i^{th} surface in the j^{th} direction; $\{E_j\}$

represents the electric field strength in the α_j direction; $\{D_j\}$ represents the electric

displacement vector; $[\epsilon]$ represents the dielectric constant matrix. The converse

piezoelectric effect and the direct piezoelectric effect are denoted by Eq. (2.7). An applied

mechanical force results in the internal generation of electrical charge leading to direct

piezoelectric effect. Whereas the internal generation of a mechanical strain due to an applied electrical field leads to converse piezoelectric effect [32]. A piezoelectric material with a symmetrical hexagonal structure ($C_{6v} = 6mm$) in the transverse α_3 is isotropic but is anisotropic in the α_1 and α_2 directions. The material expands along the axis of polarization, i.e. the thickness direction, when an electric field having the same polarity and orientation as the original polarization field is placed across the thickness of a piezoelectric shell, and contracts perpendicular to the axis of polarization. When polarized in the thickness direction, $[c]$, $[e]$, and $[\epsilon]$ matrices are defined as [31]:

$$[c] = \begin{bmatrix} c_{11} & c_{12} & c_{13} & 0 & 0 & 0 \\ c_{12} & c_{11} & c_{13} & 0 & 0 & 0 \\ c_{13} & c_{13} & c_{33} & 0 & 0 & 0 \\ 0 & 0 & 0 & c_{44} & 0 & 0 \\ 0 & 0 & 0 & 0 & c_{44} & 0 \\ 0 & 0 & 0 & 0 & 0 & c_{66} \end{bmatrix} \quad (2.8)$$

$$[e] = \begin{bmatrix} 0 & 0 & 0 & 0 & e_{15} & 0 \\ 0 & 0 & 0 & e_{24} & 0 & 0 \\ e_{31} & e_{32} & e_{33} & 0 & 0 & 0 \end{bmatrix} \quad (2.9)$$

$$[\epsilon] = \begin{bmatrix} \epsilon_{11} & 0 & 0 \\ 0 & \epsilon_{11} & 0 \\ 0 & 0 & \epsilon_{33} \end{bmatrix} \quad (2.10)$$

Where $c_{66} = (c_{11} - c_{12})/2$. Note $e_{31} = e_{32}$ for the 6mm structure. And $e_{24} = e_{15}$, if a piezoelectric material is electrically polarized, but is not mechanically stretched in the process. Based on the above matrices, enthalpy H can be written as:

$$\begin{aligned}
H &= \frac{1}{2} (\sigma_{11} S_{11} + \sigma_{22} S_{22} + \sigma_{12} S_{12} + \sigma_{13} S_{13} + \sigma_{23} S_{23} + \sigma_{33} S_{33}) \\
&- (e_{15} E_1 S_{13} + e_{15} E_2 S_{23} + e_{31} E_3 S_{11} + e_{31} E_3 S_{22} + e_{33} E_3 S_{33}) \\
&- \frac{1}{2} (\epsilon_{11} E_1^2 + \epsilon_{11} E_2^2 + \epsilon_{33} E_3^2)
\end{aligned} \tag{2.11}$$

The strain-displacement relationships as defined in [33]:

$$\epsilon_{11} = \frac{1}{1 + \alpha_3/R_1} (\epsilon_{11}^\circ + \alpha_3 \kappa_{11}) \tag{2.12}$$

$$\epsilon_{22} = \frac{1}{1 + \alpha_3/R_2} (\epsilon_{22}^\circ + \alpha_3 \kappa_{22}) \tag{2.13}$$

$$\begin{aligned}
\epsilon_{12} &= \frac{1}{(1 + \alpha_3/R_1)(1 + \alpha_3/R_2)} \\
&\cdot \left[\left(1 - \frac{\alpha_3^2}{R_1 R_2} \right) \epsilon_{12}^\circ + \alpha_3 \left(1 + \frac{\alpha_3}{2R_1} + \frac{\alpha_3}{2R_2} \right) \kappa_{12} \right]
\end{aligned} \tag{2.14}$$

where the membrane strains are given by

$$\epsilon_{11}^\circ = \frac{1}{A_1} \frac{\partial u_1}{\partial \alpha_1} + \frac{u_2}{A_1 A_2} \frac{\partial A_1}{\partial \alpha_2} + \frac{u_3}{R_1} \tag{2.15}$$

$$\epsilon_{22}^\circ = \frac{1}{A_2} \frac{\partial u_2}{\partial \alpha_2} + \frac{u_1}{A_1 A_2} \frac{\partial A_2}{\partial \alpha_1} + \frac{u_3}{R_2} \tag{2.16}$$

$$\epsilon_{12}^\circ = \frac{A_2}{A_1} \frac{\partial}{\partial \alpha_1} \left(\frac{u_2}{A_2} \right) + \frac{A_1}{A_2} \frac{\partial}{\partial \alpha_2} \left(\frac{u_1}{A_1} \right) \tag{2.17}$$

and the change-in-curvature terms (bending strains) are further given by

$$\kappa_{11} = \frac{1}{A_1} \frac{\partial \beta_1}{\partial \alpha_1} + \frac{\beta_2}{A_1 A_2} \frac{\partial A_1}{\partial \alpha_2} \tag{2.18}$$

$$\kappa_{22} = \frac{1}{A_2} \frac{\partial \beta_2}{\partial \alpha_2} + \frac{\beta_1}{A_1 A_2} \frac{\partial A_2}{\partial \alpha_1} \tag{2.19}$$

$$\kappa_{12} = \frac{A_2}{A_1} \frac{\partial}{\partial \alpha_1} \left(\frac{\beta_2}{A_2} \right) + \frac{A_1}{A_2} \frac{\partial}{\partial \alpha_2} \left(\frac{\beta_1}{A_1} \right) \tag{2.20}$$

where β_1 and β_2 represent angles, given by

$$\beta_1 = \frac{u_1}{R_1} - \frac{1}{A_1} \frac{\partial u_3}{\partial \alpha_1} \quad (2.21)$$

$$\beta_2 = \frac{u_2}{R_2} - \frac{1}{A_2} \frac{\partial u_3}{\partial \alpha_2} \quad (2.22)$$

Substituting Eq. (2.21) and Eq. (2.22) into Eq. (2.18) gives:

$$\kappa_{11} = \frac{1}{A_1} \frac{\partial}{\partial \alpha_1} \left[\frac{u_1}{R_1} - \frac{1}{A_1} \frac{\partial u_3}{\partial \alpha_1} \right] + \frac{1}{A_1 A_2} \left[\frac{u_2}{R_2} - \frac{1}{A_2} \frac{\partial u_3}{\partial \alpha_2} \right] \frac{\partial A_1}{\partial \alpha_2} \quad (2.23)$$

Since S_{11} is equivalent to ε_{11} , then substituting Eq. (2.15) and (2.23) into Eq. (2.12) gives:

$$S_{11} = \frac{1}{1 + \alpha_3/R_1} \left(\frac{1}{A_1} \frac{\partial u_1}{\partial \alpha_1} + \frac{u_2}{A_1 A_2} \frac{\partial A_1}{\partial \alpha_2} + \frac{u_3}{R_1} \right. \\ \left. + \alpha_3 \left\{ \frac{1}{A_1} \frac{\partial}{\partial \alpha_1} \left[\frac{u_1}{R_1} - \frac{1}{A_1} \frac{\partial u_3}{\partial \alpha_1} \right] + \frac{1}{A_1 A_2} \left[\frac{u_2}{R_2} - \frac{1}{A_2} \frac{\partial u_3}{\partial \alpha_2} \right] \frac{\partial A_1}{\partial \alpha_2} \right\} \right) \quad (2.24)$$

Further simplification will give:

$$S_{11} = \frac{1}{A_1 (1 + \alpha_3/R_1)} \left(\frac{\partial u_1}{\partial \alpha_1} + \frac{u_2}{A_2} \frac{\partial A_1}{\partial \alpha_2} + u_3 \frac{A_1}{R_1} \right) \quad (2.25)$$

Similarly S_{22} & S_{33} , the normal strain components are given by:

$$S_{11} = \frac{1}{A_1 (1 + \alpha_3/R_1)} \left[\frac{\partial U_1}{\partial \alpha_1} + \frac{U_2}{A_2} \frac{\partial A_1}{\partial \alpha_2} + U_3 \frac{A_1}{R_1} \right] \quad (2.26)$$

$$S_{22} = \frac{1}{A_2 (1 + \alpha_3/R_2)} \left[\frac{\partial U_2}{\partial \alpha_2} + \frac{U_1}{A_1} \frac{\partial A_2}{\partial \alpha_1} + U_3 \frac{A_2}{R_2} \right] \quad (2.27)$$

$$S_{33} = \frac{\partial U_3}{\partial \alpha_3} \quad (2.28)$$

Substituting Eqs. (2.9) and (2.10) into (2.7) gives:

$$E_1 = \frac{1}{\epsilon_{11}} D_1 - \frac{e_{15}}{\epsilon_{11}} S_{13} = E_1^e + E_1^d \quad (2.29)$$

$$E_2 = \frac{1}{\epsilon_{11}} D_2 - \frac{e_{15}}{\epsilon_{11}} S_{23} = E_2^e + E_2^d \quad (2.30)$$

$$E_3 = \frac{1}{\epsilon_{33}} D_3 - \frac{e_{31} S_{11} + e_{31} S_{22} + e_{33} S_{33}}{\epsilon_{33}} = E_3^e + E_3^d \quad (2.31)$$

where the electric field induced by an electric displacement is denoted by E_i^e ; the electric field induced by the direct piezoelectric effect ($i=1,2,3$) is denoted by E_i^d . The two separate effects are further defined as:

$$E_i^e = \frac{D_i}{\epsilon_{ii}}, \quad (i=1,2,3) \quad (2.32)$$

$$E_1^d = \frac{e_{15}}{\epsilon_{11}} S_{13} \quad (2.33)$$

$$E_2^d = -\frac{e_{15}}{\epsilon_{11}} S_{23} \quad (2.34)$$

$$E_3^d = -\frac{e_{31} S_{11} + e_{31} S_{22} + e_{33} S_{33}}{\epsilon_{33}} \quad (2.35)$$

These fundamental definitions and mechanical/electric relations will be useful in derivations of piezoelectric shell theories. All variations in Eq. (2.2) need to be calculated in order to derive the system electromechanical equations and mechanical/electric boundary conditions of the piezoelectric shell continuum. To find these, the first step that must be looked at is the variation of kinetic energy and followed by energies associated with electric enthalpy H , as well as electric charge Q . Hence a final variation equation is derived, which leads to all electromechanical system equations and boundary conditions [31]. The variation of kinetic energy \hat{K} is given by

$$\begin{aligned}
& \delta \int_{t_0}^{t_1} dt \int_{\alpha_1} \int_{\alpha_2} \int_{\alpha_3} \hat{K} dv = \delta \int_{t_0}^{t_1} dt \int_{\alpha_1} \int_{\alpha_2} \int_{\alpha_3} \left[\frac{1}{2} \rho \dot{U}_j \dot{U}_j \right] A_1 A_2 \left(1 + \frac{\alpha_3}{R_1} \right) \left(1 + \frac{\alpha_3}{R_2} \right) d\alpha_1 d\alpha_2 d\alpha_3 \\
& = -p \int_{t_0}^{t_1} dt \int_v \left(\ddot{U}_1 \delta U_1 + \ddot{U}_2 \delta U_2 + \ddot{U}_3 \delta U_3 \right) A_1 A_2 \left(1 + \frac{\alpha_3}{R_1} \right) \left(1 + \frac{\alpha_3}{R_2} \right) d\alpha_1 d\alpha_2 d\alpha_3
\end{aligned} \tag{2.36}$$

Note that the kinetic energy variation was preceded by integration by parts.

Next, the variation of electric enthalpy is inclusive of two components: mechanical strains S_{ij} and electric fields E_j . The variation of electric-field energy is derived as:

$$\begin{aligned}
& \frac{\partial H}{\partial E_k} \delta E_k \\
& = (e_{15} S_{13} + \epsilon_{11} E_1) \frac{1}{A_1 \left(1 + \frac{\alpha_3}{R_1} \right)} \frac{\partial(\delta\phi)}{\partial\alpha_1} \\
& + (e_{15} S_{23} + \epsilon_{11} E_2) \frac{1}{A_2 \left(1 + \frac{\alpha_3}{R_2} \right)} \frac{\partial(\delta\phi)}{\partial\alpha_2} \\
& + (e_{31} S_{11} + e_{31} S_{22} + e_{33} S_{33} + \epsilon_{33} E_3) \frac{\partial(\delta\phi)}{\partial\alpha_3}
\end{aligned} \tag{2.37}$$

Applying integration by parts, the first term becomes:

$$\begin{aligned}
& \int_{t_0}^{t_1} dt \int_{\alpha_1} \int_{\alpha_2} \int_{\alpha_3} (e_{15} S_{13} + \epsilon_{11} E_1) \frac{1}{A_1 \left(1 + \frac{\alpha_3}{R_1}\right)} \frac{\partial(\delta\phi)}{\partial\alpha_1} A_1 A_2 \left(1 + \frac{\alpha_3}{R_2}\right) d\alpha_1 d\alpha_2 d\alpha_3 \\
& + \frac{\alpha_3}{R_1} \left(1 + \frac{\alpha_3}{R_2}\right) d\alpha_1 d\alpha_2 d\alpha_3 \\
& = \int_{t_0}^{t_1} dt \int_{\alpha_2} \int_{\alpha_3} (e_{15} S_{13} + \epsilon_{11} E_1) A_2 \left(1 + \frac{\alpha_3}{R_2}\right) \delta\phi d\alpha_2 d\alpha_3 \\
& - \int_{t_0}^{t_1} dt \int_{\alpha_1} \int_{\alpha_2} \int_{\alpha_3} \frac{\partial \left[(e_{15} S_{13} + \epsilon_{11} E_1) A_2 \left(1 + \frac{\alpha_3}{R_2}\right) \right]}{\partial\alpha_1} \delta\phi d\alpha_1 d\alpha_2 d\alpha_3
\end{aligned} \tag{2.38}$$

Proceeding with all terms in Eq. (2.37) yields:

$$\begin{aligned}
& \int_{t_0}^{t_1} dt \int_v \frac{\partial H}{\partial E_k} \delta E_k dv \\
& = \int_{t_0}^{t_1} dt \int_{\alpha_2} \int_{\alpha_3} (e_{15} S_{13} + \epsilon_{11} E_1) A_2 \left(1 + \frac{\alpha_3}{R_2}\right) \delta\phi d\alpha_2 d\alpha_3 \\
& + \int_{t_0}^{t_1} dt \int_{\alpha_1} \int_{\alpha_3} (e_{15} S_{23} + \epsilon_{11} E_2) A_1 \left(1 + \frac{\alpha_3}{R_1}\right) \delta\phi d\alpha_1 d\alpha_3 \\
& + \int_{t_0}^{t_1} dt \int_{\alpha_1} \int_{\alpha_2} (e_{31} S_{11} + e_{31} S_{22} + e_{33} S_{33} + \epsilon_{33} E_3) A_1 A_2 \left(1 + \frac{\alpha_3}{R_1}\right) \left(1 + \frac{\alpha_3}{R_2}\right) \delta\phi d\alpha_1 d\alpha_2 \\
& - \int_{t_0}^{t_1} dt \int_{\alpha_1} \int_{\alpha_2} \int_{\alpha_3} \left\{ \frac{\partial \left[(e_{15} S_{13} + \epsilon_{11} E_1) A_2 \left(1 + \frac{\alpha_3}{R_2}\right) \right]}{\partial\alpha_1} \right. \\
& + \frac{\partial \left[(e_{15} S_{23} + \epsilon_{11} E_2) A_1 \left(1 + \frac{\alpha_3}{R_1}\right) \right]}{\partial\alpha_2} \\
& + \left. \frac{\partial \left[(e_{31} S_{11} + e_{31} S_{22} + e_{33} S_{33} + \epsilon_{33} E_3) A_1 A_2 \left(1 + \frac{\alpha_3}{R_1}\right) \left(1 + \frac{\alpha_3}{R_2}\right) \right]}{\partial\alpha_3} \right\} \delta\phi d\alpha_1 d\alpha_2 d\alpha_3
\end{aligned} \tag{2.39}$$

With variation of electrical potential energy in the variational equation gives:

$$\begin{aligned}
& \int_{t_0}^{t_1} dt \int_S Q \delta \phi dS \\
&= \int_{t_0}^{t_1} dt \int_{\alpha_2} \int_{\alpha_3} Q_1 A_2 \left(1 + \frac{\alpha_3}{R_2} \right) \delta \phi d\alpha_2 d\alpha_3 \\
&+ \int_{t_0}^{t_1} dt \int_{\alpha_1} \int_{\alpha_3} Q_2 A_1 \left(1 + \frac{\alpha_3}{R_1} \right) \delta \phi d\alpha_1 d\alpha_3 \\
&+ \int_{t_0}^{t_1} dt \int_{\alpha_1} \int_{\alpha_2} Q_3 A_1 A_2 \left(1 + \frac{\alpha_3}{R_1} \right) \left(1 + \frac{\alpha_3}{R_2} \right) \delta \phi d\alpha_1 d\alpha_2
\end{aligned} \tag{2.40}$$

Thus, carrying out the electrical components of variations. Then derivations of system equations of the piezoelectric shell continuum can proceed. To obtain the charge equation, Eq. (2.41), simply take the fourth term of Eq. (2.39) inside the integral giving,

$$\begin{aligned}
& \partial \left[\frac{(e_{15} S_{13} + \epsilon_{11} E_1) A_2 \left(1 + \frac{\alpha_3}{R_2} \right)}{\partial \alpha_1} \right] + \partial \left[\frac{(e_{15} S_{23} + \epsilon_{11} E_2) A_1 \left(1 + \frac{\alpha_3}{R_1} \right)}{\partial \alpha_2} \right] \\
&+ \partial \left[\frac{(e_{31} S_{11} + e_{31} S_{22} + e_{33} S_{33} + \epsilon_{33} E_3) A_1 A_2 \left(1 + \frac{\alpha_3}{R_1} \right) \left(1 + \frac{\alpha_3}{R_2} \right)}{\partial \alpha_3} \right] = 0
\end{aligned} \tag{2.41}$$

The last three terms of the electromechanical equations are yield by substituting all energy variation terms into Hamilton's equation (but only observing the electric boundary conditions).

$$\begin{aligned}
& \int_{t_0}^{t_1} dt \int_{S_1} (e_{15} S_{13} + \epsilon_{11} E_1 + Q_1) A_2 \left(1 + \frac{\alpha_3}{R_2} \right) \delta \phi d\alpha_2 d\alpha_3 \\
&+ \int_{t_0}^{t_1} dt \int_{S_2} (e_{15} S_{23} + \epsilon_{11} E_2 + Q_2) A_1 \left(1 + \frac{\alpha_3}{R_1} \right) \delta \phi d\alpha_1 d\alpha_3 \\
&+ \int_{t_0}^{t_1} dt \int_{S_3} (e_{31} S_{11} + e_{31} S_{22} + e_{33} S_{33} + \epsilon_{33} E_3 + Q_3) A_1 A_2 \left(1 + \frac{\alpha_3}{R_1} \right) \left(1 + \frac{\alpha_3}{R_2} \right) \delta \phi d\alpha_1 d\alpha_2 = 0
\end{aligned} \tag{2.42}$$

The electric field value is defined along the material interface as the electric boundary conditions are defined on the outside surfaces of the piezoelectric shell.

$$(e_{15}S_{13} + \epsilon_{11} E_1 + Q_1) A_2 \left(1 + \frac{\alpha_3}{R_2}\right) = 0 \quad (2.43a)$$

$$(e_{15}S_{23} + \epsilon_{11} E_2 + Q_2) A_1 \left(1 + \frac{\alpha_3}{R_1}\right) = 0 \quad (2.43b)$$

$$(e_{31}S_{11} + e_{31}S_{22} + e_{33}S_{33} + \epsilon_{33} E_3 + Q_3) A_1 A_2 \left(1 + \frac{\alpha_3}{R_1}\right) \left(1 + \frac{\alpha_3}{R_2}\right) = 0 \quad (2.43c)$$

It can be seen that the electric displacements D on the surfaces are equal to the densities of surface charges σ , from Eqs. (2.43-a, b, c), which is defined as the amount of electric charge q that is present on a surface of given area A .

All $A_i \left(1 + \frac{\alpha_3}{R_i}\right)$ and $A_1 A_2 \left(1 + \frac{\alpha_3}{R_1}\right) \left(1 + \frac{\alpha_3}{R_2}\right)$ terms can be eliminated since $A_i \left(1 + \frac{\alpha_3}{R_i}\right) \neq 0$

and $A_1 A_2 \left(1 + \frac{\alpha_3}{R_1}\right) \left(1 + \frac{\alpha_3}{R_2}\right) \neq 0$, because A_i cannot be zero, and α_3 nor R_i can be a negative

number. Thus,

$$(e_{15}S_{13} + \epsilon_{11} E_1 + Q_1) = 0 \quad (2.44a)$$

$$(e_{15}S_{23} + \epsilon_{11} E_2 + Q_2) = 0 \quad (2.44b)$$

$$(e_{31}S_{11} + e_{31}S_{22} + e_{33}S_{33} + \epsilon_{33} E_3 + Q_3) = 0 \quad (2.44c)$$

The transverse shear deformations and rotary inertias are neglected as the piezoelectric shell continuum is thin. The transverse shear strains are considered negligible, i.e., $S_{13} = 0$ and $S_{23} = 0$. In-plane electric fields E_1 and E_2 are neglected too, with only

the transverse electric field E_3 discernible; Eq. (2.41), the charge equation of electrostatics, can be written as [15]:

$$\frac{\partial}{\partial \alpha_3} (e_{31}S_{11} + e_{32}S_{22} + \epsilon_{33} E_3) A_1 A_2 \left(1 + \frac{\alpha_3}{R_1}\right) \left(1 + \frac{\alpha_3}{R_2}\right) = 0 \quad (2.45)$$

The curvature effect can be neglected since $\alpha_3 \ll R_i$:

$$\left(1 + \frac{\alpha_3}{R_i}\right) \cong 1 \quad (2.46)$$

In sensor applications and open-circuit condition it is assumed there are no externally applied electric boundary conditions:

$$e_{31}S_{11} + e_{32}S_{22} + \epsilon_{33} E_3 = 0 \quad (2.47)$$

Integrating over the piezoelectric layer thickness:

$$\int_{\alpha_3} (e_{31}S_{11} + e_{32}S_{22}) d\alpha_3 + \epsilon_{33} \int_{\alpha_3} E_3 d\alpha_3 = 0 \quad (2.48)$$

The electric potential after integrating the electric field E_3 , is given by:

$$\int_{\alpha_3} E_3 d\alpha_3 = \phi_3 \quad (2.49)$$

$$\phi_3 = -\frac{1}{\epsilon_{33}} \int_{\alpha_3} (e_{31}S_{11} + e_{32}S_{22}) d\alpha_3 \quad (2.50)$$

The total signal output ϕ_3^S , for spatially distributed piezoelectric shell sensor continuum with an effective surface electrode area S^e is given as:

$$\begin{aligned} & \int_{S^e} \phi_3^S A_1 A_2 \left(1 + \frac{\alpha_3}{R_1}\right) \left(1 + \frac{\alpha_3}{R_2}\right) d\alpha_1 d\alpha_2 \\ &= -\frac{1}{\epsilon_{33}} \int_{S^e} \int_{\alpha_3} (e_{31}S_{11} + e_{32}S_{22}) A_1 A_2 \left(1 + \frac{\alpha_3}{R_1}\right) \left(1 + \frac{\alpha_3}{R_2}\right) d\alpha_1 d\alpha_2 d\alpha_3 \end{aligned} \quad (2.51)$$

Note: $\frac{\alpha_3}{R_1} \ll 1$, $\frac{\alpha_3}{R_2} \ll 1$

Neglecting curvature effect and taking the surface average over the entire electrode area

S^e gives:

$$\phi_3^S = - \frac{\int_{S^e} \int_{\alpha_3} (e_{31} S_{11} + e_{32} S_{22}) A_1 A_2 d\alpha_1 d\alpha_2 d\alpha_3}{\epsilon_{33} S^e} \quad (2.52)$$

Note that $\int_{S^e} A_1 A_2 \left(1 + \frac{\alpha_3}{R}\right) \left(1 + \frac{\alpha_3}{R}\right) d\alpha_1 d\alpha_2 = S^e$.i.e. effective electrode area. In case of a

thin shell continuum, normal strains can be further divided into two strain components:

membrane strains, S_{ii}° and bending strains, κ_{ii} :

$$S_{11} = S_{11}^\circ + \alpha_3 \kappa_{11} \quad (2.53)$$

$$S_{22} = S_{22}^\circ + \alpha_3 \kappa_{22} \quad (2.54)$$

Throughout the thickness of a shell, plate, or beam the membrane strain is defined as average strain and occurs during in-plane expansion and contraction. During bending applications, bending strain occurs and is calculated by determining the relationship between the force and the amount of bending which results from it. In case of distributed sensors made of symmetrical hexagonal piezoelectric materials, the piezoelectric constants $e_{31} = e_{32}$. Thus, the sensor output signal is given by:

$$\phi_3^S = - \frac{1}{\epsilon_{33} S^e} \int_{S^e} \int_{\alpha_3}^{h^S} \left[e_{31} (S_{11}^\circ + S_{22}^\circ) + \alpha_3 (\kappa_{11} + \kappa_{22}) \right] A_1 A_2 d\alpha_1 d\alpha_2 d\alpha_3 \quad (2.55)$$

The membrane strains and bending strains represented by S_{ii}° and κ_{ii} , respectively, can be further expressed as a function of three neutral-surface displacements, u_1 , u_2 , and u_3 , in the three axial directions:

$$S_{11}^{\circ} = \frac{1}{A_1} \frac{\partial u_1}{\partial \alpha_1} + \frac{u_2}{A_1 A_2} \frac{\partial A_1}{\partial \alpha_2} + \frac{u_3}{R_1}$$

(2.56)

$$S_{22}^{\circ} = \frac{1}{A_2} \frac{\partial u_2}{\partial \alpha_2} + \frac{u_1}{A_1 A_2} \frac{\partial A_2}{\partial \alpha_1} + \frac{u_3}{R_2} \quad (2.57)$$

$$\kappa_{11} = \frac{1}{A_1} \frac{\partial}{\partial \alpha_1} \left(\frac{u_1}{R_1} - \frac{1}{A_1} \frac{\partial u_3}{\partial \alpha_1} \right) + \frac{1}{A_1 A_2} \left(\frac{u_2}{R_2} - \frac{1}{A_2} \frac{\partial u_3}{\partial \alpha_2} \right) \frac{\partial A_1}{\partial \alpha_2} \quad (2.58)$$

$$\kappa_{22} = \frac{1}{A_2} \frac{\partial}{\partial \alpha_2} \left(\frac{u_2}{R_2} - \frac{1}{A_2} \frac{\partial u_3}{\partial \alpha_2} \right) + \frac{1}{A_1 A_2} \left(\frac{u_1}{R_1} - \frac{1}{A_1} \frac{\partial u_3}{\partial \alpha_1} \right) \frac{\partial A_2}{\partial \alpha_1} \quad (2.59)$$

Substituting Eq. (2.56), (2.57), (2.58), and (2.59) into Eq. (2.55) gives the general sensor equation:

$$\begin{aligned} \phi_3^S = & -\frac{1}{\epsilon_{33} S^e} \int_{S^e} \int_{\alpha_3}^{h^s} \left\{ e_{31} \left[\frac{1}{A_1} \frac{\partial u_1}{\partial \alpha_1} + \frac{u_2}{A_1 A_2} \frac{\partial A_1}{\partial \alpha_2} + \frac{u_3}{R_1} \right. \right. \\ & \left. \left. + \alpha_3 \left(\frac{1}{A_1} \frac{\partial}{\partial \alpha_1} \left(\frac{u_1}{R_1} - \frac{1}{A_1} \frac{\partial u_3}{\partial \alpha_1} \right) + \frac{1}{A_1 A_2} \left(\frac{u_2}{R_2} - \frac{1}{A_2} \frac{\partial u_3}{\partial \alpha_2} \right) \frac{\partial A_1}{\partial \alpha_2} \right) \right] \right. \\ & \left. + e_{32} \left[\frac{1}{A_2} \frac{\partial u_2}{\partial \alpha_2} + \frac{u_1}{A_1 A_2} \frac{\partial A_2}{\partial \alpha_1} + \frac{u_3}{R_2} \right. \right. \\ & \left. \left. + \alpha_3 \left(\frac{1}{A_2} \frac{\partial}{\partial \alpha_2} \left(\frac{u_2}{R_2} - \frac{1}{A_2} \frac{\partial u_3}{\partial \alpha_2} \right) + \frac{1}{A_1 A_2} \left(\frac{u_1}{R_1} - \frac{1}{A_1} \frac{\partial u_3}{\partial \alpha_1} \right) \frac{\partial A_2}{\partial \alpha_1} \right) \right] \right\} A_1 A_2 d\alpha_1 d\alpha_2 d\alpha_3 \end{aligned} \quad (2.60)$$

Note the Lamé parameters, the A_i s, and radii of curvatures, the R_i s, are geometry dependent, e.g., for a rectangular plate $A_1 = A_2 = 1$ and $R_1 = R_2 = \infty$; for a cylindrical shell $A_1 = 1$, $A_2 = R$, $R_1 = \infty$, and $R_2 = R$. Thus, further simplification of the sensor equation is based on these four parameters defined for the geometries. Certain shaping functions can be used to specify the sensor shape and is introduced in next section.

2.2 Distributed Sensing of Elastic Shells

Excess observations in a control system can give unwanted dynamic responses. Thus, it is necessary that sensors only monitor those modes which need to be controlled, so that spillover is prevented. However, sensors respond to the controlled as well as the modes uncontrolled residual modes. Their occurrence can be reduced by implementing certain techniques like; one such method is to use spatially distributed modal sensors which only respond to a structural mode or group of modes. The detailed electromechanics of generic distributed shell sensors/actuators for modal sensing and control are studied under next section.

2.2.1 Generic Shape

A piezoelectric film is bonded to a flexible shell continuum and covers the entire surface of the structure in the generic case. The piezoelectric film is perfectly coupled with the shell continuum but does not affect its dynamic characteristics, such as natural frequencies and mode shapes. The top piezoelectric layer on the generic shell distributed sensor/actuator system acts as a distributed sensor. A distributed sensing theory based on the direct piezoelectric effect and the shell strains/deformations is presented in this section. It is assumed that the distributed piezoelectric layer is very thin in comparison to the shell structure. Therefore, the piezoelectric strains are the same as the outer surface strains of the shell continuum. The transverse electric field E_3 is considered for such thin film, and thus the voltage across the electrodes can be obtained by integrating the electric field over the thickness of the piezoelectric sensor layer as shown in Eq. (2.61).

$$\phi = -\int^{h^s} E_3 d\alpha_3 \quad (2.61)$$

where piezoelectric sensor thickness is defined by h^s . Using Figure 2.1, Eq. (2.61) can be expressed in terms of normal strains for the sensor: S_{11}^s and S_{22}^s in the direction of α_1 and α_2 , respectively, and dielectric displacement D_3 .

$$\phi_3 = h^s (h_{31}S_{11}^s + h_{32}S_{22}^s - \beta_{33}D_3) \quad (2.62)$$

where β_{33} and h_{ij} denote the impermeability and the strain charge coefficients of the piezoelectric sensor, respectively. It is assumed that the piezoelectric material is insensitive to in-plane twisting shear strain S_{12} . The shell being thin, the transverse shear strains S_{13} and S_{23} are neglected. The piezoelectric sensor layer when coupled with the elastic shell; the normal strains in the sensor layer can be estimated by:

$$S_{11}^s = \left\{ \left[\frac{1}{A_1} \frac{\partial u_1}{\partial \alpha_1} + \frac{u_2}{A_1 A_2} \frac{\partial A_1}{\partial \alpha_2} + \frac{u_3}{R_1} \right] + r_1^s \left[\frac{1}{A_1} \frac{\partial}{\partial \alpha_1} \left(\frac{u_1}{R_1} - \frac{1}{A_1} \frac{\partial u_3}{\partial \alpha_1} \right) + \frac{1}{A_1 A_2} \frac{\partial A_1}{\partial \alpha_2} \left(\frac{u_2}{R_2} - \frac{1}{A_2} \frac{\partial u_3}{\partial \alpha_2} \right) \right] \right\} \quad (2.63)$$

$$S_{22}^s = \left\{ \left[\frac{1}{A_2} \frac{\partial u_2}{\partial \alpha_2} + \frac{u_1}{A_1 A_2} \frac{\partial A_2}{\partial \alpha_1} + \frac{u_3}{R_2} \right] + r_2^s \left[\frac{1}{A_2} \frac{\partial}{\partial \alpha_2} \left(\frac{u_2}{R_2} - \frac{1}{A_2} \frac{\partial u_3}{\partial \alpha_2} \right) + \frac{1}{A_1 A_2} \frac{\partial A_2}{\partial \alpha_1} \left(\frac{u_1}{R_1} - \frac{1}{A_1} \frac{\partial u_3}{\partial \alpha_1} \right) \right] \right\} \quad (2.64)$$

where r_1^s and r_2^s refer to the distances measured from the neutral surface to the mid-plane of the sensor layer. Rearranging Eq. (2.62), the electric displacement D_3^s can be written as:

$$D_3^s = \frac{1}{\beta_{33}} \left(h_{31}S_{11}^s + h_{32}S_{22}^s - \frac{\phi_3}{h^s} \right) \quad (2.65)$$

Since D_3^S is defined as the charge per unit area, Eq. (2.64) can be integrated over the electrode surface S^e to estimate a total surface charge. By setting the charge zero, an open-circuit voltage ϕ^S condition can be obtained:

$$\begin{aligned}\phi^S &= \frac{h^S}{S^e} \int_{S^e} (h_{31}S_{11}^S + h_{32}S_{22}^S) dS^e \\ &= \frac{h^S}{S^e} \int_{S^e} (h_{31}S_{11}^S + h_{32}S_{22}^S) A_1 A_2 d\alpha_1 d\alpha_2\end{aligned}\quad (2.66)$$

Substituting the strains into Eq. (2.65) yields the distributed sensor output $\phi^S(\alpha_1, \alpha_2)$ in terms of displacements and other system parameters.

$$\begin{aligned}\phi^S(\alpha_1, \alpha_2) &= \frac{h^S}{S^e} \int_{S^e} \left\{ \left(\frac{1}{A_1} \frac{\partial u_1}{\partial \alpha_1} + \frac{u_2}{A_1 A_2} \frac{\partial A_1}{\partial \alpha_2} + \frac{u_3}{R_1} \right) \right. \\ &+ r_1^S \left[\frac{1}{A_1} \frac{\partial}{\partial \alpha_1} \left(\frac{u_1}{R_1} - \frac{1}{A_1} \frac{\partial u_3}{\partial \alpha_1} \right) + \frac{1}{A_1 A_2} \frac{\partial A_1}{\partial \alpha_2} \left(\frac{u_2}{R_2} - \frac{1}{A_2} \frac{\partial u_3}{\partial \alpha_2} \right) \right] \left. \right\} \\ &+ h_{32} \left\{ \left(\frac{1}{A_2} \frac{\partial u_2}{\partial \alpha_2} + \frac{u_1}{A_1 A_2} \frac{\partial A_2}{\partial \alpha_1} + \frac{u_3}{R_2} \right) + r_2^S \left[\frac{1}{A_2} \frac{\partial}{\partial \alpha_2} \left(\frac{u_2}{R_2} - \frac{1}{A_2} \frac{\partial u_3}{\partial \alpha_2} \right) \right. \right. \\ &\left. \left. + \frac{1}{A_1 A_2} \frac{\partial A_2}{\partial \alpha_1} \left(\frac{u_1}{R_1} - \frac{1}{A_1} \frac{\partial u_3}{\partial \alpha_1} \right) \right] \right\} dS^e\end{aligned}\quad (2.67)$$

Eq. (2.67) relates the piezoelectric film output charge to the dynamic of the substrate shell structure and from this equation, many sensors and actuators have been developed using experimental, simplified analytical, and finite element approaches. The sensor design goal is the development of a technique that uses a combination of numerical and experimental methods for sensors or actuators design.

2.2.2 Spatial Thickness Shaping

Distributed piezoelectric shell layers can be both surface bonded or embedded with a flexible elastic shell and the layers are used as distributed sensors. In case of a spatially

distributed piezoelectric shell convolving sensor, a weighting function $W(\alpha_1, \alpha_2)$ and a polarity function $\text{sgn}[U_3(\alpha_1, \alpha_2)]$ can be added to the generic shell sensor equation, Eq. (2.67). Also, a $\text{sgn}(\cdot)$ denotes a signum function can be used to change the piezoelectric polarity, in which $\text{sgn}(\cdot)=1$ when $(\cdot)>0$, 0 when $(\cdot)=0$ and -1 when $(\cdot)<0$. $U_3(\alpha_1, \alpha_2)$ denotes a transverse modal function, mode shape function. Weighting functions discussed are: thickness shaping and surface shaping. It is assumed that the thickness of the piezoelectric shell is a spatial function for thickness shaping.

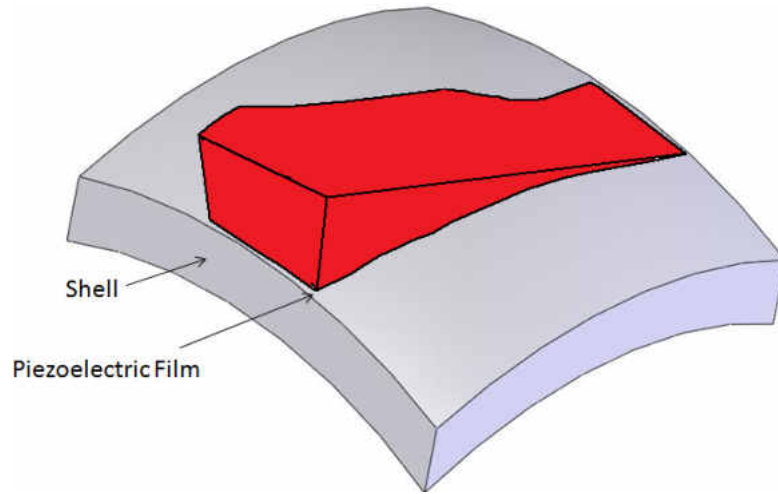


Figure 2.2: Spatial Thickness Shaping

The sensor thickness varies over the effective sensor area for spatial thickness shaping. Thickness shaping of distributed shell sensors is illustrated in the Figure 2.2. The piezoelectric shell sensor thickness is a spatial function $W_t(\alpha_1, \alpha_2)$. Thus, the sensor equation, Eq. (2.51), becomes:

$$\begin{aligned}
& \int_{S^e} \phi_3^S A_1 A_2 \left(1 + \frac{\alpha_3}{R_1}\right) \left(1 + \frac{\alpha_3}{R_2}\right) d\alpha_1 d\alpha_2 \\
&= -\frac{e_{31}}{\epsilon_{33}} \int_{\alpha_1} \int_{\alpha_2} \operatorname{sgn}[U_3(\alpha_1, \alpha_2)] \left[W_t(\alpha_1, \alpha_2) (S_{11}^\circ + S_{22}^\circ) \right. \\
& \left. + \int_{r_1}^{W_t(\alpha_1, \alpha_2) + r_1} \alpha_3 (\kappa_{11} + \kappa_{22}) d\alpha_3 \right] \left(1 + \frac{\alpha_3}{R_1}\right) \left(1 + \frac{\alpha_3}{R_2}\right) A_1 A_2 d\alpha_1 d\alpha_2
\end{aligned} \tag{2.68}$$

effective sensor area or electrode area denoted by S^e and r_1 is the distance measured from the shell neutral surface to the bottom of the piezoelectric sensor layer. The first term inside the second set of square brackets is contributed by the membrane strains and the second by the bending strains. The total output signal of the sensor is contributed by the sum of membrane and bending strains.

2.2.3 Spatial Surface Shaping

The piezoelectric shell thickness is assumed constant in the second case. The substrate flexible shell structure surface is not usually covered by piezoelectric film entirely. The film is in fact shaped such that the output charge represents the desired dynamic characteristics of the structure. Surface shaping of a shell sensor is illustrated in Figure 2.3. Weighting shape function $W_s(\alpha_1, \alpha_2)$ can be used in designing sensor shape.

$$\begin{aligned}
& \int_{\alpha_1} \int_{\alpha_2} \phi_3^S \left(1 + \frac{\alpha_3}{R_1}\right) \left(1 + \frac{\alpha_3}{R_2}\right) A_1 A_2 d\alpha_1 d\alpha_2 \\
&= -\frac{1}{\epsilon_{33}} \int_{\alpha_1} \int_{\alpha_2} W_s(\alpha_1, \alpha_2) \cdot \operatorname{sgn}[U_3(\alpha_1, \alpha_2)] \int_{S^e} (e_{31} S_{11} + e_{31} S_{22}) \\
& \cdot \left(1 + \frac{\alpha_3}{R_1}\right) \left(1 + \frac{\alpha_3}{R_2}\right) A_1 A_2 d\alpha_1 d\alpha_2 d\alpha_3
\end{aligned} \tag{2.69}$$

The film covers the whole structure as the generic sensor equation does not include a shape function. The film covers a certain area of the structure as for the shaped sensor equation, it does have a shape function.

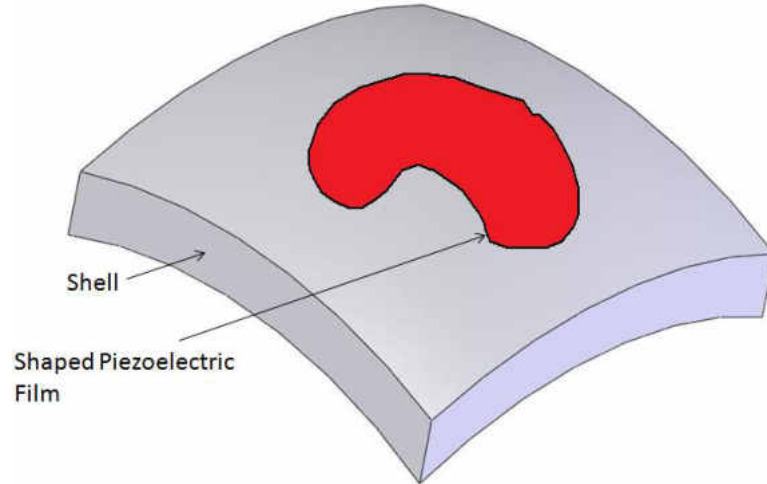


Figure 2.3: Spatial Surface Shaping

Considering Eq. (2.67) as the output of the piezoelectric film analytical calculations for simple structures such as beams, plates, and cylinders can be done if u_1 , u_2 , u_3 are known. However, for complicated structures and boundary conditions, an analytical solution is impossible, but with help of numerical integration, the charge ϕ could be calculated. Here, it is assumed that the structure displacement field can be obtained either experimentally or with finite element analysis. Before the numerical integration, the spatial double derivatives are computed. Further, the generic sensor shaping theory is applied to a cylindrical shell, plate, and beam.

2.3 Cylindrical Shell

The generic sensor theory is also applicable to other geometries with curvature, such as a cylinder, sphere, ring, cylindrical shell, etc. a cylindrical shell is discussed here. A cylindrical shell is defined by a three tri-orthogonal axes α_1 , α_2 , and α_3 . In terms of cylindrical coordinate system the cylindrical shell can be defined as; the z-axis (α_1) is aligned with the length, the second axis θ (α_2) defines the circumferential direction and the

third axis (α_3) is normal to the neutral surface. In case of a generic sensor, the sensor would cover the entire outer surface of the shell; Figure 2.4 illustrates the cylindrical shell with a piezoelectric shaped sensor attached to the top half of the structure.

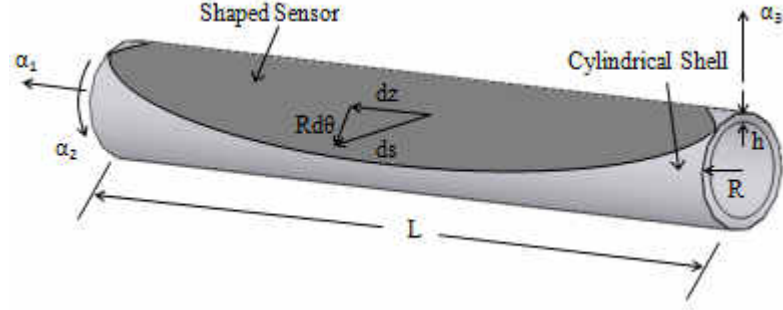


Figure 2.4: Cylindrical Shell with a Shaped Sensor Adhered

It has Lamé parameters: $A_1 = 1$ and $A_2 = R$, and radii of curvatures: $R_1 = \infty$ and $R_2 = R$. Substituting these four parameters into the generic shell sensor equation Eq. (2.67) gives:

$$\begin{aligned}
 \phi^s(\alpha_1, \alpha_2) = & \frac{h^s}{S^e} \int_{S^e} \left\{ h_{31} \left[\left(\frac{1}{(1)} \frac{\partial u_1}{\partial \alpha_1} + \frac{u_2}{(1)(R)} \frac{\partial(1)}{\partial \alpha_2} + \frac{u_3}{(\infty)} \right) \right. \right. \\
 & + r_1^s \left[\frac{1}{(1)} \frac{\partial}{\partial \alpha_1} \left(\frac{u_1}{(\infty)} - \frac{1}{(1)} \frac{\partial u_3}{\partial \alpha_1} \right) + \frac{1}{(1)(R)} \frac{\partial(1)}{\partial \alpha_2} \left(\frac{u_2}{(R)} - \frac{1}{(R)} \frac{\partial u_3}{\partial \alpha_2} \right) \right] \left. \right\} \\
 & + h_{32} \left\{ \left[\frac{1}{(R)} \frac{\partial u_2}{\partial \alpha_2} + \frac{u_1}{(1)(R)} \frac{\partial(R)}{\partial \alpha_1} + \frac{u_3}{(R)} \right] + r_2^s \left[\frac{1}{(R)} \frac{\partial}{\partial \alpha_2} \left(\frac{u_2}{(R)} - \frac{1}{(R)} \frac{\partial u_3}{\partial \alpha_2} \right) \right. \right. \\
 & \left. \left. + \frac{1}{(1)(R)} \frac{\partial(R)}{\partial \alpha_1} \left(\frac{u_1}{(\infty)} - \frac{1}{(1)} \frac{\partial u_3}{\partial \alpha_1} \right) \right] \right\} dS^e
 \end{aligned} \tag{2.70}$$

Simplifying Eq. (2.70), where $\frac{\partial(1)}{\partial \alpha_2} = 1, \frac{u_{1,3}}{(\infty)} = 0$ gives:

$$\begin{aligned}
\phi^s(\alpha_1, \alpha_2) &= \frac{h^s}{S^e} \int_{S^e} \left(h_{31} \left\{ \left(\frac{\partial u_1}{\partial \alpha_1} + \frac{u_2}{R} \right) \right. \right. \\
&+ r_1^s \left[\frac{\partial}{\partial \alpha_1} \left(-\frac{\partial u_3}{\partial \alpha_1} \right) + \frac{1}{R} \left(\frac{u_2}{R} - \frac{1}{R} \frac{\partial u_3}{\partial \alpha_2} \right) \right] \left. \right\} \\
&+ h_{32} \left\{ \left(\frac{1}{R} \frac{\partial u_2}{\partial \alpha_2} + \frac{u_1}{R} \frac{\partial R}{\partial \alpha_1} + \frac{u_3}{R} \right) + r_2^s \left[\frac{1}{R} \frac{\partial}{\partial \alpha_2} \left(\frac{u_2}{R} - \frac{1}{R} \frac{\partial u_3}{\partial \alpha_2} \right) \right. \right. \\
&\left. \left. + \frac{1}{R} \frac{\partial R}{\partial \alpha_1} \left(-\frac{\partial u_3}{\partial \alpha_1} \right) \right] \right\} \right) dS^e
\end{aligned} \tag{2.71}$$

Conversion from curvilinear to cylindrical coordinates gives:

$$\begin{aligned}
\phi^s(z, \theta) &= \frac{-h^s}{S^e} \int_{S^e} \left(h_{31} \left\{ \left(\frac{\partial u_z}{\partial z} + \frac{u_\theta}{R} \right) \right. \right. \\
&+ r_z^s \left[\frac{\partial}{\partial z} \left(-\frac{\partial u_R}{\partial z} \right) + \frac{1}{R} \left(\frac{u_\theta}{R} - \frac{1}{R} \frac{\partial u_R}{\partial \theta} \right) \right] \left. \right\} \\
&+ h_{32} \left\{ \left(\frac{1}{R} \frac{\partial u_\theta}{\partial \theta} + \frac{u_z}{R} \frac{\partial R}{\partial z} + \frac{\partial u_R}{\partial z} \right) + r_\theta^s \left[\frac{1}{R} \frac{\partial}{\partial \theta} \left(\frac{u_\theta}{R} - \frac{1}{R} \frac{\partial u_R}{\partial \theta} \right) \right. \right. \\
&\left. \left. + \frac{1}{R} \frac{\partial R}{\partial z} \left(-\frac{\partial u_R}{\partial z} \right) \right] \right\} \right) dS^e
\end{aligned} \tag{2.72}$$

Where $\frac{u_\theta}{R} = 0, \frac{\partial u_R}{\partial z} = 0$ and multiplying through gives:

$$\begin{aligned}
\phi^s(z, \theta) &= \frac{-h^s}{S^e} \int_{S^e} \left(h_{31} \left\{ \left(\frac{\partial u_z}{\partial z} \right) + r_z^s \left(-\frac{\partial}{\partial z} \frac{\partial u_R}{\partial z} \right) + \left(-\frac{1}{R^2} \frac{\partial u_R}{\partial \theta} \right) \right\} \right. \\
&+ h_{32} \left\{ \left(\frac{1}{R} \frac{\partial u_\theta}{\partial \theta} + \frac{u_z}{R} \frac{\partial R}{\partial z} + \frac{\partial u_R}{\partial z} \right) + r_\theta^s \left(\frac{1}{R} \frac{\partial}{\partial \theta} \frac{u_\theta}{R} - \frac{1}{R^2} \frac{\partial}{\partial \theta} \frac{\partial u_R}{\partial \theta} \right) \right\} \left. \right) dS^e
\end{aligned} \tag{2.73}$$

$$\begin{aligned}
\phi^s(z, \theta) &= \frac{-e_{31} h^s}{e_{33} S^e} \int_{S^e} \left\{ e_{31} \left(\frac{\partial u_z}{\partial z} - r_z^s \frac{\partial^2 u_R}{\partial z^2} \right) \right. \\
&+ e_{32} \left(\frac{\partial u_\theta}{R \partial \theta} + \frac{u_R}{R^2} + r_\theta^s \frac{\partial u_\theta}{R^2 \partial \theta} - r_\theta^s \frac{\partial^2 u_R}{R^2 \partial \theta^2} \right) \left. \right\} dS^e
\end{aligned}$$

(2.74)

Thus, can be expanded to:

$$\begin{aligned} \phi^s(z, \theta) = & \frac{-e_{31}h^s}{e_{33}S^e} \int_0^z \int_{\theta=0}^{\theta=\pi} \int_{r-t}^r \left\{ e_{31}(z'(z) - r_z^s z''(R)) \right. \\ & \left. + e_{32} \left(\frac{1}{R} \theta'(\theta) + \frac{u_R}{R^2} + r_\theta^s \frac{1}{R^2} \theta'(\theta) - r_\theta^s \frac{1}{R^2} \theta''(R) \right) \right\} r dr d\theta dz \end{aligned} \quad (2.75)$$

It is observed that the transverse direction, exhibits greater displacement than that of the other two directions when the cylindrical shell is under loading. Thereby, it is proposed that the shape of the cylindrical shell can be observed as the shape of a plate to visualize the shape of the sensor. Hence, $F = k(x^2 - Lx)$ for a beam by Lee and Moon [34], is also used for the shaping function of the piezoelectric sensor for a cylindrical shell, because shaping function can correctly capture the dynamic of the structure; verified by the previous research on the shaped film [34].

2.4 Plate Substrate

A plate is a zero-curvature shell case. The general sensor equation is applicable here as well. The development of the generic sensor output charge equation for a plate is presented in this section. The Lamé parameters are derived from the fundamental equation $(ds)^2 = (1)^2(dx)^2 + (1)^2(dy)^2$ and therefore $A_1 = A_2 = 1$ and $R_1 = R_2 = \infty$. Substituting these values into Eq. (2.67), the piezoelectric film output charge is given as:

$$\begin{aligned}
\phi^S(\alpha_1, \alpha_2) = & \frac{h^S}{S^e} \int_{S^e} \left(h_{31} \left\{ \left(\frac{1}{(1)} \frac{\partial u_1}{\partial \alpha_1} + \frac{u_2}{(1)(1)} \frac{\partial(1)}{\partial \alpha_2} + \frac{u_3}{(\infty)} \right) \right. \right. \\
& + r_1^S \left[\frac{1}{(1)} \frac{\partial}{\partial \alpha_1} \left(\frac{u_1}{(\infty)} - \frac{1}{(1)} \frac{\partial u_3}{\partial \alpha_1} \right) + \frac{1}{(1)(1)} \frac{\partial(1)}{\partial \alpha_2} \left(\frac{u_2}{(\infty)} - \frac{1}{(1)} \frac{\partial u_3}{\partial \alpha_2} \right) \right] \left. \right\} \\
& + h_{32} \left\{ \left(\frac{1}{(1)} \frac{\partial u_2}{\partial \alpha_2} + \frac{u_1}{(1)(1)} \frac{\partial(1)}{\partial \alpha_1} + \frac{u_3}{(\infty)} \right) + r_2^S \left[\frac{1}{(1)} \frac{\partial}{\partial \alpha_2} \left(\frac{u_2}{(\infty)} - \frac{1}{(1)} \frac{\partial u_3}{\partial \alpha_2} \right) \right. \right. \\
& \left. \left. + \frac{1}{(1)(1)} \frac{\partial(1)}{\partial \alpha_1} \left(\frac{u_1}{(\infty)} - \frac{1}{(1)} \frac{\partial u_3}{\partial \alpha_1} \right) \right] \right\} \left. \right) dS^e
\end{aligned} \tag{2.76}$$

Simplifying Eq. (2.76), where $\frac{u_{1,2,3}}{(\infty)} = 0$ gives:

$$\begin{aligned}
\phi^S(\alpha_1, \alpha_2) = & \frac{h^S}{S^e} \int_{S^e} \left(h_{31} \left\{ \left(\frac{\partial u_1}{\partial \alpha_1} + \frac{\partial u_2}{\partial \alpha_2} \right) + r_1^S \left[\frac{\partial}{\partial \alpha_1} \left(-\frac{\partial u_3}{\partial \alpha_1} \right) + \frac{\partial}{\partial \alpha_2} \left(-\frac{\partial u_3}{\partial \alpha_2} \right) \right] \right\} \right. \\
& \left. + h_{32} \left\{ \left(\frac{\partial u_2}{\partial \alpha_2} + \frac{\partial u_1}{\partial \alpha_1} \right) + r_2^S \left[\frac{\partial}{\partial \alpha_2} \left(-\frac{\partial u_3}{\partial \alpha_2} \right) + \frac{\partial}{\partial \alpha_1} \left(-\frac{\partial u_3}{\partial \alpha_1} \right) \right] \right\} \right) dS^e
\end{aligned} \tag{2.77}$$

The plate as defined in a coordinate system where the x-axis (α_1) is aligned with the length, the y-axis (α_2) defines the width and the third axis (α_3) is normal to the neutral surface. Eq. (2.77) on further simplification, where the plate, shown in Figure 2.6,

experiences only a transverse vibration, where $\frac{\partial u_1}{\partial \alpha_1} = \frac{\partial u_2}{\partial \alpha_2} = 0$.

$$\begin{aligned}
\phi^S(\alpha_1, \alpha_2) = & \frac{h^S}{S^e} \int_{S^e} \left(h_{31} \left\{ r_x^S \left[-\frac{\partial^2 u_3}{\partial x^2} - \frac{\partial^2 u_3}{\partial y^2} \right] \right\} + h_{32} \left\{ r_y^S \left[-\frac{\partial^2 u_3}{\partial y^2} - \frac{\partial^2 u_3}{\partial x^2} \right] \right\} \right) dS^e
\end{aligned} \tag{2.78}$$

The generic sensor output charge equation for a plate is given by:

$$\phi^S = -\frac{h^S}{S^e} \int_{S^e} \left[h_{31} r_x^S \frac{\partial^2 u_3}{\partial x^2} + h_{32} r_y^S \frac{\partial^2 u_3}{\partial y^2} \right] dS^e \quad (2.79)$$

According to the research done on known film shapes for a plate by Zahui and Wendt [35], they proposed the following equation:

$$\phi^S = \int_0^{L_y} \int_0^{L_x} (-h) W_s(x, y) \left[h_{31} \frac{\partial^2 u_3}{\partial x^2} + h_{32} \frac{\partial^2 u_3}{\partial y^2} \right] dx dy \quad (2.80)$$

Where L_x and L_y refer to the dimensions of the plate in the x and y directions, respectively. $W_s(x, y)$ is the surface shaping function of the plate where h is given by the following equation:

$$h = \frac{h_p + h_s}{2} \quad (2.81)$$

Where plate and sensor thicknesses are defined by h_p and h_s , respectively.

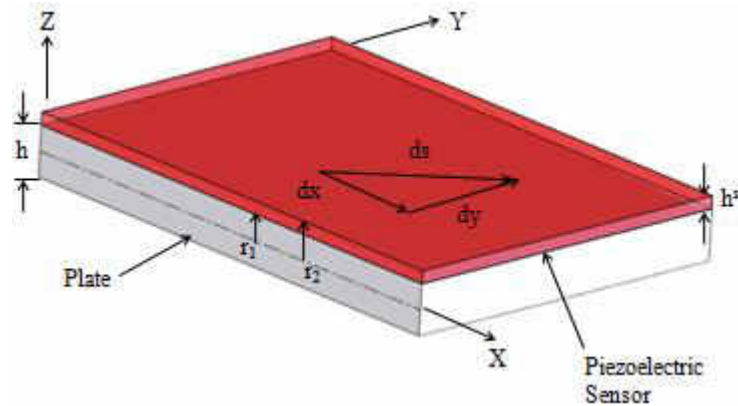


Figure 2.5: A Rectangular Plate Bonded with a Piezoelectric Sensor

The equation for the shape of a beam as proposed by Lee and Moon [34], can be applied to a plate to develop the shaped sensor for the plate.

2.5 Beam Substrate

The general sensor equation can be applied to a beam structure too. In this section, the generic sensor output charge equations for a beam are presented [31]. Note that the plate structure can be reduced to a beam structure by considering only one effective axis, in this case, the x -direction. Thus, the generic sensor output equation, Eq. (2.67) can be written as:

$$\phi^S = -\frac{bh^S}{S^e} \int_x \left(h_{31} r_x^S \frac{\partial^2 u_3}{\partial x^2} \right) dx \quad (2.82)$$

where b is the beam width.

CHAPTER III
SENSOR DEVELOPMENT

3.1 Sensor Design

3.1.1 Beam Displacement Sensor Design

3.1.1.1 Sensor Equation

When multiple patches of the beam are to be used with n segments of film, output charge for the i^{th} patch can be derived from Eq. (2.6):

$$\phi_i = -\frac{bh_i^f}{S_i^f} \int_{x_{i-1}}^{x_i} \left(h_{31_i} r_{x_i}^f \frac{\partial^2 z_i}{\partial x^2} \right) dx \quad (2.83)$$

On further simplifying Eq. (2.83), we get:

$$\phi_i = -\frac{bh_i^f}{S_i^f} h_{31_i} r_{x_i}^f \left[\frac{\partial z_i}{\partial x} \right]_{x_{i-1}}^{x_i} \quad (2.84)$$

Now considering the i^{th} patch and assuming the slope of the deflected beam to be constant at the patch. Variable a_i represents the slope, Eq. (2.84) can be written as;

$$\phi_i = -\frac{bh_i^f}{S_i^f} h_{31_i} r_{x_i}^f a_i \quad (2.85)$$

Sensor general equation is represented by Eq. (2.85).

The output signal obtained from the i^{th} patch is directly proportional to its slope.

Hence the slope of the patch considered can be represented in form of the charge ϕ_i

$$a_i = -\frac{\phi_i S_i^f}{bh_i^f h_{31}^f r_{x_i}^f} \quad (2.86)$$

Hence, the slope of the deflected beam can be calculated at the sensor patch from above equation.

3.1.1.2 Beam lateral displacement equation

In the figure 2.6, z represents the deflection of the beam and can be evaluated at points that lie left and right of the center point x of i^{th} patch. The central-difference formula is applied to determine the slope at the center of the patch.

$$a_i \cong \frac{z(x + \Delta x) - z(x - \Delta x)}{2\Delta x} \quad (2.87)$$

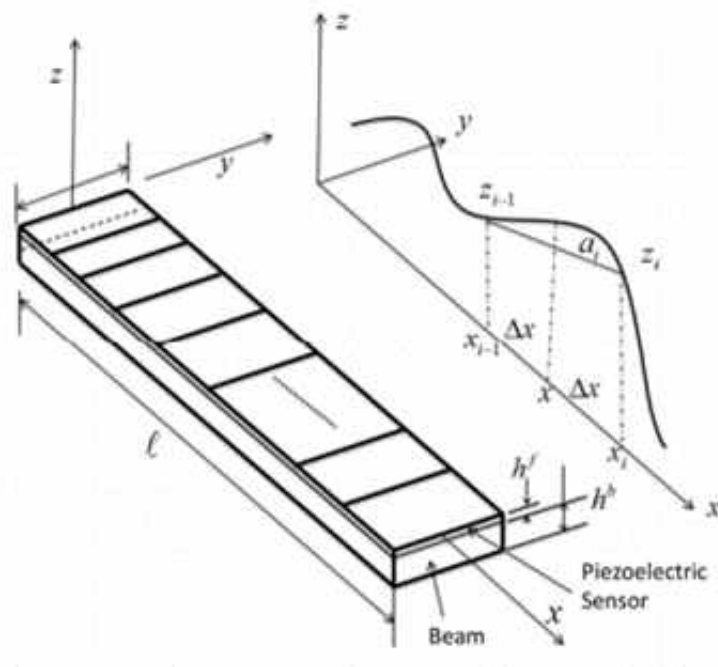


Figure 3.1: Beam with PVDF film and deflection curve.

Now substituting $z_i = z(x + \Delta x) = z(x_i)$, $z_{i-1} = z(x - \Delta x) = z(x_{i-1})$ and $2\Delta x = x_i - x_{i-1}$, hence Eq. (2.87) can be written as:

$$z_i \cong a_i(x_i - x_{i-1}) + z_{i-1} \quad (2.88)$$

The value of slope obtained from Eq. (2.86) is substituted in Eq. (2.88) to obtain Eq. (2.89). Here we assume the piezoelectric film patches to be of equal length and fabricated from the same material of uniform thickness.

$$x_i - x_{i-1} = \frac{\ell}{n}, \quad r_{x_i}^f = \frac{h^f + h^b}{2} \cong \frac{h_b}{2}, \quad h_{31_i} = h_{31} \quad (2.89)$$

The beam lateral displacement equation:

$$z_i = -2 \frac{\phi_i \ell^2}{h^f h_b h_{31} n^2} + z_{i-1} \quad (2.90)$$

The above equation requires displacement of beam from one end. For clamped, cantilever and simply supported boundary conditions the ends those are stationary will have zero displacements, whereas a point sensor can be used to determine the displacement at other points.

3.1.2 Plate Displacement Sensor Equation

For the plate vibration displacement sensor, plate substrate and Eq. (2.79) is considered. If multiple patches of the film are used as shown in Fig. (2.6) with $n \times m$ patches of films, the ij patch output charge can be written as:

$$\phi_{ij} = -\frac{h_{ij}^f}{S_{ij}^f} \int_{x_{j-1}}^{x_j} \int_{y_{i-1}}^{y_i} \left[h_{31} r_x^f \frac{\partial^2 z}{\partial x^2} + h_{32} r_y^f \frac{\partial^2 z}{\partial y^2} \right] dx dy \quad (2.91)$$

The charge ϕ_{ij} can be calculated by separating the equation into two:

$$\phi_{ij}^x = -\frac{h_{ij}^f}{S_{ij}^f} \int_{x_{j-1}}^{x_j} \int_{y_{i-1}}^{y_i} h_{31} r_x^f \frac{\partial^2 z}{\partial x^2} dx dy \quad (2.92)$$

$$\phi_{ij}^y = -\frac{h_{ij}^f}{S_{ij}^f} \int_{x_{j-1}}^{x_j} \int_{y_{i-1}}^{y_i} h_{32} r_y^f \frac{\partial^2 z}{\partial y^2} dx dy \quad (2.93)$$

The integration of Eq. (2.92) along x -direction and Eq. (2.93) along the y -direction yields the following equations:

$$\phi_{ij}^x = -\frac{h_{ij}^f}{S_{ij}^f} \int_{y_{i-1}}^{y_i} h_{31} r_x^f \left[\frac{\partial z}{\partial x} \right]_{x_{j-1}}^{x_j} dy \quad (2.94)$$

$$\phi_{ij}^y = -\frac{h_{ij}^f}{S_{ij}^f} \int_{x_{j-1}}^{x_j} h_{32} r_y^f \left[\frac{\partial z}{\partial y} \right]_{y_{i-1}}^{y_i} dx \quad (2.95)$$

If the slopes $z_x^{ij} = \partial z / \partial x$ in the x -direction and $z_y^{ij} = \partial z / \partial y$ in the y -direction are respectively assumed constant at the location of the i^{th} patch. These equations are similar in form to Eq. (2.83) however, their dependency on the gradient in the y -direction complicates the integration. In practice sensor strips output charges that account more for strains in the x -direction than in the y -direction. Therefore, multiple beam sensors could be used to measure the transverse vibration displacement curve of a plate. In the next section, we will derive equations that will prove this assertion.

Using Raleigh formulation, the mode shapes of a plate can be written as the product of beam functions:

$$W(x, y) = X(x)Y(y) \quad (2.96)$$

Where $X(x)$ and $Y(y)$ are chosen as the fundamental mode shapes of beams having the boundary conditions of the plate. This formulation works well for all plates boundary condition except for free edges where the approximate solution is required. Therefore, the

following discussion will focus on plates with clamped or simply supported edges. First, we will consider a case where the plate is vibrating at one of its fundamental frequency and second we will derive equations for the general case of plate vibration.

3.1.2.1 Plate Lateral Fundamental Vibration Displacement curve

Using Raleigh formation and Figure 3.7 the sensor strips respectively along the x – and y – direction, the output charges can be written as:

$$\phi_i^x = -\frac{h_i^f \Delta y}{S_i^f} h_{31_i} r_{x_i}^f z_x^i \quad (2.97)$$

$$\phi_i^y = -\frac{h_i^f \Delta x}{S_i^f} h_{31_i} r_{y_i}^f z_y^i \quad (2.98)$$

Based on the beam sensor theory, the plate deflection z_i^x and z_i^y along the PVDF strips can be written as

$$z_i^x \cong z_x^i (x_i - x_{i-1}) + z_{i-1}^x \quad (2.99)$$

$$z_i^y \cong z_y^i (y_i - y_{i-1}) + z_{i-1}^y \quad (2.100)$$

Where and z_x^i are respectively calculated from ϕ_i^x and ϕ_i^y . The following equation gives the resulting deflection of the plate. The above equation is only valid when the plate is vibrating at one of its fundamental frequencies. At resonance, the shape of the plate along the

$$z(x, y) \cong z^x z^y \quad (2.101)$$

x –direction remains constant across the y –direction while the shape of the plate along the y –direction remains constant across the x –direction. For a random vibration of the plate, these two sensor strips will only capture the deflections at their locations and Eq. 2.101 cannot be used.

3.2 Numerical Simulation

3.2.1 Beam Sensor

3.2.1.1 Numerical Simulation Equations

The forced lateral vibration steady-state response of a beam can be formulated in modal superposition form as shown in Eq. (3.1)

$$z(x) = \sum_{k=1}^m W_k \Psi_k(x) \quad (3.1)$$

Where k is the k^{th} mode number, W_k is the modal participation factor, Ψ_k the k^{th} mode shape, and m the maximum number of modes used in the approximation. The output of the i^{th} patch can be written using Eqs. (2.83), (2.89), and (3.1) as:

$$\phi_i = \frac{nh^f h_b h_{31}}{2l} \sum_{k=1}^m W_k \int_{x_{i-1}}^{x_i} \frac{\partial^2 \Psi_k}{\partial x^2} dx \quad (3.2)$$

To perform the numerical simulation, we will assume that the beam is excited by a general force vector $\{f\}$ of unity magnitude applied at a node and rewrite Eq. (3.1) in discretized form as:

$$\{z\} \cong \frac{\{\Psi_k\} \{\Psi_k\}^T \{f\}}{\omega_k^2 - \omega^2 + j\eta_k \omega_k^2} \quad (3.3)$$

Where ω is the excitation frequency, η_k is the structural damping factor of the k^{th} mode, ω_k the k^{th} natural frequency, and $\sqrt{j^2 = -1}$. It can be shown that

$$W_k \cong \frac{\{\Psi_k\}\{\Psi_k\}^T}{\omega_k^2 - \omega^2 + j\eta_k\omega_k^2} \quad (3.4)$$

Equation (3.3) is used to calculate the response of the beam and the mode participation factor W_k to a unit input force. The output charge of each patch is then calculated using modal coordinates W_k in Eq. (3.4). These output charges are then used in Eq. (2.86) to calculate the slopes a_i at the center of each patch before calculating the beam deflection using the central-difference equation (Eq. (2.88)). The deflection calculated from the sensor output charge and referred to as “Measured” is compared to the deflection calculated from the mode superposition equation and referred to as “Actual”. The results of the numerical simulation are discussed in the next section.

3.2.1.2 Numerical Simulation Results

The numerical simulation was performed for simply supported, clamped-clamped, and clamped-free boundary conditions. Low frequency (about 800Hz) excitation was applied to the beam using the data of Table 3.1. The admittance of each beam was calculated from Eq. (3.3) (we will refer to this as an actual response) and plotted against the admittance calculated from the sensor output using Eq. (2.90) (refer to this as a measured response). The admittance data was further process to extract the response of the beam at resonance for the first four modes. These four modes were selected arbitrary for brevity. The results are shown in Figs. (3.1-3.6) for the three types of boundary conditions considered for the beam.

Table 3.1: Simulation data for beam.

Aluminum Beam	PVDF
$l = 0.3556 \text{ (m)}$	$h^f = 50e^{-6} \text{ (m)}$
$b = 0.0254 \text{ (m)}$	$\frac{V}{m}$ $h_{31} = 0.4e^9 \left(\frac{m}{m}\right)$
$h^b = 0.003175 \text{ (m)}$	$\rho = 1789 \text{ (kg/m}^2\text{)}$
$\rho = 2767.849 \text{ (kg/m}^3\text{)}$	$E = 8.4e^9 \text{ (N/m}^2\text{)}$
$E = 71e^9 \text{ (N/m}^2\text{)}$	$\nu = 0.18$
$\eta = 0.002$	

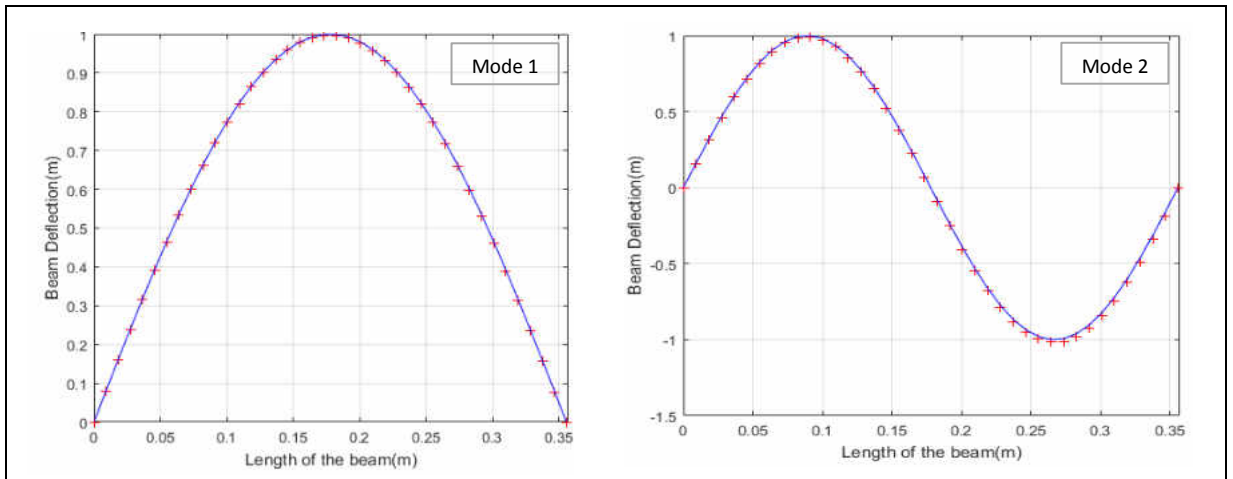


Figure 3.2: Beam (S-S) first and second mode response (Continuous= Actual; Dot=Sensor)

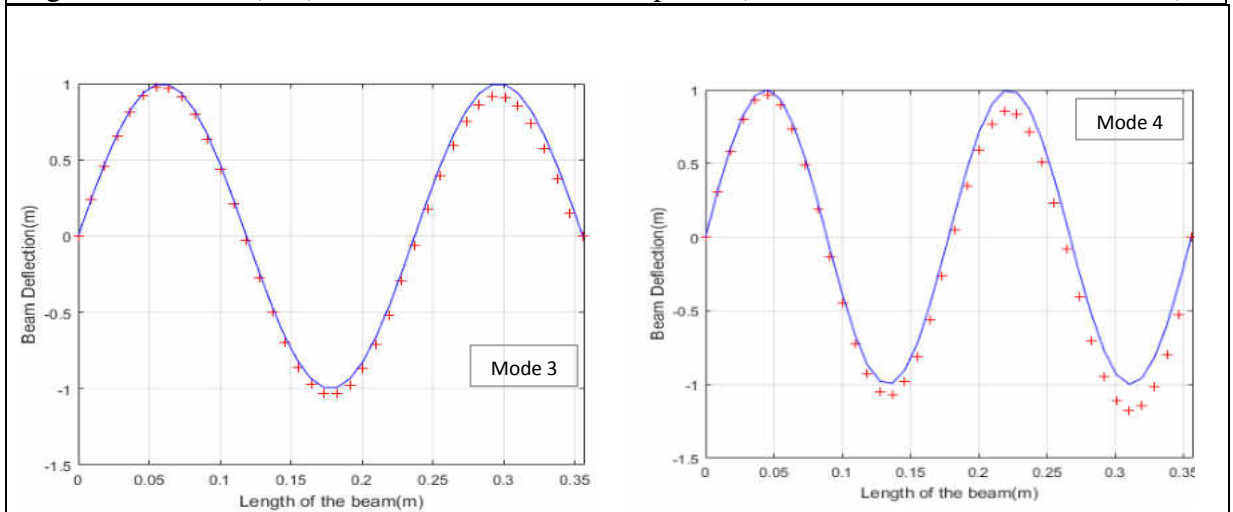


Figure 3.3: Beam (S-S) third and fourth mode response (Continuous= Actual; Dot=Sensor)

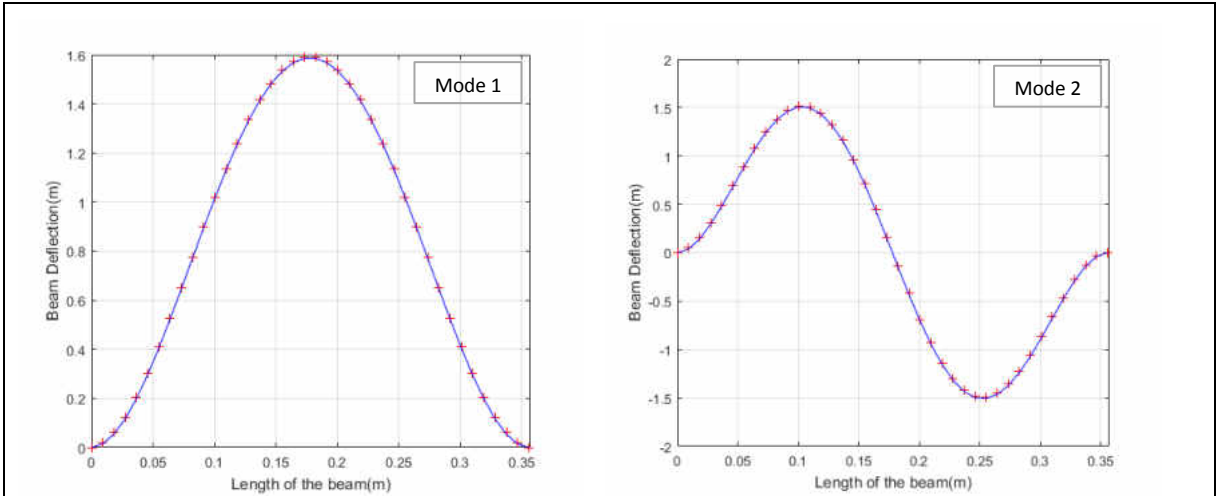


Figure 3.4: Beam (C-C) first and second mode response (Continuous= Actual; Dot=Sensor)

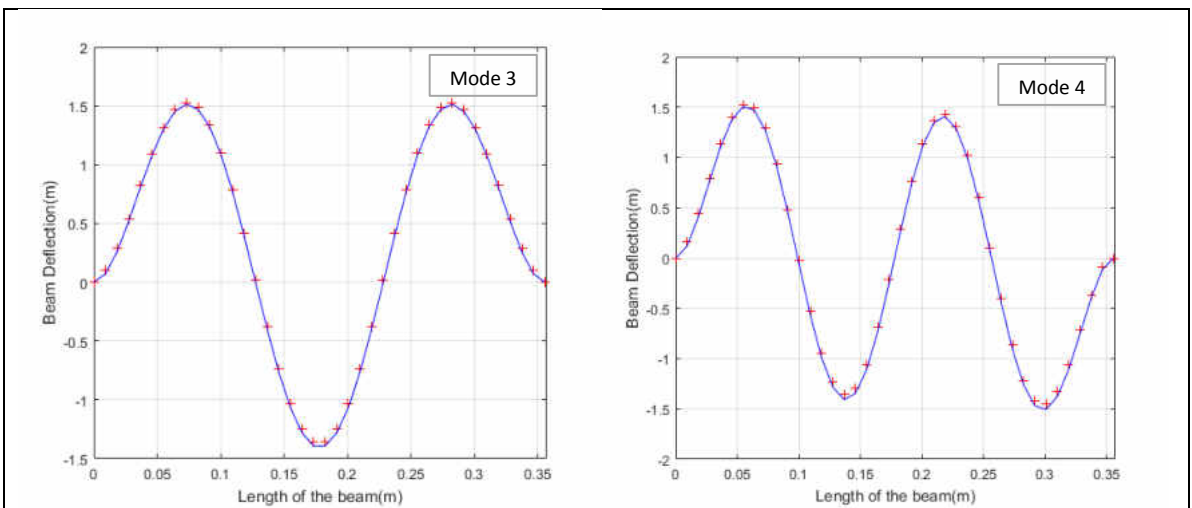


Figure 3.5: Beam (C-C) third and fourth mode response (Continuous= Actual; Dot=Sensor)

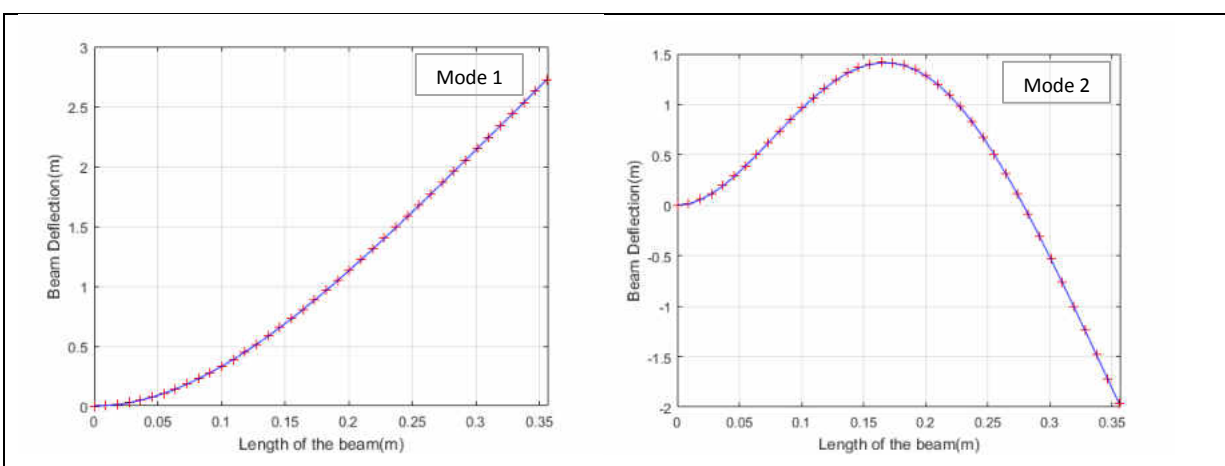


Figure 3.6: Beam (C-F) first and second mode response (Continuous= Actual; Dot=Sensor)

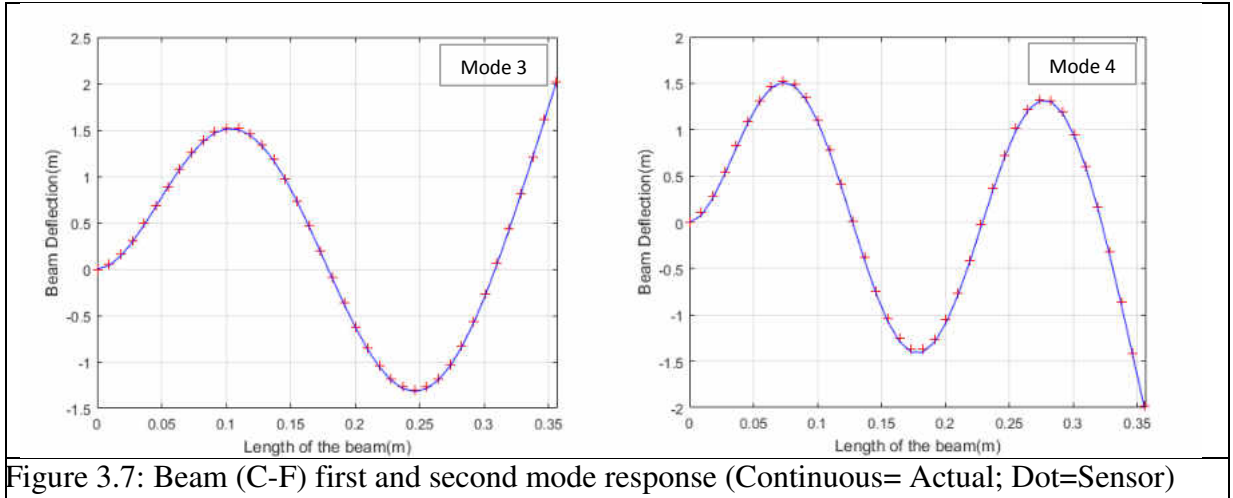


Figure 3.7: Beam (C-F) first and second mode response (Continuous= Actual; Dot=Sensor)

3.2.1.3 Frequency Calculations by using MATLAB

In this section we calculate the theoretical natural frequencies of the beam to utilize these frequencies to set the approximate boundary conditions on the beam in the experimental setup and measure the experimental natural frequencies. The vibration of the beam is referred to as a continuous system. The equations of motion defining the continuous systems are the partial differential equations. There are numerous cases of continuous systems such as longitudinal vibration of a bar, the transverse vibration of tight stretched cable or string, torsional vibration of shaft or rod, lateral vibration of beams; derived by considering an infinitesimally small element of the continuous system through the free-body diagram and applying Newton's second law of motion. The relevant boundary conditions of the system are used to obtain the vibration solution of the system giving infinite natural frequencies and mode shapes.

In distributed or continuous systems, it is not possible to distinguish between masses, springs, and dampers. In such cases we must assume that each infinite number of points of the system can vibrate. Hence a continuous system also referred to a *system of*

the infinite degree of freedom. The frequency of beam with common boundary conditions (in rad/s) is given by:

$$\omega_n = (\beta_n l)^2 \sqrt{\frac{EI}{\rho A l^4}} \quad (3.9)$$

Converting to Hz, we get the natural frequency as:

$$f_n = \frac{\omega_n}{2\pi} \quad (3.10)$$

MATLAB code was written to calculate the natural frequencies of the beam. The physical and material properties of the beam were assigned to parameters in the MATLAB code. Constants for the boundary conditions and the modes shapes function for different boundary conditions of the beam were used from Table 3.2 [2].

Table 3.2: Boundary Condition and characteristics of the vibrating beam

Sr. No.	Configuration of beam	Frequency Equation	Mode Shape	Value of $\beta_n l$
1.	Pined-Pined	$\sin\beta_n l = 0$	$W_n(x) = C_n[\sin\beta_n x]$	$\beta_1 l = \pi$ $\beta_2 l = 2\pi$ $\beta_3 l = 3\pi$ $\beta_4 l = 4\pi$
2.	Fixed-Fixed	$\cos\beta_n l = 1$ $\cos\beta_n l = 1$	$W_n(x) = C_n[\sinh\beta_n x - \sin\beta_n x + \alpha_n(\cosh\beta_n x - \cos\beta_n x)]$ Where $\alpha_n = \frac{\sinh\beta_n l - \sin\beta_n l}{\cos\beta_n l - \cosh\beta_n l}$	$\beta_1 l = 4.730041$ $\beta_2 l = 7.853205$ $\beta_3 l = 10.994757$ $\beta_4 l = 14.137165$
3.	Fixed-pinned	$\tan\beta_n l - \tanh\beta_n l = 0$	$W_n(x) = C_n[\sin\beta_n x - \sinh\beta_n x + \alpha_n(\cosh\beta_n x - \cos\beta_n x)]$ Where $\alpha_n = \frac{\sinh\beta_n l - \sin\beta_n l}{\cos\beta_n l - \cosh\beta_n l}$	$\beta_1 l = 3.926602$ $\beta_2 l = 7.068583$ $\beta_3 l = 10.210176$ $\beta_4 l = 13.351768$

Table 3.3: Natural Frequencies of Beam with boundary conditions

No. of Modes	<i>CC</i>	<i>SS</i>	<i>CF</i>
1	129.6944	56.8243	20.5347
2	360.2623	227.2972	128.6897
3	706.1141	511.4188	360.3282
4	1167.2	909.1889	706.1174
5	1743.7	1420.6	1167.2

3.2.2 Plate Sensor

3.2.2.1 Numerical Simulation Equations

The validity of Eqs. 2.101 is tested using numerical simulation with MATLAB. The data from Then using the layout of Figure.3.7, the charges ϕ_i^x and ϕ_i^y are calculated from Eq. 2.82 before the deflections z_{ij}^x and z_{ij}^y are calculated from Eqs. 2.99 and 2.100.

Table 3.4 below is used in the simulation. For the case of the plate vibration at one of the fundamental frequencies, we arbitrarily selected modes (1,1),(1,2),(2,1), & (2,2) to calculate the “actual” deflections of the plate using Eq. 3.5 for the simply supported plate and Eq. 3.6 for the clamped plate.

$$z(x, y) = \left[\sin\left(\frac{n\pi x}{L_x}\right) \right] \left[\sin\left(\frac{m\pi y}{L_y}\right) \right] \quad (3.5)$$

$$z(x, y) = \left[\sin\left(\frac{n\pi x}{L_x}\right) \right] \left[\sin\left(\frac{m\pi y}{L_y}\right) \right] \quad (3.6)$$

Then using the layout of Figure.3.7, the charges ϕ_i^x and ϕ_i^y are calculated from Eq. 2.82 before the deflections z_{ij}^x and z_{ij}^y are calculated from Eqs. 2.99 and 2.100.

Table 3.4: Simulation data for plate.

Aluminum Plate	PVDF
$l = 0.610 \text{ (m)}$	$h^f = 50e^{-6} \text{ (m)}$
$b = 0.381 \text{ (m)}$	$h_{31} = 0.4e^9 \left(\frac{V}{m}\right)$
$h^b = 4.76e^{-3} \text{ (m)}$	$\rho = 1789 \text{ (kg/m}^2\text{)}$
$\rho = 2767.849 \text{ (kg/m}^3\text{)}$	$E = 8.4e^9 \text{ (N/m}^2\text{)}$
$E = 71e^9 \text{ (N/m}^2\text{)}$	$\nu = 0.33$

The “measured” deflections of the plate are calculated from Eq. 2.101. Figures (3.8-3.11) show the plots of the “Actual” and “Measured” deflections. The results indicate that PVDF sensor strips can be used to validate the Raleigh formulation of the mode shape of plates and the measurement of deflection curve theory presented for vibration at resonance.

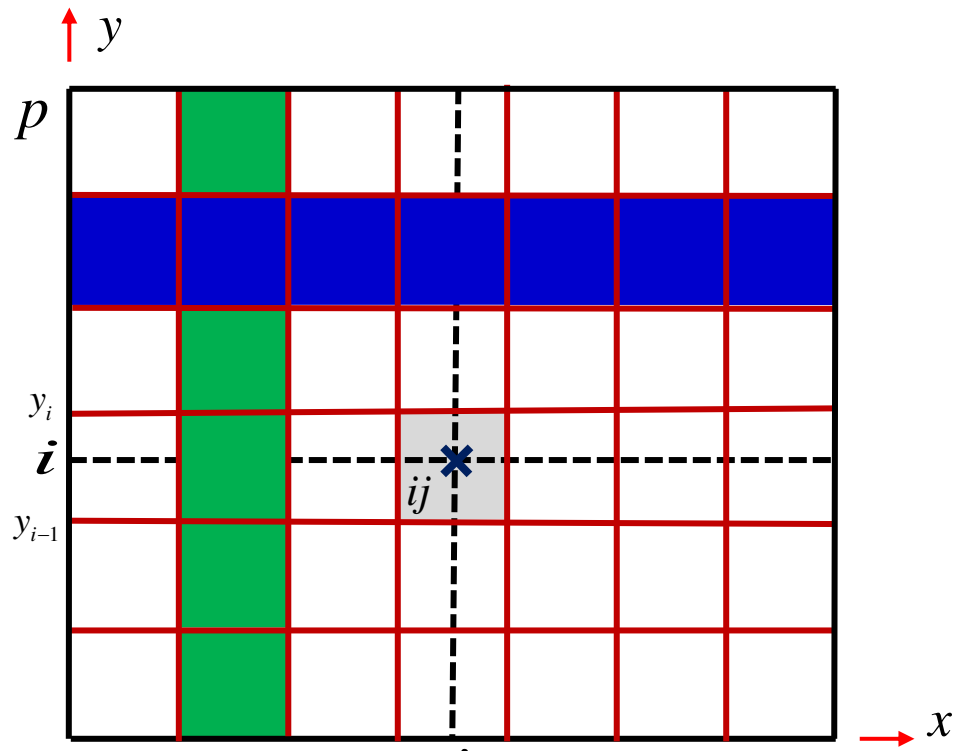


Figure 3.8: Layout of the PVDF sensor across plate for measuring plate deflection curve at resonance

Figure 3.7 describes the process to place the PVDF films in such a way to measure the deflection of the vibrating plate at resonance. The blue section represents the PVDF film along x -axis of the plate whereas the green section represents PVDF film along the y -axis of the plate. Only two films are enough to measure deflection across the plate because at resonance the deflection along the x -axis is constant along the y -axis and the deflection along the y -axis is constant along the x -axis for the plate. Implementing multiple films along x & y -direction will yield same results. Hence, only two films are employed to measure the plate deflection.

3.2.2.2 Numerical Simulation Results

The numerical simulation was performed for simply supported, clamped-clamped, and clamped-free boundary conditions. Low frequency (about 800Hz) excitation was applied to the beam using the data of Table 3.4. The admittance of each beam was calculated from Eq. (3.3) (we will refer to this as an actual response) and plotted against the admittance calculated from the sensor output using Eq. (3.5 & 3.6) (refer to this as a measured response). The admittance data was further processed to extract the response of the beam at resonance for the first four modes. These four modes were selected arbitrarily for brevity. The results are shown in Figs. (3.8-3.11) for the three types of boundary conditions considered for the beam.

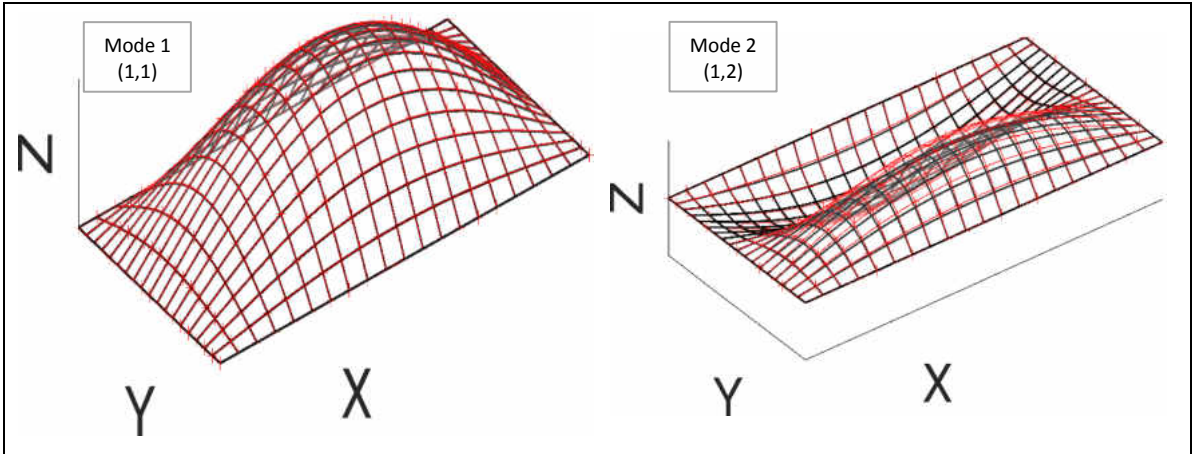


Figure 3.9: Plate (S-S) first and second mode response (Continuous= Actual; Dot=Sensor)

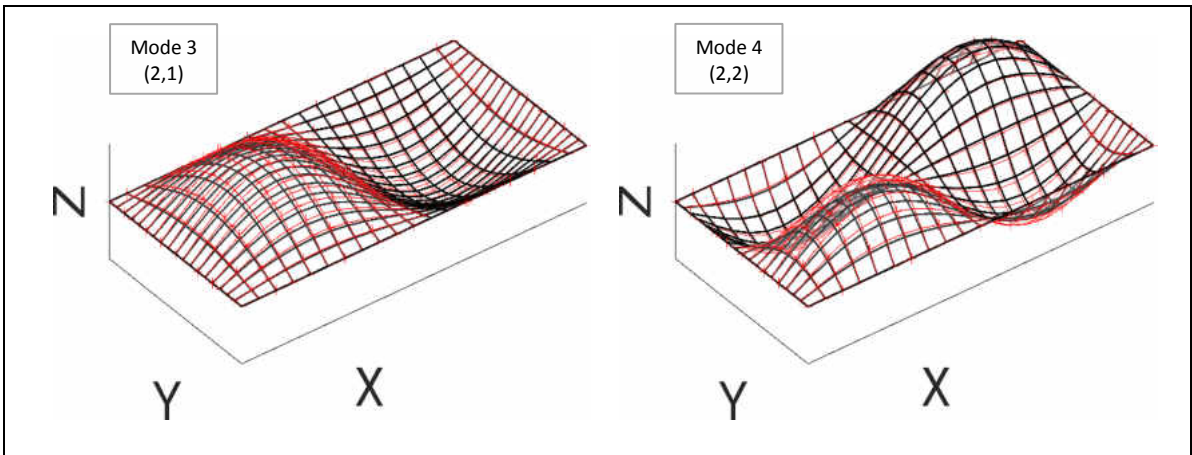


Figure 3.10: Plate (S-S) third and fourth mode response (Continuous= Actual; Dot=Sensor)

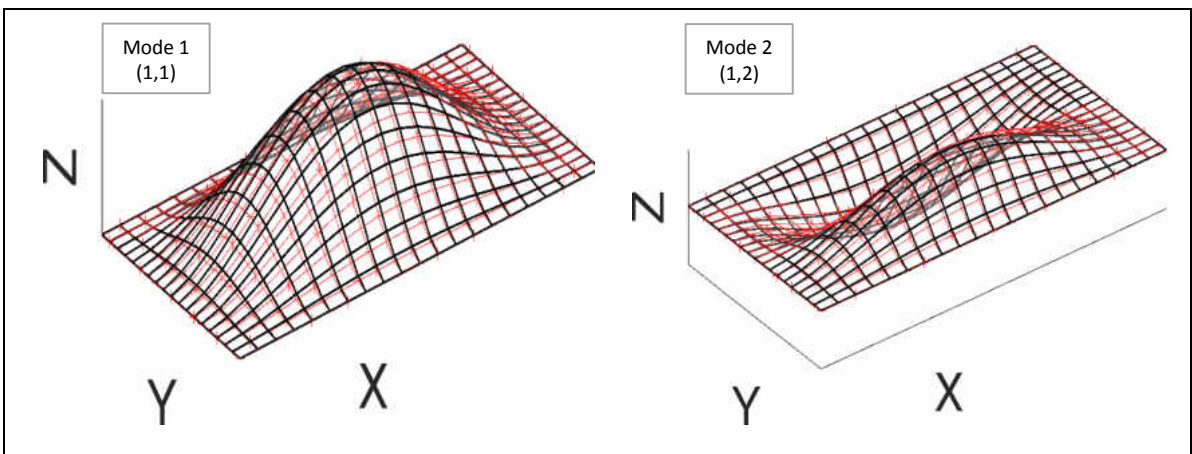


Figure 3.11: Plate (C-C) first and second mode response(Continuous= Actual; Dot=Sensor)

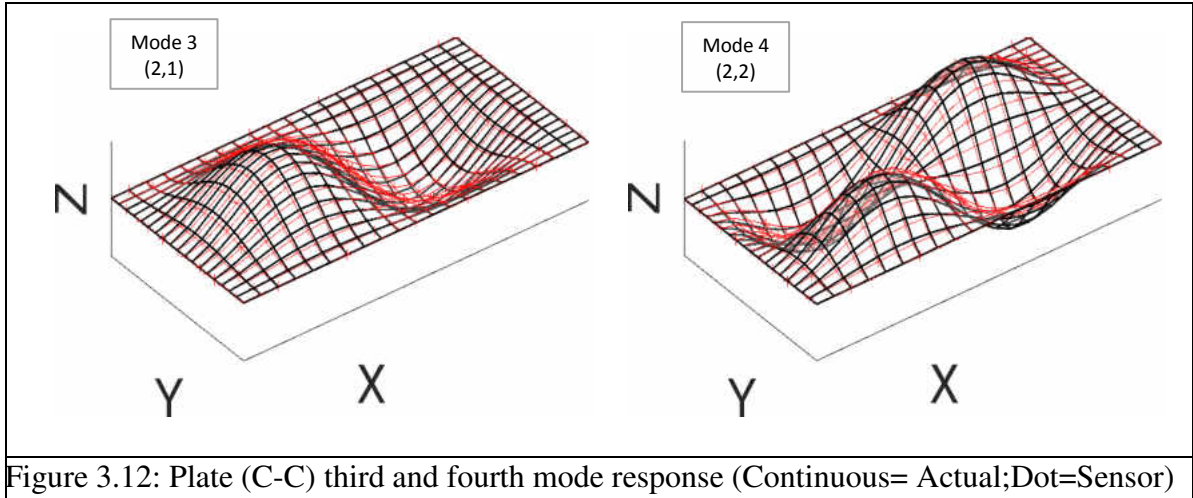


Figure 3.12: Plate (C-C) third and fourth mode response (Continuous= Actual;Dot=Sensor)

3.2.3 Multiphysics Simulation

Multiphysics modeling bridges the gap between the real-life problems involving physical phenomenon and simulations to acquire most accurate results. ANSYS Workbench was used for conducting finite element analysis. Finite element analysis serves needs to several streams in engineering sectors like static, dynamic, heat flow, fluid flow, electromagnetics and coupled field problems. A Multiphysics analysis is a combination of analyses, involving different streams of engineering to solve a global engineering problem. Load acts over surfaces or volume according to the input parameter provided by the user. The solution obtained on finite elements basis is always an approximate solution, and one needs to decide whether it is a good or bad solution. However, in the presence of experimental or analytical results, it is easy to verify finite element results. Simulations involve the structural model constraining with required boundary conditions to obtain the desired output. The finite analysis steps involve pre-processing, solution and post-processing.

3.2.3.1 Preprocessing

Preprocessing step consist of defining the real constant such as geometrical and material parameter of the beam. *ANSYS Workbench 16.0* is the tool used for modal analysis purpose. Select *Modal* analysis section in workbench to perform modal analysis of the plate and beam. Define material properties like Young's Modulus; select aluminum as material from the available *Engineering data* section under Modal analysis.

3.1.1.1.1 Geometry

Under *Geometry* construct the plate and beam with line element for modal analysis purpose and choose the rectangular cross-section. Line elements selection surpasses the classic solid element not only possess displacement degree of freedom, but also rotations. Elements are available in ANSYS according to the Timoshenko theory and Bernoulli theory. Shear stresses are calculated for Timoshenko theory and not for Bernoulli theory. Therefore, we prefer the latter through use of line element. Bending stresses are available for both theories. Use the *Properties* tabs to assign length, width and height as 0.3556m, 0.0254m and .00375m respectively for the beam. These parameters correspond to the actual specimen dimension. The beam dimensions are same for various boundary conditions; hence one geometry can be assigned to different modal analysis with respective boundary conditions prevailing. Similarly construct the model for plate. Figure 3.13 shows beam geometry in ANSYS.

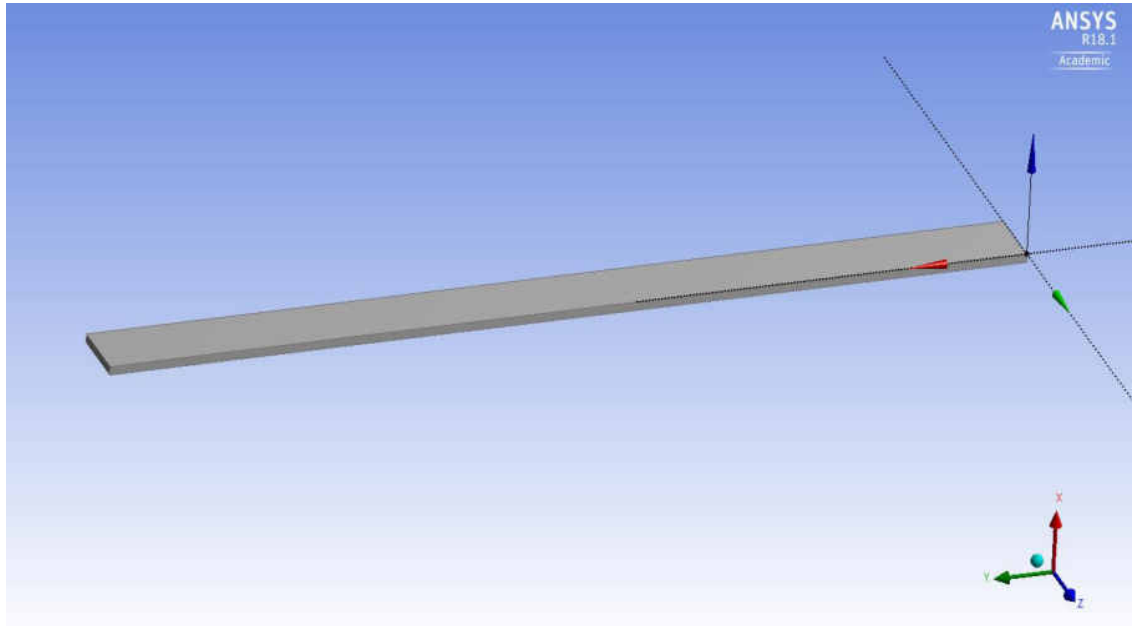


Figure 3.13: Geometry of beam in ANSYS

3.1.1.1.2 Mesh Size

Now we need to define the mesh size of the structures. Meshing is the process that divides the structure component into small elements uniformly distributed the load applied on the component. Components can be analyzed without or with meshing; the latter is preferred. After meshing the entire structure is divided into some elements and each element has its own stiffness while loading. Adding all those elements stiffness's, derive the global stiffness matrix which helps in calculating the stress developed in structure. Without meshing the load distribution is not uniform which causes irregular or faulty results. Mesh size used in this analysis is 0.05. Lower the mesh size used, finer are the results. With low mesh size, results of natural frequencies are closer to the ones' calculated by MATLAB in section 3.3.2

Assign aluminum material which was earlier specified in the engineering data. Three different modal analysis is performed due to three boundary conditions of the beam i.e. simply supported, clamped-clamped and clamped-free, i.e. clamped-clamped. The boundary conditions are applied at the ends of the beam for the respective modal analysis.

3.2.3.2 Numerical Solution and results

As we do modal analysis, it is also necessary to specify the number of modes for the vibrating plate and beam, to display the mode shapes. Out of the different modal analysis setups, select either of the setups and here we select three modes of vibration. To solve the analysis setup, give the generate command which returns three natural frequencies for three modes for vibrating beam. Select the natural frequencies and solve them to generate mode shapes of respective frequencies. Figure 3.14, Figure 3.15 and Figure 3.16: S-S Beam third mode of vibration at frequency 519.53 Hz shows modes shapes for the first three modes of vibration for simply supported boundary conditions of the beam. Figure 3.17, Figure 3.18 and Figure 3.19, represent modes shapes for the first three modes of vibration for clamped-clamped boundary conditions of the beam. Figure 3.20, Figure 3.21 and Figure 3.22 illustrate modes shapes for the first three modes of vibration for clamped free boundary conditions of the beam.

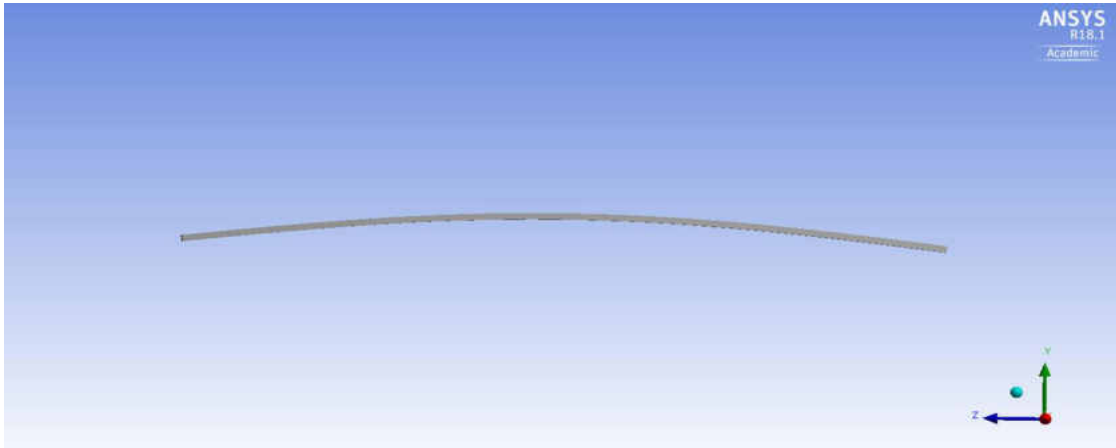


Figure 3.14: S-S Beam first mode of vibration at frequency 56.672 Hz

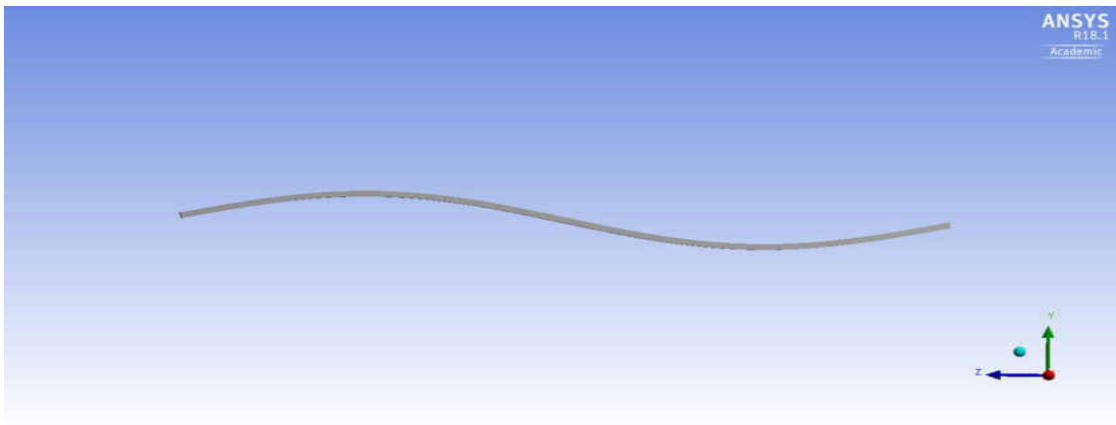


Figure 3.15: S-S Beam second mode of vibration at frequency 230.77 Hz

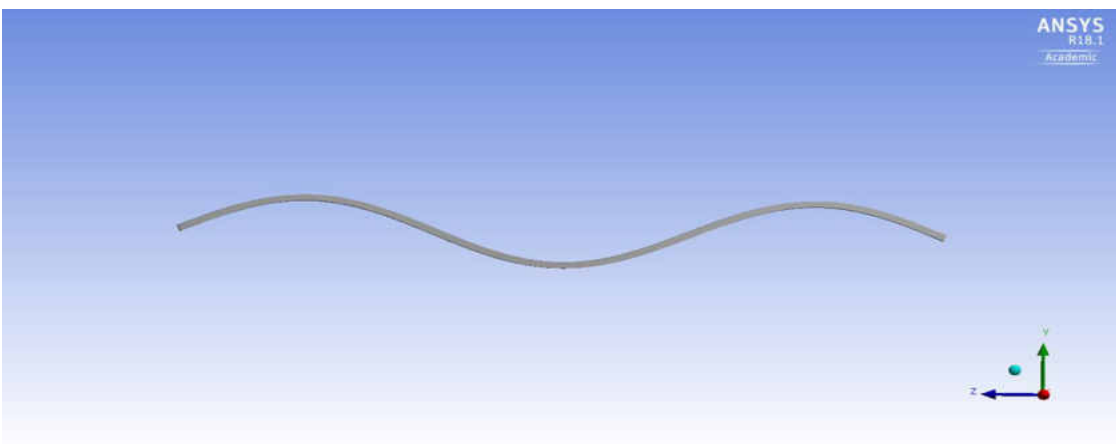


Figure 3.16: S-S Beam third mode of vibration at frequency 519.53 Hz

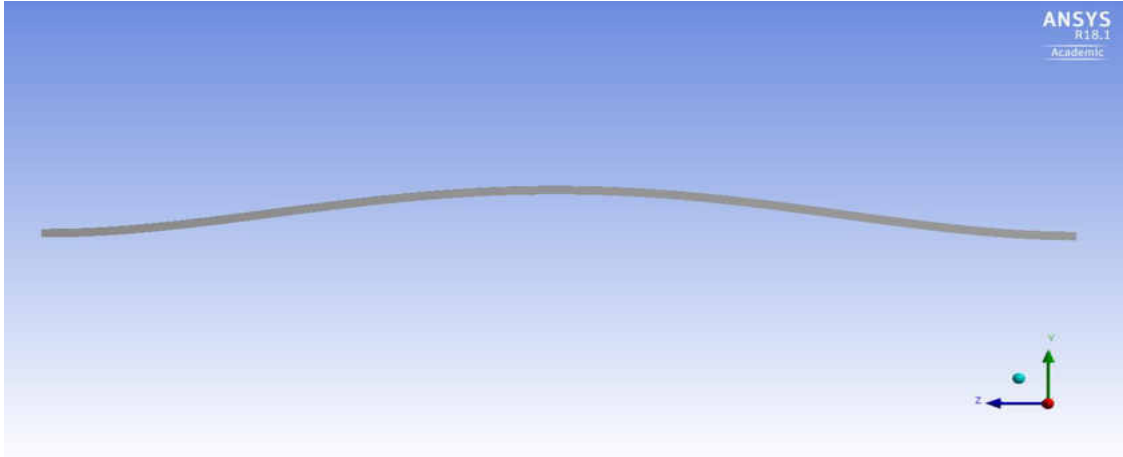


Figure 3.17: C-C Beam first mode of vibration at frequency 129.44 Hz

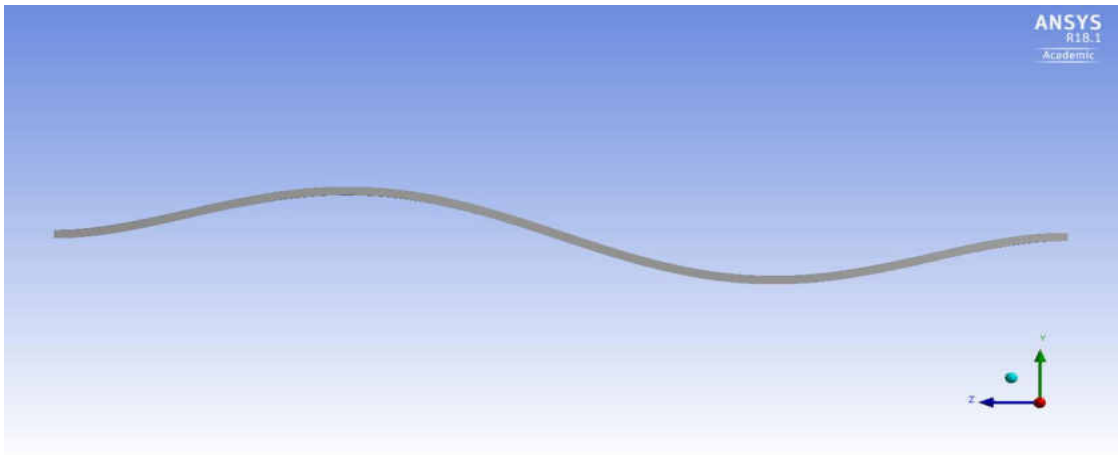


Figure 3.18: C-C Beam second mode of vibration at frequency 358.88 Hz

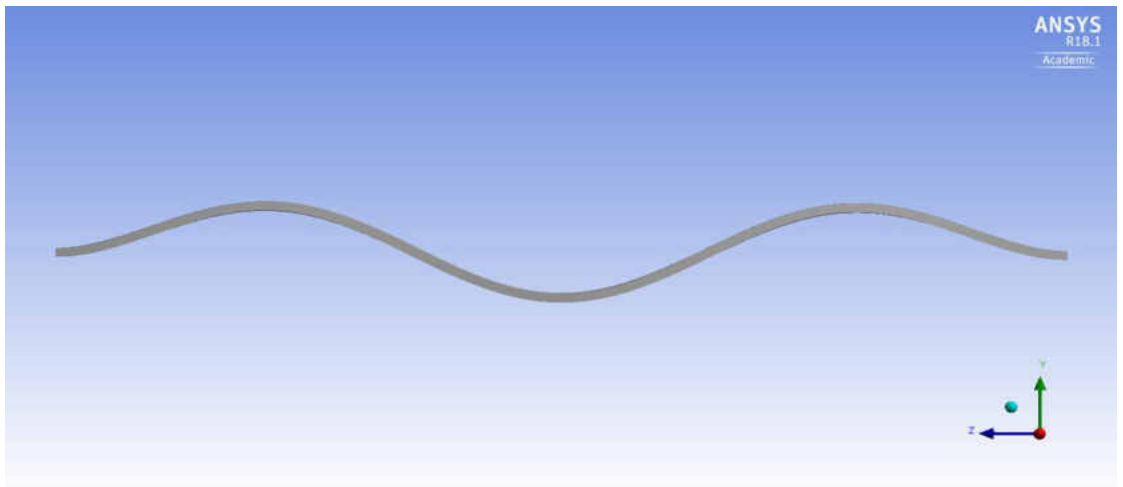


Figure 3.19: C-C Beam third mode of vibration at frequency 706.64 Hz

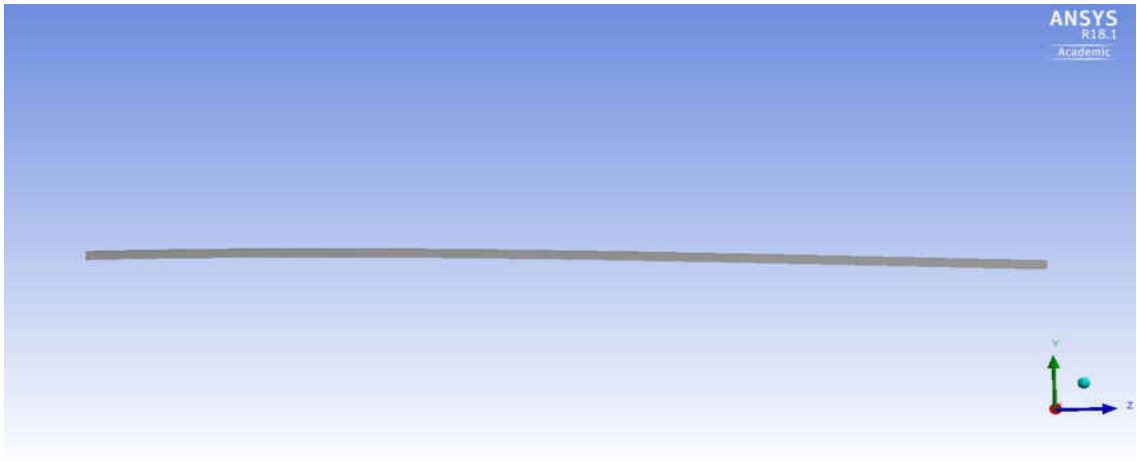


Figure 3.20: C-F Beam first mode of vibration at frequency 20.771 Hz

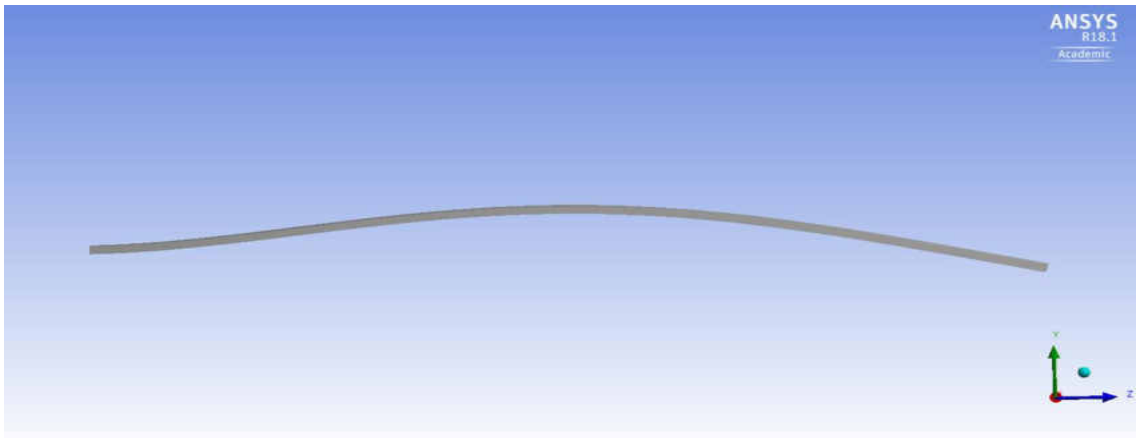


Figure 3.21: C-F Beam second mode of vibration at frequency 130.04 Hz

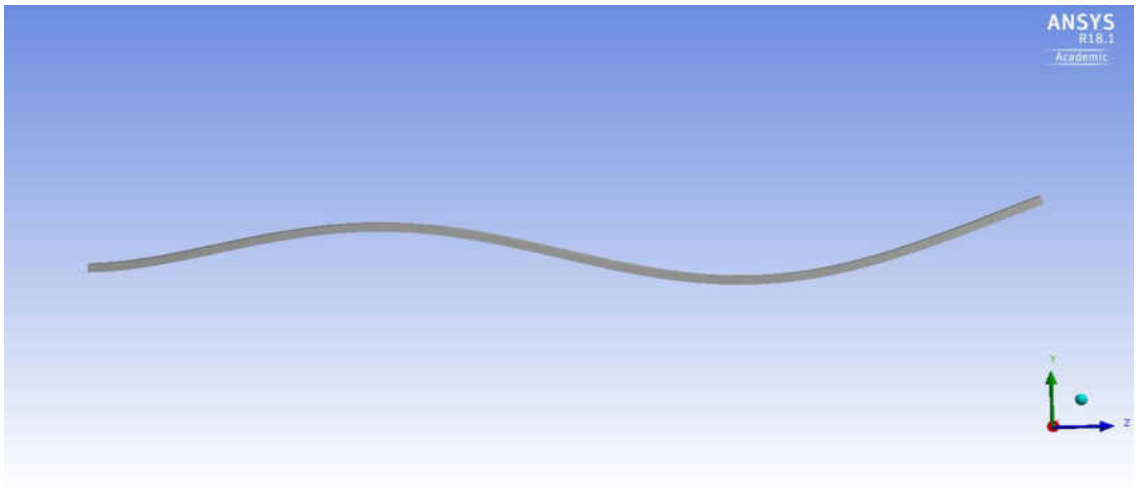


Figure 3.22: C-F Beam third mode of vibration at frequency 364.41 Hz

3.2.3.3 Post-processing and results

The final step for Multiphysics simulation comprises of verification and validation of the results obtained from simulation. The simulation frequencies are substituted in the final solution to observe the modes shapes and structural deformations visually. Thus, confirming the boundary conditions applied are correct. Firstly, for our verification, we focus on first three modes of vibration. However, the reason for considering first five modes is because for the sixth mode of vibration and onwards the frequency goes beyond 1000Hz and we are considering frequencies less than 1000Hz for verification purpose. The frequencies acquired in post-processing are compared to the frequencies calculated through MATLAB and are represented in Table 3.5 and Table 3.6 below represents frequencies acquired from numerical calculations and Multiphysics simulation and the percentage error in comparing the frequencies respectively.

The error percentage is mostly less than 2% and in some cases for S-S boundary condition is above 2%, but the error is well in limits to consider the results to be a good match. Here it is to be noted that ANSYS beam element formulation used is Timoshenko beam theory whereas MATLAB calculation is based on Euler-Bernoulli theory. As the number of modes increases, there are discrepancies observed between the frequencies derived from MATLAB and ANSYS. The reasons can be described as the mesh size; need to find the adequate mesh size and the two-different process (MATLAB and ANSYS) return results prescribed on different theories. ANSYS simulation results are an approximation of the natural frequencies based on Timoshenko beam theory which includes shear -deformation effect, which is neglected in Euler-Bernoulli theory.

Table 3.5: Theoretical and finite element beam natural frequencies

Mode Number	Theoretical Natural Frequencies (Hz)			Finite Element Natural Frequencies (Hz)		
	S-S	C-C	C-F	S-S	C-C	C-F
1	56.8243	129.6944	20.5347	57.672	129.44	20.771
2	227.2972	360.2623	128.6897	230.77	358.88	130.04
3	511.4188	706.1141	360.3282	519.53	706.64	364.41
4	909.1889	1167.2	706.1174	924.22	1172	710.41
5	1420.6	1743.7	1167.2	1445	1754.8	1171.36

Table 3.6: Percentage error for analytical and simulation calculation.

Sr. No.	% Error		
No. of Modes	S-S	C-C	C-F
1	1.541567037	-0.196153419	1.13764383
2	1.756051176	-0.383692659	1.038372808
3	2.015787255	0.074478048	1.120111962
4	2.219878903	0.411240576	1.292020801
5	2.276948476	0.636577393	1.493796945

This comparison is a vital part of the experimental setup that was built later. When the MATLAB and ANSYS natural frequencies confirm a match, thus lay the foundation of practical demonstration of measuring the deflection curve by observing the natural frequencies through the experimental setup. Match in natural frequencies from MATLAB calculations and ANSYS simulation triggers the process of implementing the boundary conditions for the actual experimental setup. In other words, the experimental setup to be built should be as close as possible to the ANSYS model regarding boundary conditions.

CHAPTER IV

EXPERIMENTAL DISPLACEMENT MEASUREMENT

4.1 Beam Experimental Displacement Measurement

To validate the results of theoretical calculations, an experiment was conducted. A set-up accommodating all three boundary conditions was constructed. The set-up was constructed in such way that no boundary condition was permanently applied to the specimen (as a permanent application of boundary condition will force us to construct multiple set-ups) as we must experiment with varying boundary conditions on the same base construction saving time and material required for multiple set-ups. The clamped-



Figure 4.1: Setup for Clamped-Clamped boundary condition of the beam.

clamped boundary conditions refer to no rotational, lateral or longitudinal movement of the beam in either direction at the boundary and hence the plates are bolted as shown in

Figure 4.1. When the bolts are tightened, it must be taken care that excess tightening will result in bending of the beam. This deformation beyond a point is detrimental to the beam hence adequate tightening of the bolts is recommended. Hence, we had to monitor the natural frequency readings on the digital analyzer and keep tightening the bolts up to the point where the readings on the analyzer screen have an approximate match to the theoretically calculated frequencies. For such supporting of the beam between the bolted plates, the beam had to be longer than 14 inches as supporting with exact length was impractical. The longer beam was taken, but the distance between the supporting pillars was maintained to 14 inches, limiting the beam length to be within 14 inches.



Figure 4.2: Setup for Simply Supported boundary condition of the beam.

Setup for simply supported boundary conditions on either side of the beam is shown in Figure 4.2. The simply supported boundary conditions on either side of the beam was an intricate task. Rotational, lateral and longitudinal motion are prevented. A peculiar characteristic design was adopted which included rectangular shapes small structures supporting the beam on top and bottom on either side creating knife edges. Lastly, the

clamped free boundary condition is reflected in Figure 4.3. Material and geometrical properties of the beam are shown in Table 4.1. Before the sensor was attached to the beam, an accelerometer was used to measure the deflection curve of the beam. This task was accomplished by mapping the area on the beam surface.

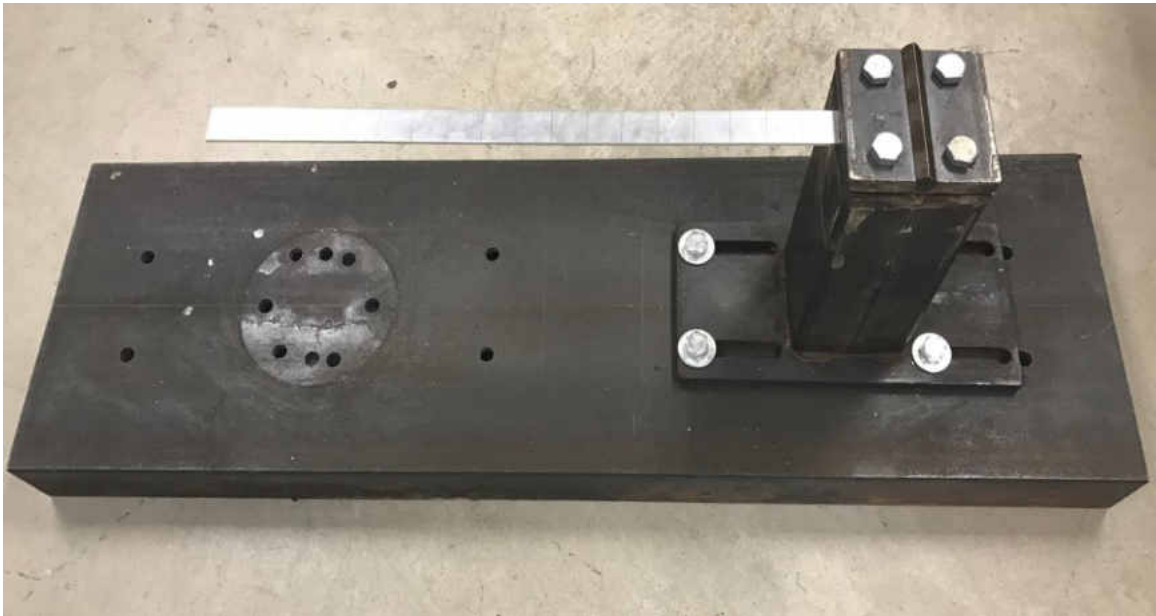


Figure 4.3: Setup for Clamped-Free boundary condition of the beam.

Table 4.1: Properties of the test specimen.

Sr. No.	Properties	Values	Units
1.	Material	Aluminum	-
2.	Density	2767.849	(kg/m^3)
3.	Young's Modulus	71×10^9	-
4.	Length (L)	0.3556	m
5.	Breadth (b)	0.0254	m
6.	Height (h)	0.003175	m

The measurement procedure is described in detail, in section 4.1.2. The data acquisition system is comprised of Hewlett Packard (HP) Dynamic Signal Analyzer (DSA) (model 35670 A). An electrodynamic shaker (model ET-132-2) by Techron power amplifier (model 5507) was the excitation source for the beam specimen. Fundamental resonance for the electrodynamic shaker is 7500 Hz which is above the frequency limit of our measurement of 800 Hz, as we focus on the first three modes. PCB Piezoelectric accelerometer was used to acquire the vibration reading and signals were passed through a PCB signal conditioner (model 480E09).

4.1.1 Sensor shaping and fabrication

The sensor layout is first designed in SolidWorks and then printed on a self-adhesive vinyl sheet. This sensor layout is then cut from the self-adhesive with the help of printer-cutter, thus generating a sensor template as shown in Figure 4.4. Here the template represents the sensor design, having slits at regular intervals of 1 inch. The template is laid on top of the film, as shown in Figure 4.5(a) before an etching ink is applied in the slits. The etching solution is applied with the help of a brush, as shown in Figure 4.5(b), therefore corroding the PVDF film's piezoelectric property. This etching solution can stay on the film for about a day and then the template is removed from the film hence forming a distributed PVDF film sensor with 14 PVDF segments and the corroded portion differentiating between the PVDF film segments on one side and a continuous electrode on the others side of the film. A multimeter is used to ensure the patches are electrically isolated from each other shown in Figure 4.5(c), therefore serving the purpose of the distributed sensor.

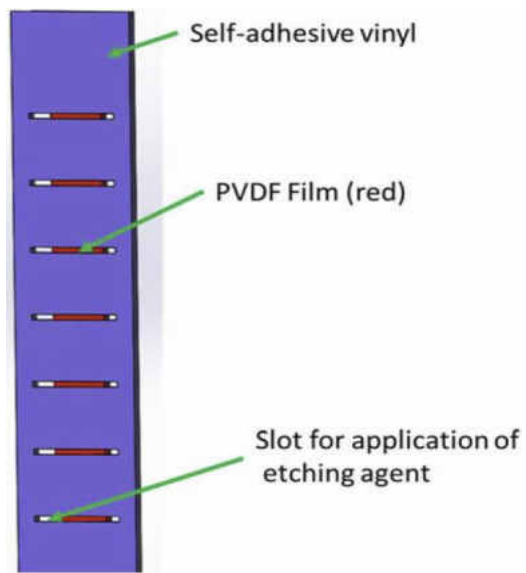


Figure 4.4: Sensor template.

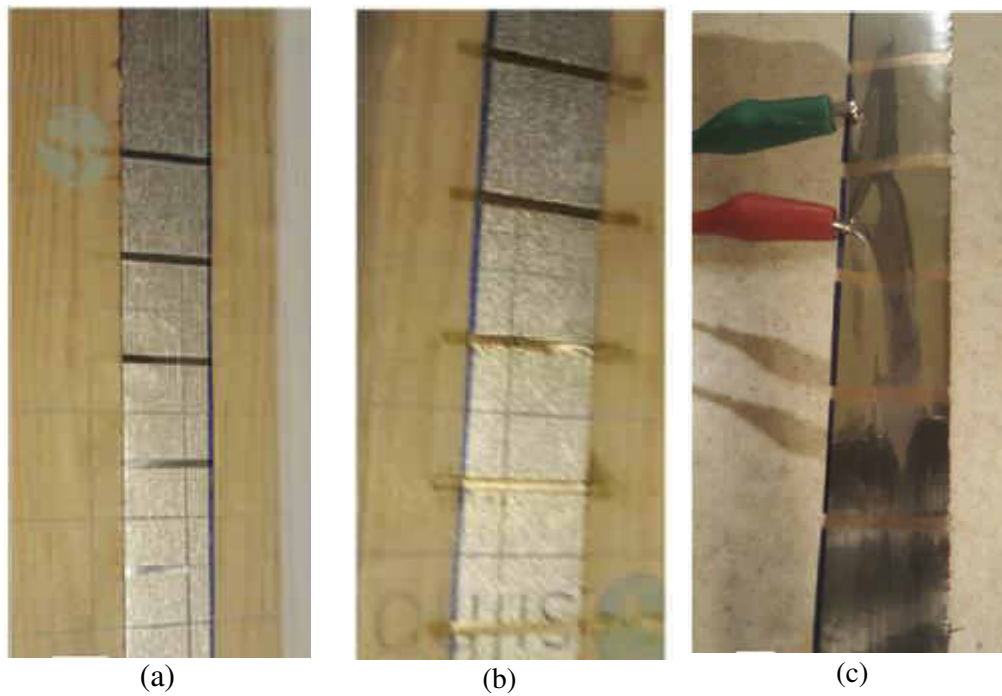


Figure 4.5: Sensor fabrication details.

4.1.2 Experimental Measurement Procedure for beam

The beam length was kept constant throughout the experimental procedure. The experiment to calculate the deflection curve of the vibrating beam was first done with an accelerometer. The schematic diagram for experimental setup of the beam is shown in Figure 4.6. For this, the beam was divided equally into 14 parts, each measuring 1 inch, as shown in Figure 4.7. The accelerometer was placed individually on each of the 14 parts (as shown in Figure 4.7) recording the acceleration measurement per part. The shaker was placed beneath the beam with the stringer (on the shaker) just touching the beam. The shaker was connected to the amplifier, which in turn was connected to the input port of the Dynamic Signal Analyzer. The force gauge, on the other hand, is connected to a signal conditioner which was connected to Channel 1 of Dynamic Signal Analyzer. The frequency supplied by the shaker was set within a range of 0-800 Hz through the analyzer. As mentioned earlier, we focus our attention on response with a frequency less than 800 Hz and data recorded beyond 800 Hz though measured will be not be considered in evaluating the sensor accuracy. The accelerometer is connected to the PCB signal conditioner for signal conditioning before it is connected to the Channel 2 of the Dynamic Signal Analyzer. Fast Fourier Transform (FFT) program was selected from the Digital Signal Analyzer for processing the measurements. The shaker is turned on and the amplifier is used to adjust the volume of the vibration to a level that's easily perceived by human ears. Then the accelerometer was placed at each of the 14 parts on the beam measuring the acceleration of each part individually. Here, wax was used to attach the accelerometer to the beam. These measurements were stored in the Digital Signal analyzer for a range over 0-800Hz and were saved in the form of data points to be analyzed later. Each of the 14 data points

(measured from the 14 parts of the beam) consist the average of 20 acceleration measurements at a point on the beam, i.e., a single data point is the average of 20 measurements. The measurements recorded through the analyzer were extracted through a floppy drive and processed through MATLAB.

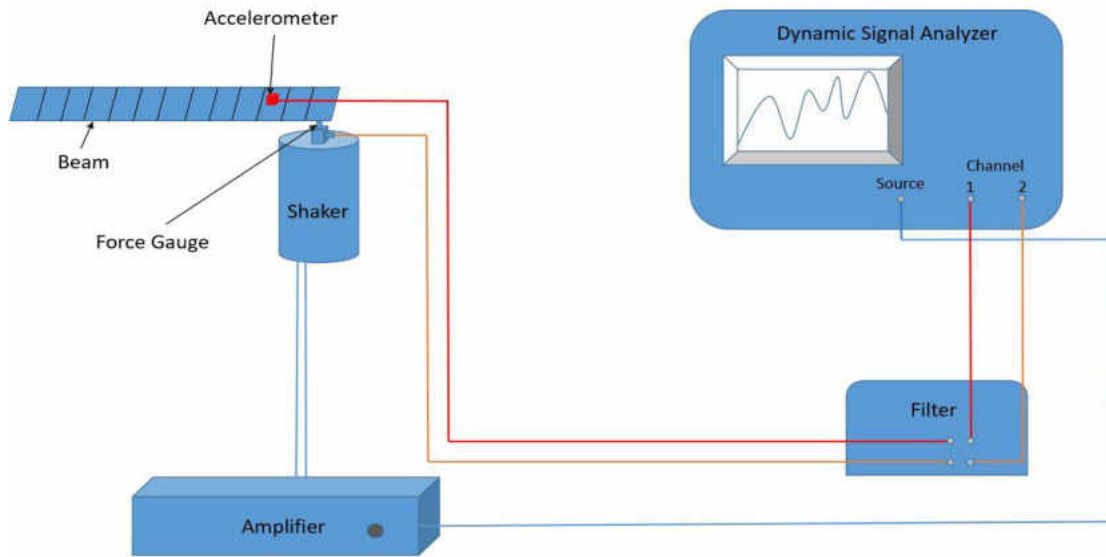


Figure 4.6: Beam Experimental Setup using an accelerometer

While recording these measurements for the beam, we need to vary the boundary conditions but the process of measuring the frequency is same. For C-C boundary condition the beam accounts for 14 measurements whereas the two supporting columns on either side account for 2 measurements. This forms the first observation set for C-C boundary condition comprising of 16 measurements. A similar process is adopted for the S-S boundary condition leading to second observation set with again 16 measurements. For the C-F boundary condition there is only one supporting column, hence the third observation set consist of 15 measurements (14 measurements form the sensor film while 1 measurement from the supporting column). Therefore, 3 different observation sets with different boundary conditions are obtained, though the measurement procedure was same.

It is to be noted that once measurement process has started for a given boundary condition of the beam, a complete set of readings must be recorded for that boundary condition before switching off the equipment. (shaker, analyzer, filter & amplifier)

The experiment to measure the deflection curve of the vibrating beam with PVDF sensor is similar in approach as mentioned above with a difference that etched PVDF film replaces the accelerometer. Solutions like dilute phosphoric acid and ammonia water with sandpaper were used to cleanse the beam surface from any dirt and wax. Then follows the task to adhere the sensor to the beam top surface. Following the etching process mentioned in section 4.1.1, the sensor was then bonded to the beam surface with the help of double-sided tape (Letraset dual Tack, 50 mm wide). The sensor film width extension is vital from a wiring point of view. If the sensor film width were exact as that of the beam, it would have been impossible to reach the surface beneath the sensor (i.e., the electrode on the other side of the sensor film), as one surface serves as a positive electrode and other as negative. For the wiring, it is important that these electrodes be completely isolated from each other. The PVDF film on beam was etched on one side and consisted of a continuous electrode surface on the other. Therefore, one wire will always be in contact with the continuous electrode surface while we need to change the location of the wire connected to the etched electrode surface. As the etched electrode surface has multiple PVDF segments isolated from each other, each PVDF segment will have one terminal with a common electrode surface. The sensor film is connected to the data acquisition unit with the alligator clips (attached to the sensor) at one end and the BNC connectors are connecting to the Channel 2 of the Dynamic Signal Analyzer. The back side of each clip is isolated with a tape.

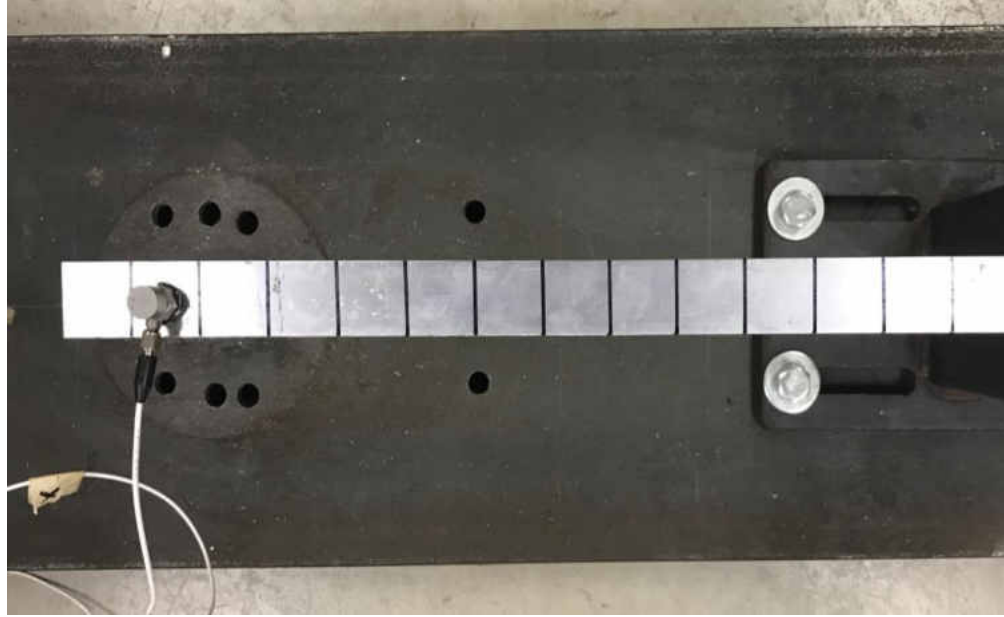


Figure 4.7: Beam divided into 14 sections for accelerometer measurements.

Ensuring the PVDF sensors accuracy and functioning each sensor readings were to be verified with the accelerometer readings, thereby comparing the deflection curve of the beam obtained by the accelerometer to that obtained by distributed PVDF sensors. Hence these sets of measurements by PVDF sensor/accelerometer denote the deflection curve of the vibrating beam.

4.1.3 Experimental Results for the beam.

Figures (4.8-4.13) show the response of the sensor over the frequency ranging from 0-800Hz, for each boundary condition the beam represents, the sensor accurately measures the vibration amplitude apprehending all the resonance frequencies within the excitation signal. Moreover, the figures(4.8-4.13) shows the sensor correctly matches the actual response of the beam over the frequency of interest. Therefore, matching the actual lateral displacement response of the structure with actual lateral displacement response of the sensor is a critical task in sensor development. The results presented in Figures (4.8-4.13)

show the actual lateral displacement curves of the beam and actual lateral displacement curve of the sensor at the first, second, third and fourth modes of vibration. The deflection curve measured with the beam measured through accelerometer coincides with the deflection curve of the PVDF sensor. However, there is a noticeable decline in sensor accuracy as we move to a higher frequency which can be explained with the error innate to the central difference approximation and the approximation of the actual deflection with mode superposition as related to the number of modes included in the computational process.

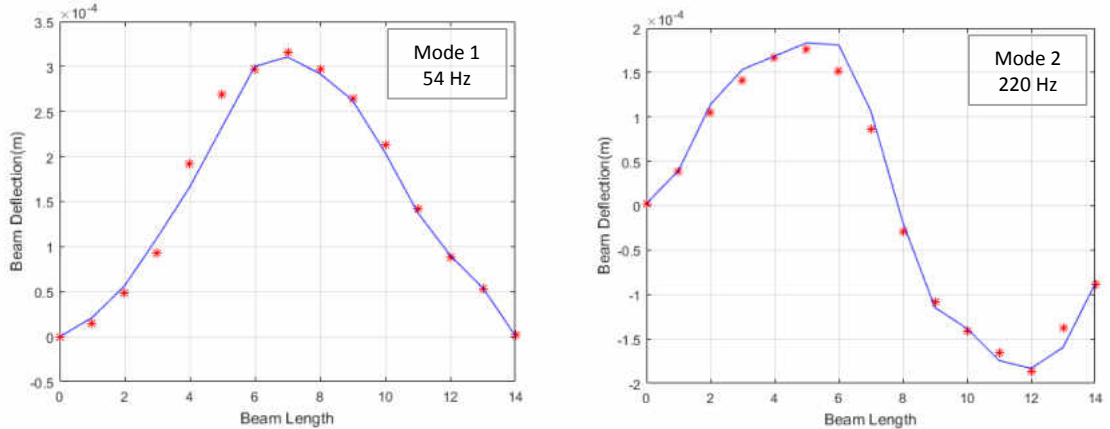


Figure 4.8: Beam (S-S) first and second mode response (Continuous= Actual; Dot=Sensor)

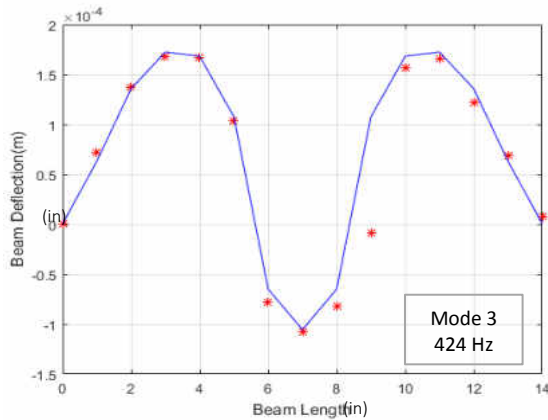


Figure 4.9: Beam (S-S) third mode response(Continuous= Actual; Dot=Sensor)

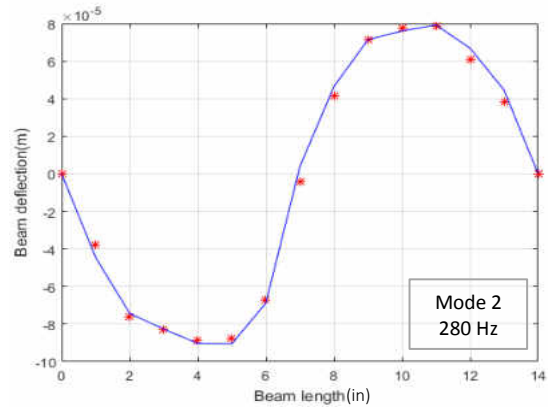
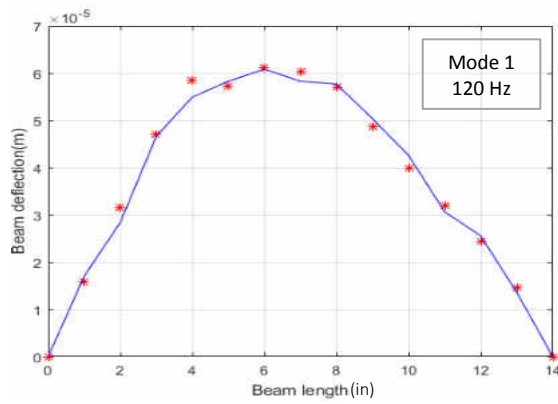


Figure 4.10: Beam (C-C) first and second mode response (Continuous= Actual; Dot=Sensor)

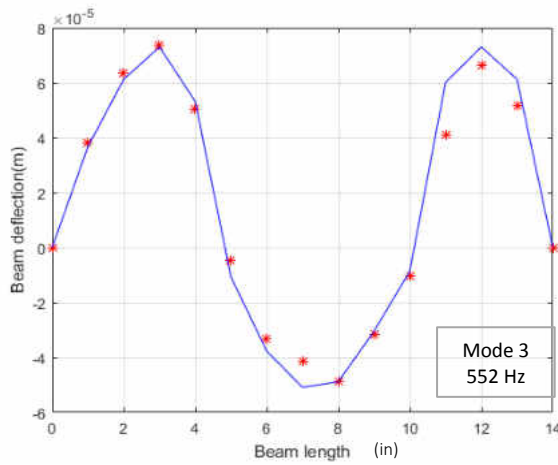


Figure 4.11: Beam (C-C) third mode response (Continuous= Actual; Dot=Sensor)

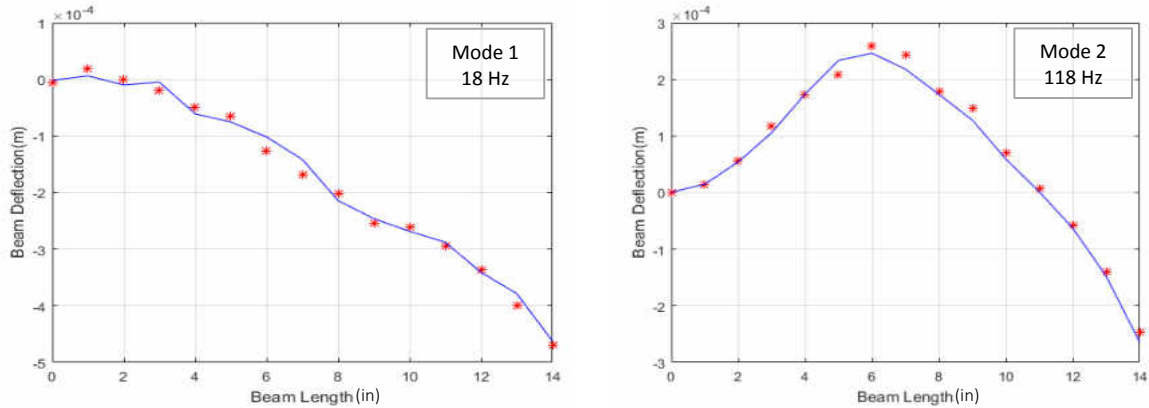


Figure 4.12: Beam (C-F) first and second mode response (Continuous= Actual; Dot=Sensor)

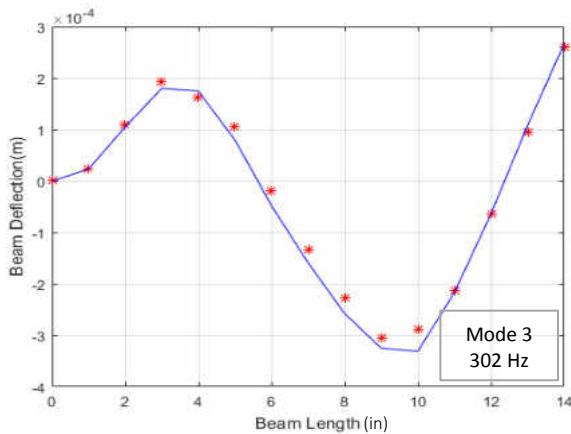


Figure 4.13: Beam (C-F) third mode response (Continuous= Actual; Dot=Sensor)

4.2 Plate Experimental Displacement Measurement.

In case of the plate, a grid formation with a resolution of 15×24 was implemented where the plate was divided into 360 equal parts and shaker was placed beneath the plate for random excitation as shown in Figure 4.14. The plate should be firmly bolted to the supports otherwise will cause irregularities in the experimental results. The schematic diagram for plate experimental setup is shown in Figure 4.15. The accelerometer is placed on these 360 sections individually to obtain the surface

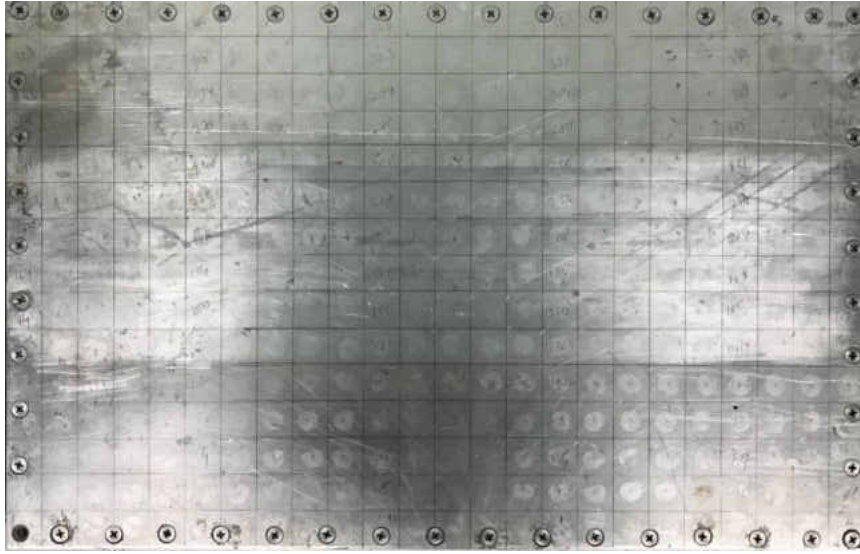


Figure 4.14: Plate with the grid mapping.

acceleration of the vibrating plate. One must be careful while placing the accelerometer on the sections for measuring, as placing the accelerometer should follow a pattern of the grid. Example, if you start measuring from left corner to right corner of the plate for a row in the grid, the next row should be measuring from right corner to left corner of the plate. A particular pattern should be followed because when a sensor film is placed on the plate surface, the film will measure the stress from one corner to another. One section (one of the 360 divisions) missed on the grid by the accelerometer will induce error in the measurement as the film covering the entire row and column will not miss any section on the plate. Thus, it is highly recommended to follow a pattern rather than randomly measuring with the accelerometer. Like the beam in section 4.1.2 the measurements are obtained through the accelerometer and processed through MATLAB to obtain the deflection curve of the vibrating plate. Then, the plate surface is cleaned with dilute phosphoric acid and ammonia water and polished using sandpaper. The $\frac{3}{4}$ " width dual

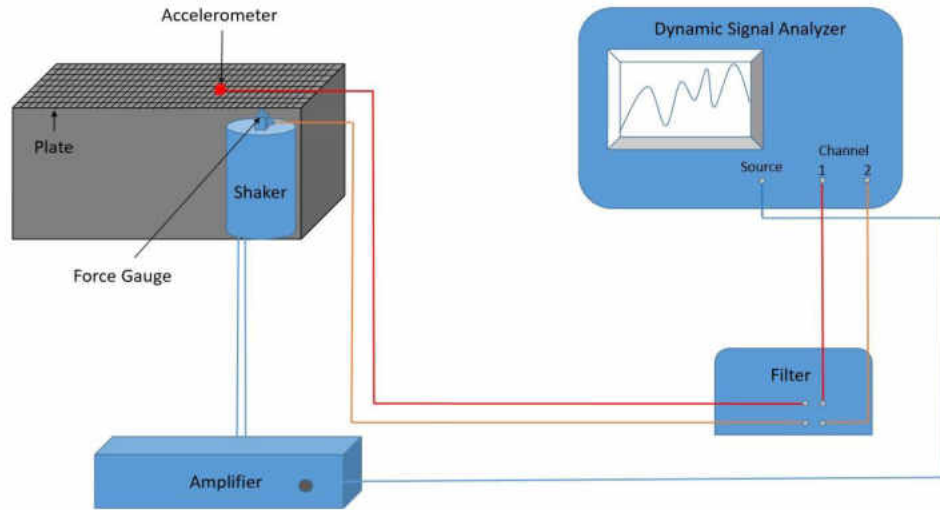


Figure 4.15: Plate Experimental Setup using an accelerometer.

side tape is placed along plate length and width, and then the 1" width PVDF film is attached to the tape along the plate length whereas another film along the plate width. $\frac{3}{4}$ " of the PVDF film is in contact with the tape measuring the stress acting along the plate whereas the remaining $\frac{1}{4}$ " film is utilized for wiring purpose. Multi-meter is used to check that the film is completely isolated and there is no charge leakage. In this case, we measure the deflection of the plate for resonance condition only. Hence two PVDF films are implemented (one along the length and another along width). Here, to follow a different methodology, instead of proceeding with an etching process to obtain distributed PVDF sensors, we use a blade to cut the PVDF film along its length forming 1" x 1" distributed patches across the plate length and width.

The wiring procedure for the PVDF segments in case of the plate is different as compared to the one in beam procedure. For the plate, the PVDF film is cut instead of etching. Hence, the PVDF segments are completely independent of each other and have no common electrode surface as in case of the beam. Each PVDF segment will have two terminals as there is no common electrode surface as in case of the beam.

As described in section 2.7 and [36], designing a sensor to measure the deflection curve for vibrating plate is a challenging task as this involves stress acting along the x and y directions (when the plate vibrates in off-resonance state) whereas the sensor fabricated in section 4.1.1 is capable of measuring stress along x -direction for the beam (the stress along y -direction is assumed to be negligible).

4.2.1 Experimental Results for the plate.

Figures (4.16-4.19) show the response of the sensor over the frequency ranging from 0-800Hz. For each boundary condition the plate represents, the sensor accurately measures the vibration amplitude apprehending all the resonance frequencies within the excitation signal. Moreover, the figures (4.16-4.19) shows the *red grid* representing the measured lateral displacement of sensor correctly matches the actual response of the plate represented by *black grid*, over the frequency of interest. Therefore, matching the lateral displacement response of the structure with lateral displacement response of the sensor is a critical task in sensor development. The results presented in Figures (4.18-4.119) show the lateral displacement curves of the plate and actual lateral displacement curve of the sensor at the first, second, third and fourth modes of vibration. The deflection curve of the plate measured through accelerometer coincides with the actual deflection curve of the PVDF sensor, where the *red dot* representing the measured lateral displacement of sensor are in good match with the *black continuous line* representing the actual lateral displacement of plate. However, there is a noticeable decline in sensor accuracy as we move to a higher frequency which can be explained with the error innate to the central difference approximation and the approximation of the actual deflection with mode superposition as related to the number of modes included in the computational process.

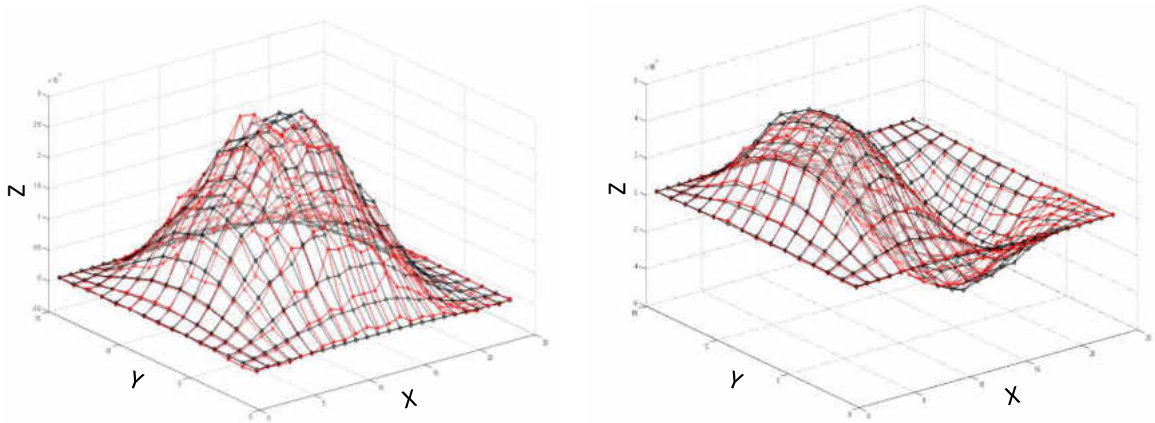


Figure 4.16: Plate (S-S) first and second mode response (Continuous= Actual; Dot=Sensor)

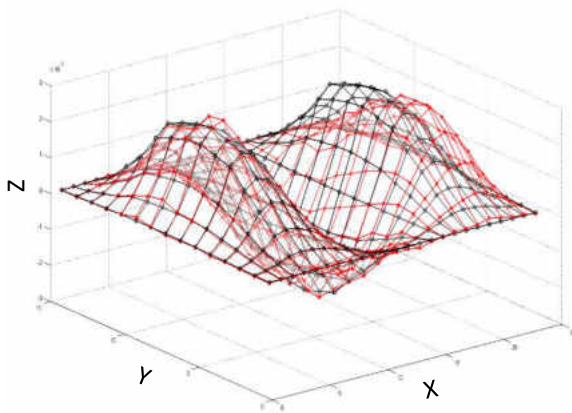


Figure 4.17: Plate (S-S) third mode response (Continuous= Actual; Dot=Sensor)

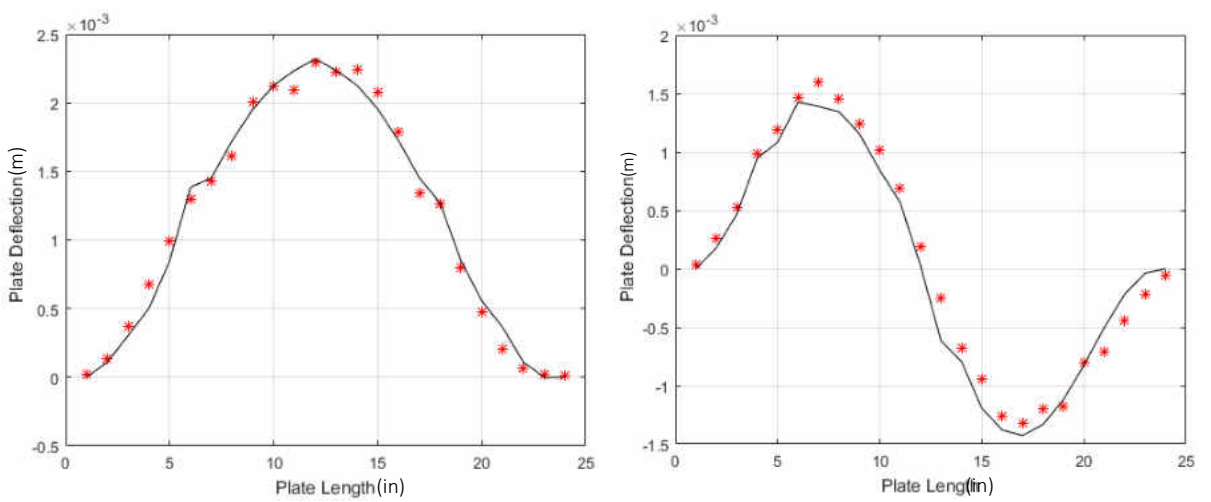


Figure 4.18: Plate (C-C) first and second mode response (Continuous= Actual; Dot=Sensor)

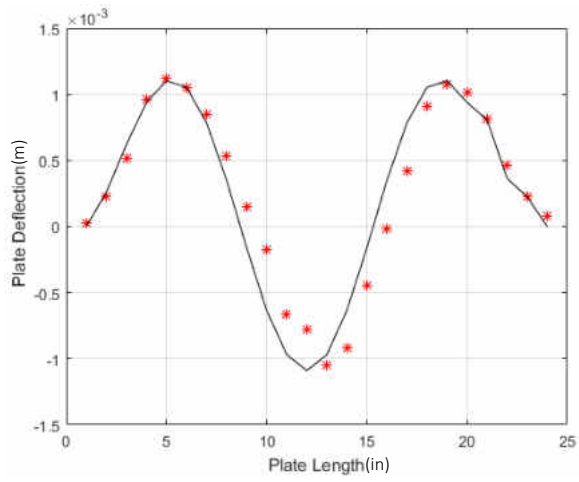


Figure 4.19: Plate (C-F) third mode response (Continuous= Actual; Dot=Sensor)

CHAPTER V

CONCLUSION AND RECOMMENDATIONS

5.1 Conclusion

As mentioned throughout this thesis, the goal of this research is to develop a distributed sensor using polyvinylidene Fluoride film that will accurately measure the deflection curve of a vibrating beam and plate. In past, experimental research has been conducted to measure only the displacement of the beam with piezoelectric material and measuring the plate displacement with piezoelectric material was described as intrinsic task, hence only theoretical work was presented regarding vibrating plate. But in this work, we propose to proceed with a constant shape PVDF film sensor measuring the vibrating plate displacements experimentally. Moreover, best of author's knowledge, this is the first recorded research relating to measuring deflection curve of vibrating plate with proposed sensor design.

This research began reviewing the work of others to gain insight on measuring deflection curves of beam and plate. The review clearly stated that all previous researchers had the charge equation derived by Lee and Moon [34] based on novel development of distributed piezoelectric laminates for control and sensing of bending vibration of flexible beams and plates. This was used as the starting point of sensor design process. The well-established one-dimensional output charge equation of polyvinylidene Fluoride or PVDF helped in deriving equations regarding lateral vibration displacement of the sensor. The accelerometer was used to measure the beam deflection curve. Followed was the sensor

fabrication process for forming PVDF patches across the film through etchings bands across the width of the sensor film. The output charge of the PVDF patch is proportional to the slope of the beam deflection curve at a respective location on the beam. In the numerical analysis, the slopes were substituted in central-difference equations to compute the vibration deflection curve, and the truncation error associated with central-difference method helped derive sensor accuracy.

The proposed sensor was verified through numerical simulation and experimental analysis. The numerical simulation proceeded with mode superposition and discretized models computing the forced vibration responses of the beam over a broadband frequency. Hence deducing the deflection curves and these deflection were compared to the charges calculated from PVDF charge equation (for individual PVDF film patches). The experimental procedure carried out to verify sensor performance as accelerometer readings were used to verify the sensor results. The most prominent source of error is the sensor construction and placement procedure itself; including spilling of the etching solution over the sensor patches tampering the readings, air bubbles getting trapped between the double-sided tape and sensor film, and misalignment of the sensor film concerning beam structure. Other error includes loosening of the bolts (used to impose boundary conditions on the beam) due to vibration.

In conclusion, the goal of the research was accomplished with encouraging results through the use of distributed PVDF sensor measuring the deflection curve of vibrating beams and plates. Though variation in structural displacement were clearly observed through the naked eye, the fact that the sensor was fabricated and placed on the beam by hand clearly justifies the errors induced in experimental readings. Due to the low output

voltage from the PVDF patches, it necessitates implementation of multiple patches at the same location, to sum up the charges. This thesis sets the trend to use distributed PVDF film sensor to measure the complete deflection curve of flexible objects such as beams rather than measuring deflection at particular sections only and measuring deflection curve of plates at resonance, and it is the belief of the author that more accurate data could be extracted with more exact methods exercised.

5.2 Recommendation for Future Work

To make the sensor inexpensive manual work was incorporated in sensor fabrication. Many of the issues regarding the error dealt with the PVDF material itself. Inherent error was inculcated into the sensor while cutting, fabricating and placing the sensor on the beam. In this work, the sensor was first fabricated and then attached to the beam, but in future work, the PVDF film could be placed on the beam first and then the fabrication process can be carried out. This method might help reduce the sensor misalignment on the beam substrate. Controlled brushing of etching solution on to the sensor to prevent spillover.

Gorilla Epoxy Clear was used instead of dual sided tape for attaching the PVDF film on the plate. This, attempt to use a different medium of contact between the plate and PVDF film was a failure as the epoxy substance did not prove to be a good insulation layer; PVDF film charge was leaked. The different medium should be used instead on dual sided tape as slight misalignment in sticking the tape on structural surface results in misalignment of PVDF film being attached on the tape. Thus, resulting error in measurements acquired when structure undergo deflection.

The film is cut along the length when unwrapped from the roll hence makes it easier to be attached to the beam concerning its directional properties, coefficients such as e_{31} and e_{32} . In case of designing a sensor for the plate, the question raised on how e_{31} and e_{32} properties could be distinguished. When the material is unwrapped, and cut from the roll, it is unknown what direction each coefficient lies. These properties should be marked or labelled, otherwise they could easily be reversed. No such apparatus to test the PVDF properties is yet constructed hence markings need to be made on the film.

PVDF sensor must be fabricated for measuring the deflection curve of the plate for the off-resonance condition. This work demonstrated the sensor measuring deflection curve of plate vibrating at resonance only. Now, to measure the deflection curve during off-resonance condition multiple PVDF film need to be attached along the length and width of the plate, covering the entire plate surface. In case of resonance, two PVDF film was used (one along the length & one along the width), whereas off resonance case requires 39 PVDF films (15 along the length and 24 along the width).

APPENDICES

APPENDIX A

MATLAB CODE TO CALCULATE THE NATURAL FREQUENCIES OF BEAM WITH DIFFERENT BOUNDARY CONDITIONS

```
%% Beam Simply Supported At Both Ends

clc

close all;

clear all;

bm=0.0254;           %breath of the model

hm=0.003175;        %thickness of the model

lm=0.3556;          %length of the model

Am=bm*hm;           %area of the model

dm=2767.849;        %density of model

mm=dm*Am;           %mass per unit length of model

a1=1.875;           %constant

Em=69*10^9;         %elasticity of the model material

Im=(bm*hm^3)/12;    %moment of inertia of model

]%%shows the constant values for 10 nodes

for a=[3.1416,6.2832,9.4248,12.5664,5*pi,6*pi,7*pi,8*pi,9*pi,10*pi]

    SIM_SUPPORT=(a^2)*(sqrt((Em*Im)/(mm*Im^4))) *0.5/pi

end
```

```

%% Beam Fixed At Both Ends

clc

close all;

clear all;

bm=0.0254;           %breath of the model

hm=0.003175;        %thickness of the model

lm=0.3556;          %length of the model

Am=bm*hm;           %area of the model

dm=2767.849;        %density of model

mm=dm*Am;           %mass per unit length of model

Em=71*10^9;         %elasticity of the model material

Im=(bm*hm^3)/12;    %moment of inertia of model

shows the constant values for 10 nodes

for z=[4.730041,7.853205,10.9955,14.137165]

    FIX_FIX=(z^2)*(sqrt((Em*Im)/(mm*lm^4)))*0.5/pi

end

c=5:10;

for i=1:length(c)

    constant=((2*c(i)-1)*pi)/2;

    for a=[constant]

        FIX_FIX=(a^2)*(sqrt((Em*Im)/(mm*lm^4)))*0.5/pi

    end

end

end

```

```

%% Beam Fixed Support At One End

clc

close all;

clear all;

bm=0.0254;           %breadth of the model

hm=0.003175;        %thickness of the model

lm=0.3556;          %length of the model

Am=bm*hm;           %area of the model

dm=2767.849;        %density of model

mm=dm*Am;           %mass per unit length of model

Em=71*10^9;         %elasticity of the model material

Im=(bm*hm^3)/12;    %moment of inertia of model

%shows the constant values for 10 nodes

for n=[1.875104,4.694091,7.854757,10.995541];

CANTILEVER=(n^2)*(sqrt((Em*Im)/(mm*lm^4)))*0.5/pi

end

c=5:10;

for i=1:length(c)

    constant=((2*c(i)-1)*pi)/2;

    for a=[constant]

        CANTILEVER=(a^2)*(sqrt((Em*Im)/(mm*lm^4)))*0.5/pi

    end

end

end

```

APPENDIX B

MATLAB CODE TO CALCULATE THE MODE SHAPES OF BEAM WITH DIFFERENT BOUNDARY CONDITIONS

```
%% Calculate the first two modes shapes for Simply supported-Simply supported  
boundary condition.
```

```
clear all;
```

```
close all;
```

```
clc;
```

```
%First Constant for first mode shape
```

```
B1=pi
```

```
%Define range over x-axis
```

```
x = .01:0.01:1;
```

```
%Calculate mode shape for first mode
```

```
W1 = (sin(B1*x))
```

```
%Second Constant for second mode shape
```

```
B2=pi*2
```

```
%Calculate mode shape for second mode
```

```
W2 = (sin(B2*x))
```

```
%Define figure number
```

```
figure(1)
```

```

%Plot the modes shape for first mode
plot(x,W1)

%Define figure number
figure(2)

%Plot the modes shape for second mode
plot(x,W2)

%% Calculate the first two modes shapes for Fixed-Fixed boundary condition.

clear all;

close all;

clc;

%First Constant for first mode shape
B1_1=4.730041

%Evaluate the coefficients for mode shape
a1=(cosh(B1_1)-cos(B1_1))/(sinh(B1_1)-sin(B1_1));

%Define range over x-axis
B11 = .01:0.01:1

%Calculate mode shape for first mode
W1 =(cosh(B1_1*B11)-cos(B1_1*B11))-a1*(sinh(B1_1*B11)-sin(B1_1*B11));

%Second Constant for second mode shape
B2_1=7.853205

%Evaluate the coefficients for mode shape
a2=(cosh(B2_1)-cos(B2_1))/(sinh(B2_1)-sin(B2_1));

%Define range over x-axis

```

```

B2l = .01:0.01:1

%Calculate mode shape for second mode

W2 =(cosh(B2_l*B2l)-cos(B2_l*B2l))-a2*(sinh(B2_l*B2l)-sin(B2_l*B2l));

%Define figure number

figure(3)

%Plot the modes shape for first mode

plot(B1l,W1)

%Define figure number

figure(4)

%Plot the modes shape for second mode

plot(B2l,W2)

%% Calculate the first two modes shapes for Clamped-Free boundary condition.

clear all;

close all;

clc;

%First Constant for first mode shape

B1_l=1.875104

%Evaluate the coefficients for mode shape

a1=(sin(B1_l)-sinh(B1_l))/(cos(B1_l)+cosh(B1_l));

%Define range over x-axis

B1l = .01:0.01:.5

%Calculate mode shape for first mode

W1=(sin(B1_l*B1l)-sinh(B1_l*B1l)-(a1*(cos(B1_l*B1l)-cosh(B1_l*B1l))));

```

```

%Second Constant for second mode shape
B2_1=4.694091

%Evaluate the coefficients for mode shape
a2=(sin(B1_1)-sinh(B1_1))/(cos(B1_1)+cosh(B1_1));

%Define range over x-axis
B2l=.01:0.01:1

%Calculate mode shape for second mode
W2=(a1*(sin(B2_1*B2l)-sinh(B2_1*B2l))-(a2*(cos(B2_1*B2l)-cosh(B2_1*B2l))));

%Define figure number
figure(5)

%Plot the modes shape for first mode
plot(B1l,W1)

%Define figure number
figure(6)

%Plot the modes shape for second mode
plot(B2l,W2)

%end of program.

```


REFERENCES

- [1] X. Escaler, E. Egusquiza, M. Farhat, F. Avellan and M. Coussirat, "Detection of cavitation in hydraulic turbines," *Mechanical Systems and Signal Processing*, vol. 20, no. 4, pp. 983-1007, 2006.
- [2] S. S. Rao, *Mechanical Vibration*, Pearson, 2004.
- [3] Y. Altinta and M. Weck, "Chatter Stability of Metal Cutting and Grinding," *CIRP Annals*, vol. 53, no. 2, pp. 619-642, 2004.
- [4] L. Caracoglia and N. P. Jones, "Numerical and experimental study of vibration mitigation for highway light poles," *Engineering Structures*, vol. 29, pp. 821-831, 2007.
- [5] L. Caracoglia and A. Velazquez, "Experimental comparison of the dynamic performance for steel, aluminum and glass-fiber-reinforced-polymer light poles," *Engineering Structures*, vol. 30, no. 4, pp. 1113-1123, 2008.
- [6] K. Wardhana and F. C. Hadipriono, "Analysis of Recent Bridge Failures in the United States," *Journal of Performance of Constructed Facilities*, vol. 17, no. 3, pp. 144-151, 2003.
- [7] J. Valdman, *Application from Engineering with MATLAB Concepts*, InTech, 2016.

- [8] Randall and R. Bond, *Vibration-based Condition Monitoring: Industrial, Aerospace and Automotive*, Washington, DC: API Publishing Services, 2010.
- [9] J.-F. Lei, L. C. Martin and H. A. Will, "Advances In Thin Film Sensor Technologies For Engine Applications," National Aeronautics and Space Administration., Florida, 1997.
- [10] K. R. Czech and W. Gosk, "Measurement of surface vibration accelerations propagated in the environment," *Procedia Engineering*, vol. 189, pp. 45-50, 2017.
- [11] I. A. K. A. H. O. Ç. Berke Erdaş, "Integrating features for accelerometer-based activity recognition," *Procedia Computer Science*, vol. 98, pp. 522-527, 2016.
- [12] G. Y. Tian, Z. X. Zhao and R. W. Baines, "The research of inhomogeneity in eddy current sensors," *Sensors and Actuators A: Physical*, vol. 69, no. 2, pp. 148-151, 1998.
- [13] D. J. Ewins, *Modal Testing theory, practice and application*.
- [14] J. L. Wang, X. J. Meng and J. H. Chu, "New Properties and Application of Polyvinylidene-Based Ferroelectric Ploymer.," in *Ferroelectric Materials - Synthesis and Characterization*, Intech, 2016, pp. 151-169.
- [15] Y. -H. Huh, J. I. Kim, J. H. Lee, S. G. Hong and J. H. Park, "Application of PVDF Film Sensor to Detect Early Damage in Wind Turbine Blade Components," *Procedia Engineering*, vol. 10, pp. 3304-3309, 2011.
- [16] A. V. Shirinov and W. K. Schomburg, "Pressure sensor from a PVDF film," *Sensors and Actuators A: Physical*, vol. 142, no. 1, pp. 48-55, 2008.

- [17] S. Choi and Z. Jiang, "A novel wearable sensor device with conductive fabric and PVDF film for monitoring cardiorespiratory signals," *Sensors and Actuators A: Physical*, vol. 128, no. 2, pp. 317-326, 2006.
- [18] Y. Ting, Suprpto, A. Nugraha, C. W. Chiu and H. Gunawan, "Design and characterization of one-layer PVDF thin film for a 3D force sensor," *Sensors and Actuators A: Physical*, vol. 250, pp. 129-137, 2016.
- [19] K. Rajanna, M. M. Nayak and G. Roopa, "Non-invasive human breath sensor," Limerick, Ireland, 2011.
- [20] J. C. Adamowski, F. Buiocho and R. T. Higuti, "Ultrasonic material characterization using large-aperture PVDF receivers," *Ultrasonics*, vol. 50, no. 2, pp. 110-115, 2010.
- [21] M. Kryger, T. Eiken and L. Qin, "The use of combined thermal/pressure polyvinylidene fluoride film airflow sensor in polysomnography," *Sleep and Breathing*, vol. 17, no. 4, p. 1267–1273, 2013.
- [22] "Measurement Specialities, Inc.," Norristown, 1999.
- [23] VinhNguyen, S. Melkote, A. Deshamudre, M. Khanna and D. Walker, "PVDF sensor based monitoring of single-point cutting," *Journal of Manufacturing Processes*, vol. 24, no. 2, pp. 328-337, 2016.
- [24] N. Tamjidi, K. Sato, J. Sakurai and S. Hata, "PVDF actuator for high-frequency fatigue test of thin-film metals," *IEEJ Transaction on Electronic and Electronic Engineering*, vol. 8, no. 2, pp. 199-205, 2013.

- [25] S. D. Hu, H. Li and H. S. Tzou, "Precision Microscopic Actuators of Parabolic Cylindrical Shell Reflectors," *Journal of Vibration and Acoustics*, vol. 137, no. 1, pp. VIB-14-1108; doi: 10.1115/1.4028341, 2015.
- [26] A. Pinjan and M. Zahui, "Monitoring of a traffic sign structural support vibrations," in *24th International Congress on Sound and Vibration*, London, 2017.
- [27] R. Gregorio, "Determination of the α , β , and γ crystalline phases of poly(vinylidene fluoride) films prepared at different conditions," *Applied Polymer*, vol. 100, no. 4, pp. 3272-3279, 2006.
- [28] E. Guzmán, J. Cugnoni and T. Gmür, "Monitoring of composite structures using a network of integrated PVDF film transducers," *Smart Materials and Structures*, vol. 24, no. 5, pp. 1-13, 2015.
- [29] E. Guzman, J. Cugnoni, T. Gmür, P. Bonhôte and A. Schorderet, "Survivability of integrated PVDF film sensors to accelerated ageing conditions in aeronautical/aerospace structures," *Smart Materials and Structures*, vol. 22, no. 6, 2013.
- [30] H. Han, Y. Nakagawa, Y. Takai, K. Kikuchi, S. Tsuchitani and Y. Kosimoto, "Microstructure fabrication on a β -phase PVDF film by wet and dry etching technology," *Journal of Micromechanics and Microengineering*, vol. 22, no. 8, 2012.
- [31] H. S. TZOU, *Piezoelectric Shells Distributed Sensing and Control of Continua*, New York: Springer, 1993.

- [32] G. Gautschi, *Piezoelectric Sensorics*, New York: Springer, 2006.
- [33] W. Soedel, *Vibration of Shells and Plates*, Third Edition, New York: New York:Springer, 2004.
- [34] C. K. Lee and F. C. Moon, "Modal Sensors/Actuators," *Journal of Applied Mechanics*, vol. 57, no. 2, pp. 434-441, 1990.
- [35] R. Wendt and M. Zahui, "Development of local volume displacement sensor for vibrating plates," *The Journal of the Acoustical Society of America*, 116 pp., pp. 2111-2117, 2004.
- [36] J. Sirohi and I. Chopra, "Fundamental Understanding of Piezoelectric Strain Sensor," *Journal of Intelligent Material Systems and Structures*, vol. 11, pp. 246-257, 2000.